Assessing Hydrologic Connectivity using Water Temperature, Wax Lake Delta, Louisiana

A Thesis
SUBMITTED TO THE FACULTY OF THE UNIVERSITY OF MINNESOTA
BY

Nicholas Thomas Evans

IN PARTIAL FULFILLMENT OF THE REQUIREMENTS
FOR THE DEGREE OF
MASTER OF SCIENCE

Dr. Chris Paola, Adviser

September 2018

Acknowledgements

I would like to acknowledge and recognize Dr. Chris Paola for allowing me the opportunity to conduct this work. He has shown a unique ability to guide and direct my research in a very meaningful way while at the same time allowing me the freedom to explore topics that are not necessarily within the scope of the great body of work that he has produced and been involved in. I confess that multiple times during this work Dr. Paola gave me advice on a direction to pursue that I initially thought would be unproductive at best, and a waste of time at least. Some of the most intriguing results of my research come from those very suggestions.

Thank you to my parents, Jeff and Linda Evans, for everything they have done to allow me to reach this point. They instilled in me a love of the natural sciences that led to my desire to pursue both graduate school and a career working in the natural sciences. They have always supported and encouraged me in whatever I do, and I cannot adequately express my gratitude enough in this context. I would also like to thank my sister Carly for all of her support and well wishing.

Thanks to my wife Florence Wright for all of her support, help, love, and friendship that extends well beyond the timeframe of this project. Her graduate school experience while obtaining a Master of Social Work degree was the ultimate inspiration for me pursuing my Master's degree, and without her in my life I almost certainly would not have had the motivation to pursue my own graduate studies.

Thanks to Dr. Andy Wickert, who constructed the data loggers used in this study, and provided a great deal of technical advice and troubleshooting help regarding the data logging portion of this

study. He deftly fielded multiple phone calls in the middle of the night to help me troubleshoot data loggers and went far out of his way to do so.

Thanks to Dr. Tim Griffis for his assistance and direction as a member of my thesis committee. His expertise and guidance helped a great deal with many aspects of this project, and he has been an excellent source of answers for many of my questions regarding the meteorological data collection and modeling used in the project.

Thanks to Dr. Antoinette Abeyta, Kareem Mroue, and Gerard Salter for trudging through the Mike Island muck, dodging alligators, visiting oil platforms, and most importantly helping me with the field portion of this study.

Thanks to my colleagues, friends, and the staff at the University of Minnesota's St. Anthony Falls Laboratory. I was lucky to work around such a brilliant group of people, and received significant advice and help with my research from Dr. Heinz Stefan, Chris Ellis, and John Schwenk. This list could and probably should be much longer, so thanks to everyone at SAFL for their help.

Thanks to Wax Lake Delta collaborators from the University of Texas –Austin for helping me with many aspects of my research. Dr. David Mohrig, Dr. Paola Passalacqua, Dr. Wayne Wagner, Dr. John Shaw (now at University of Arkansas – Fayetteville), Matt Hiatt, and Brandon Minton have all made meaningful contributions to this work that I appreciate very much.

Finally, thanks to the National Science Foundation for supporting this work through the Frontiers in Earth Surface Dynamics grant program.

Abstract

The hydrologic connectivity between a delta's primary distributary channels and the interior wetlands of its interdistributary islands is a complex, potentially advective system. We take a reduced complexity approach to assessing the advective factors that contribute to the hydrologic connectivity between a primary distributary channel and interdistributary island on the Wax Lake Delta of coastal Louisiana. We deployed a relatively inexpensive, open-source data logging platform to collect high quality continuous water temperature, water depth, air temperature, and shortwave solar radiation from a portion of Wax Lake Delta from February 18 through May 19, 2015. We use this field data to create a reference model of predicted water temperature at the data logging locations at the site. Based on comparison of that model with the water temperature observations, we find that different regions of the island have differing degrees of hydrologic connectivity to the primary distributary channel. Additionally, we use several methods to assess the spatial relationships between water temperature time series at our data logging locations. We conclude that the distal portions of the island have a high degree of hydrologic connectivity with the primary delta distributary channels. Proximal regions of the interdistributary island wetlands can be either relatively hydrologically isolated from, or highly hydrologically connected to, primary distributary channels, depending on the effectiveness of adjacent island edge levees and the presence of secondary inner island feeder channels.

Table of Contents

List of Tables

List of Figures

INTRODUCTION

Wax Lake Delta

Wax Lake Delta is a relatively recent bayhead river delta located in the Atchafalaya Bay of coastal Louisiana (Carle et al., 2013). The evolution of Wax Lake Delta began in 1941, when the U.S. Army Corps of Engineers dredged the 39 km Wax Lake Outlet to relieve the Atchafalaya River of excess discharge and alleviate downstream flooding within the Atchafalaya Basin (Carle et al, 2013; Shaw et al., 2013). Sediment accommodation space along the outlet channel, particularly within the 12 km portion of the outlet channel passing through Grand Lake, filled with sandy deposits during the first few decades following the dredging of Wax Lake Outlet. Once this accommodation space was filled, accelerated land growth began within Wax Lake Delta (Shaw et al., 2013). By the 1960s a sandy, subaqueous delta had begun to form at the mouth of the Wax Lake Outlet. By 1973 portions of Wax Lake Delta had become subaerial during low tide events, and several high discharge events during the mid-1970s fueled relatively rapid progradation of the delta into the bay (Shaw et al., 2013; Wellner et al., 2005). At present, Wax Lake Delta is composed of a bifurcating network of primary channels that distribute the discharge of the Wax Lake Outlet throughout the delta towards Atchafalaya Bay. In between these distributary channels is a series of interdistributary islands, many of which have interior wetland portions connected to the primary channels via secondary channels and overbank flow and whose distal reaches are open to the delta front and Atchafalaya Bay (Shaw et al., 2016).

The evolution of the Wax Lake Delta has been shaped by an interesting mix of anthropogenic and natural processes. However, outside of the original dredging of the Wax Lake Outlet in the early 1940s, the growth of Wax Lake Delta has proceeded largely without human intervention or interference (Carle et al., 2013; Hiatt and Passalacqua, 2015). This uninhibited

growth coupled with the birth and evolution of a river delta on human-observable timescales makes Wax Lake Delta a particularly interesting case study (Hiatt and Passalacqua, 2015). Much of the recent interest in the growth of Wax Lake Delta is motivated by the desire to use it as a model for planning of Mississippi river diversion projects. These projects seek to use engineered river diversions as a way to mitigate the land loss and possibly the enhanced nutrient delivery to the Gulf of Mexico that plague the region (Hiatt and Passalacqua, 2015; Lane et al., 2011; Paola et al., 2011; Theriot et al., 2013). Our project focuses on water temperature, because it is both important and relatively easy to measure. Water temperature plays a role in the rate at which denitrification proceeds in constructed wetlands (Wood et al., 1999). If large scale diversions are to be built with a partial purpose of aiding the denitrification of river water headed to the Gulf of Mexico, a better understanding of temperature regimes on Wax Lake Delta will lead to better project outcomes. Additionally, water temperature has been cited as an important factor in various biophysical processes in fish, aquatic invertebrates, and the developmental stages of malaria carrying mosquitoes (Paaijmans et al., 2008; Wagner, 2011).

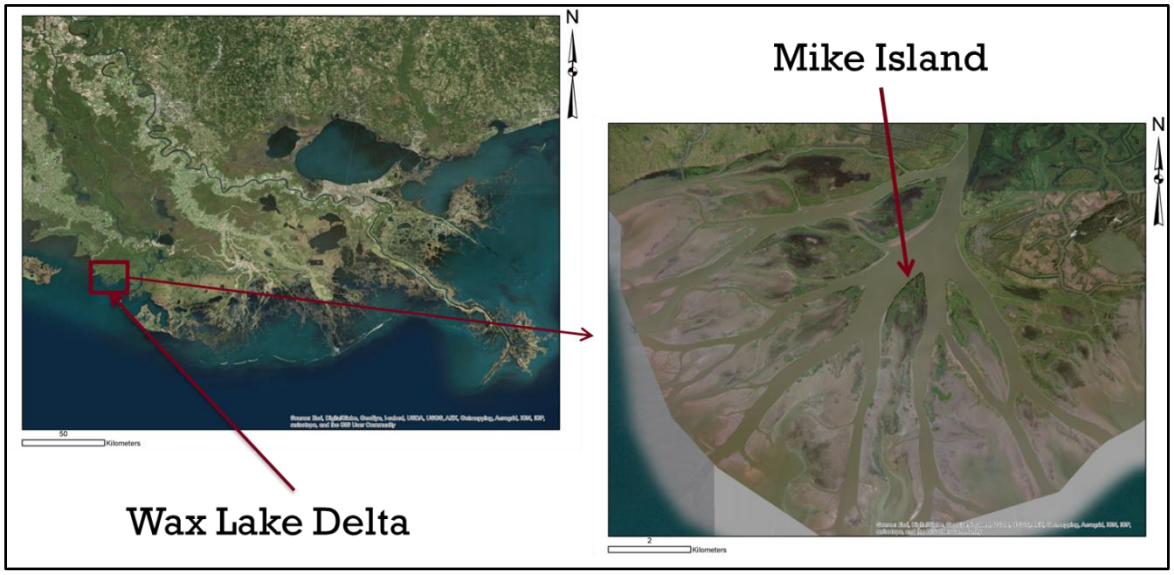

Figure 1: Location of Wax Lake Delta and Mike Island

Mike Island

Mike Island is a lobate, 6 km long interdistributary island with a maximum width of approximately 2 km, oriented roughly north-south in the approximate center of Wax Lake Delta. The northern tip of Mike Island is located approximately 3 km south of the delta apex, while the southern end of the island reaches near the bayward extent of the delta. The edges of Mike Island consist of naturally formed levees, while the interior is more accurately described as an inner island wetland. The island edge levees are at a higher elevation then the interior of the island, and the levees create a hydrologic barrier between the inner island wetlands and the delta's primary distributary channels (Hiatt and Passalacqua, 2015). The formation and evolution of Mike Island generally started near its northern tip and progressed southward. This is reflected in the geomorphic development of the levees, the ecological stage of the vegetation occupying the levees, and the general relative inundation depth of the subaqueous portions of the island (Carle et al., 2013). The northernmost portions of Mike Island are relatively well developed levees stabilized by established populations of *Salix nigra* (black willow) trees. Travelling distally (southward) down the levees, the sediment surface elevation tends to decrease and the vegetation populations transition from *S. nigra* and *Colocasia esculenta* (elephant ear) to species more tolerant of submerged conditions, such as various *Sagittaria* (arrowhead) species and *Nelumbo lutea* (American lotus), both of which are also common in the inner island areas (Carle et al., 2013; Hiatt and Passalacqua, 2015; Shaw et al., 2013). Sediment surface elevations of the northernmost portions of the Mike Island levees are high enough that they are likely submerged only during significant flooding events, while levees farther south on the island may be in various depths of submergence depending on tidal stage (Carle et al., 2013). Overbank flooding of the primary channels across inundated levees becomes more prominent moving distally down Mike Island (Hiatt and Passalacqua, 2015).

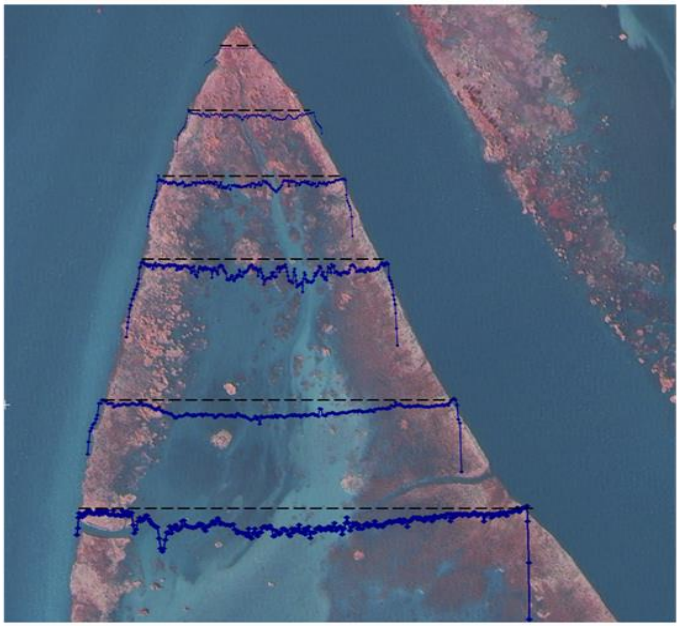

Figure 2: The results of a bathymetric survey of sediment surface elevation on Greg Island, Wax Lake Delta conducted by members of the National Center for Earth-Surface Dynamics (NCED). Dashed black lines represent the surveyed transect while blue lines represent relative sediment surface elevation. High points along the island edge constitute the island edge levees. (Unpublished, courtesy of NCED)

We will discuss two types of channels in this study, primary channels and secondary channels. Primary channels are the larger channels that connect the mouth of the Wax Lake Outlet to Atchafalaya Bay, bifurcating along the way to comprise the series of passes that separate the islands throughout Wax Lake Delta. Secondary channels serve as a connection between the primary channels and the interior wetlands within the inner island areas of Wax Lake Delta (Shaw et al., 2013; Hiatt and Passalacqua, 2015). The secondary channels bisect and cut through the levee edges of the islands of Wax Lake Delta (Hiatt and Passalacqua, 2015). Multiple recent studies highlight the prominent role of hydrologic connectivity between primary channels and inner island areas. Shaw et al. (2016) note that roughly 59% of primary channel flow enters some part of the Wax Lake Delta interdistributary island system, and Hiatt and Passalacqua

(2015) report 23-54% of primary channel flux adjacent to Mike Island travels through its inner island area.

The hydrology of a surface flow wetland located in the interior of a riverine delta island is complex. River stage and discharge, tidal cycles, ocean currents, wind, and waves, and vegetation are some of the factors contributing to the complicated advection processes that dominate the island's surface water hydrology (Hiatt and Passalacqua, 2015; Shaw and Mohrig 2014; Smesrud et al. 2013; Li et al., 2010). Previous attempts to understand the hydrology of wetland islands on Wax Lake Delta, such as the work of Hiatt and Passalacqua (2015) have used dye tracing and flow velocity measurements to study some of the complexity of this system. While providing valuable qualitative data on some of the advective processes at the site, these techniques are expensive, time intensive, and most importantly represent only a small snapshot in time.

Here we develop and apply a relatively simple and inexpensive approach to learn more about this complex system. This study consists of two portions: (1) a field portion where we use a new method of data logging to gather water temperature, water depth, air temperature, and shortwave solar radiation from the inner island area of Mike Island and the primary channel adjacent to the island; and (2) a modeling and analysis portion where we analyze the results of field derived data using several relatively simple methods, with the goals of measuring the effect of advection on temperature variation, and of identifying discrepancies where the simple models fail and thus warrant focus using more detailed approaches..

GENERAL METHODS

Data logger construction, set up, and field deployment

-*The ALog – An Arduino Based Data Logger*

This study used, and aided in the development of, a relatively inexpensive, open source data logging platform to obtain field measured data from Wax Lake Delta. The Arduino-based data logger, known as the ALog, was created by Dr. Andy Wickert as a means to make high quality environmental parameter data logging available, accessible, and highly modifiable, all for a fraction of the cost of commonly used commercially produced data logging platforms (Wickert, 2014).

In order to obtain high quality continuous field data, many studies use industry standard data logging platforms such as the suite of Campbell data loggers. While these standards have many of the benefits that come with large scale production commercial products such as well-developed programming routines, a wide variety of compatible sensors, customer support, and a proven track record of reliability, they also have many drawbacks. These benefits come with a gaudy price tag, and funds-limited research projects may be faced with the issue of having to sacrifice spatial resolution of field data as a result. Programming traditional loggers often relies on proprietary codes, and choice of sensors is often restricted to what has already been commercially developed for the specific data logger. Sensors are generally not highly modifiable, meaning the user is limited to operating them in the same means as whoever created them, regardless of what they are attempting to use them for (Wickert, 2014).

The Arduino microcontroller platform uses open source electronics and a do-it-yourself ethic to promote innovative advances in the physical sciences. The Arduino microcontroller was originally developed as a low cost prototyping platform for physical computing that was simple enough for students without electronics and programming experience to use. At its most basic level, Arduino consists of hardware, software, a programming language, and a community. The

hardware, often referred to as the Arduino board, is a relatively simple circuit board containing a microprocessor (the "brains" of this small computer). The board interacts with the surrounding environment by connecting sensors or other devices to a series of screw terminal wire connection ports mounted on the Arduino board. The Arduino software consists of the integrated development environment (IDE), which is an application that allows the user to write and develop a program that can be easily compiled and uploaded to the Arduino board. Programs written in the Arduino IDE use the Arduino programming language, which is based on a series of functions from the C/C++ programming language. The Arduino community can be seen as a collection of Arduino users who support each other in the development of Arduino based projects, and may include tutorials and learning materials, forums where individuals can receive feedback on projects or problems from other Arduino users, and display innovative projects they have done using Arduino.

The Arduino system is founded on open source ideals as applied to the hardware, software, programming language, and community. "Open source" refers to the transparent dissemination of all aspects of a system. In the context of open source hardware, the schematics, specifications, and sources are made publically available so that others can understand how the hardware is built and functions and are able to reproduce, repurpose, improve, and modify the hardware as they wish. Similarly, open source software makes the source code and programming routines available to the public to reproduce, repurpose, improve upon, and modify. The open source nature of the Arduino platform is ideal for beginners and those with limited electronics and programming experience. The user can either purchase a wide variety of preassembled boards that are ready to go out of the box, or they can construct their own board from scratch. Similarly, the user can freely use existing programs, modify those programs to meet their specific needs, or write their own programs from scratch.

There is a significant body of work using Arduino or other open source electronics prototyping platforms to create environmental sensors for scientific data collection. The development of these systems makes what can be prohibitively expensive technologies accessible to a much wider swath of society. Kelley et al. (2014) created an open source turbidimeter using primarily off the shelf electronics, programmed in the Arduino language, out of components that can be assembled for under $25. Anzalone et al. (2013) created an open source colorimeter using an Arduino board. Leeuw et al. (2013) built an Arduino based in situ fluorometer to study phytoplankton biomass for roughly $150.

The data logger we use in this study, the ALog, is made up of Arduino based hardware and programming. Dr. Andy Wickert developed the ALog to optimize collecting continuous, high quality environmental field data (Wickert, 2014). The ALog we use in this study is the ALog BottleLogger v. 1.0, and in staying true to open source development ideals, both its hardware and software use and build on previously developed components. An ATMega328P microcontroller chip controls all aspects of the logger. Sensors interface with the microcontroller via board mounted screw terminal wire connection pins, which consist of nine pins that serve as either analog or digital read pins, three additional dedicated digital pins, six 3.3V regulated power pins, two VCC power pins, and three ground pins. An onboard SD card reader/writer allows logged data to be written to an SD card in a comma separated text format, a USB connection port provides a means to both upload programs and interact with the board from another computer, and a barrel jack style power plug allows an external power connection, in this case to 3 D-cell batteries. A DS3231 real time clock keeps accurate time for the logger and determines when a logging event will occur (Wickert, 2014). ALog software includes the “Logger” library as written by Dr. Andy Wickert, which implements logging routines, interfaces with sensors, and writes data to the SD card (Wickert, 2014).

-Sensors

In this study, we measured temperatures using negative temperature coefficient (NTC) thermistors (Cantherm +/- 1% 3380K 10Kohm, part number CWF1B103F3380). This model consists of a NTC thermistor potted in a 5 mm wide by 16 mm long bead of ethoxyline resin, connected to a 2-wire PVC coated 1 meter long lead. One wire connects to an analog read pin on the ALog and the second wire connects to one of the board's 3.3V power source pins. When a logging event is triggered, the ALog sends out a 3.3V signal through the wire connected to the power source pin towards the thermistor. When the voltage reaches the NTC thermistor, the resistance of the thermistor is precisely controlled by the temperature of the surrounding material, where the resistivity increases as temperature decreases. This results in a voltage returned to the analog pin that the microcontroller converts to a temperature reading.

We measured air temperatures at logger location 4, using two thermistors to measure air temperatures near the water surface, separated vertically by approximately 58 cm. The black thermistor potting and wire expected to be exposed to shortwave solar radiation were spray painted white to reduce the impact of shortwave solar radiation on air temperature readings. Water temperatures were measured using two thermistors at every logger location with the exception of logger 11, where only one thermistor was deployed due to available pins being occupied by pyranometer sensors.

We measured water depths using the Maxbotix MB7389 ultrasonic rangefinder (*Maxbotix*, Brainerd, MN), which features 1 mm resolution and a reading range of 30 cm to 5 m. We mount the rangefinder unit at a fixed height above the water surface. The rangefinder determines the depth to the water surface by sending out an ultrasonic pulse, known as a "ping", and measures the time it takes the ping to bounce off of the water surface and return to the

rangefinder. The rangefinder applies an air temperature correction to the return time and yields an analog voltage which the microcontroller converts to a range in mm. At every 1 minute logging interval, the rangefinder sends out ten ultrasonic pings and returns ten range readings that are written to the ALog's SD card.

We measured shortwave solar radiation at one location onsite using two Apogee SP-212 pyranometers (*Apogee Instruments, Inc.*, Logan, Utah), which use a silicon-cell photodiode to quantify solar radiation in the spectral range of 360 nm to 1120 nm. Incident shortwave solar radiation powers the initial reading taken by the silicon-cell photodiode, however this yields a voltage too low for sufficient resolution on an analog read pin by the ALog. The SP-212 is an amplified pyranometer that uses power from the ALog to amplify the silicon-cell photodiode signal to a level that is readable by the ALog with high resolution. Two pyranometers were deployed at the same data logging location within Mike Island. An upward facing pyranometer measures incoming shortwave solar radiation, and a downward facing pyranometer measures shortwave radiation reflected from the water surface. The difference between the two pyranometers is taken as the shortwave radiation that the water column absorbs.

- *Logger Housing*

For this study, we designed and built logger housings that could withstand periods of submergence on the order of days to weeks. Keeping with the DIY (Do-It-Yourself) spirit of the project, construction of the data logger housings uses materials available from a local hardware or easily available through online order. The general design of the housing is a 76 mm (3") cylindrical PVC body with a threaded cap on the top and a PVC reducer fitting that tapers to a 19mm (¾") threaded connection housing the ultrasonic rangefinder.

The passage of sensor wires for thermistors and pyranometers through the housing body required the installation of waterproof ports. This proved to be difficult, and sealants designed for use with PVC did not reliably bond with the flexible PVC coating found on what are commonly listed as PVC coated wire. We developed, tested, and deployed a technique where each sensor wire passing through the housing was potted in an epoxy, which performed well in the field and laboratory tests. Detailed step by step instructions on how to construct the logger housing is available in Supplement 1.

- *Field setup*

Measuring water surface elevation using an ultrasonic rangefinder presents unique challenges. Any object that comes between the rangefinder and the water surface may be detected by the rangefinder and lead to an erroneous reading, so biofouling is a concern during field deployment. To deal with this issue, logger housings were set inside of a 152 mm (6") diameter, 1.96-2.54 m (77-100") length PVC outer casing, which acts much like a piezometer. We drilled 19 mm (¾") holes into the lower 0.30-0.91 m (1-3') portion of the 152 mm (6") casing to allow sufficient hydraulic connectivity with the surrounding environment, which we then wrapped with household exterior window screen material secured with hose clamps to limit access to the interior from potential biofoulers. Steel U-channel fence posts 2.4 m (8') high were pounded into the sediment until well seated, and 2-3 hose clamps secured the 152 mm (6") casings to the fence posts. Upon installation, hand measurement of distance to the sediment surface and water surface from the top-of-casing (TOC) was recorded. Since the range finders are measuring a distance from the sensor to the top of the water source, these hand measurements were necessary to convert the range reading to a water depth. We repeated the same hand measurements at the end of the deployment to assess any changes over the deployment period. Logger locations were recorded using a hand held GPS unit.

- Deployment

Data loggers were deployed around Mike Island during two field seasons. The first deployment consisted of 14 loggers deployed from 2/8/2014 to 8/22/2014. During this deployment, all loggers were programmed to record water temperature and depth to water at 1-minute intervals. We recovered 13 of the 14 deployed loggers. Natural processes (waves, tides, wind) appear to have been responsible for the loss of the unrecovered logger. This deployment produced only 5 days of usable data, as a technical issue with the loggers SD card writing routine lead to all loggers ceasing to write data past 5 days into the deployment. Further investigation revealed that the loggers continued to take measurements during the entire deployment, but these measurements were not written to the SD card. Troubleshooting sessions revealed that logging proceeded as designed when using brand new SD cards, however SD card issues arose when reusing cards that had been removed from a logger either to download the data or to upload new programming to the logger. When these previously used SD cards were returned to the logger and the loggers were set to run again, data wrote to the SD card for some time, generally on the order of a few days, before writing ceased. We tested multiple methods of reformatting the used SD cards, but found no solution. The workaround we employed to produce full deployment data recording was to use new, out of the box SD cards during the subsequent successful deployment.

A second deployment from 2/18/2015 to 5/19/2015 was successful and consisted initially of 12 deployed loggers. We deployed 11 loggers in the inner island area of Mike Island, and 1 logger along the northwestern edge of Mike Island in the primary channel. We recovered 10 of the 11 inner island loggers. Nine of the 10 recovered loggers recorded water temperature and depth to water for the entirety of the deployment, and one of these loggers also recorded air temperature at two different heights near the water surface (logger 4). The remaining logger (logger 11), which measured incoming shortwave solar radiation, reflected shortwave solar

radiation, water temperature, and water depth stopped writing data to the SD card during the 44th day of deployment.

Additional meteorological data

In addition to the field data acquired via the data logging units, radiation budget modeling required supplementary meteorological data. We obtained average wind speed, relative humidity, and general cloud cover type at 15 minute intervals from the Weather Underground commercial weather service website (*www.wunderground.com*) using the Patterson, LA station at Williams Memorial Airport (station KPTN) approximately 30 km northeast of the center of Mike Island. We used data from the Houma-Terrebonne, LA airport station (station KHUM, approximately 77 km east of Mike Island) to replace intervals of missing data from the Patterson station for the days of April 21, 22, 27, and 28 and May 1 through 15, 2015. We selected these stations as they are the nearest available airport weather stations to the study site and have similar format, parameters, and data intervals.

Raw data processing

For this study we preprocessed raw field data in several ways prior to any modeling or analysis in order to remove obviously erroneous values. Raw depth to water data had occasional outliers created by false readings from the ultrasonic rangefinders, either in the form of an object in the rangefinder path causing a false depth to water reading, or an unknown error causing an impossible depth to water value (for example, a reading occurring significantly below the sediment surface or a physically unreasonable spike in depth as defined below). Logging intervals of 1 minute made these false readings particularly easy to pick out, as a depth to water change of the order of 1 meter or more over the span of 1 minute was extremely unlikely in this field setting. Extreme outliers tended to be at a relatively consistent value for each individual logger,

so we applied a filter to remove any values exceeding a certain threshold. After we removed outliers, we applied the MATLAB function *naninterp* to interpolate across the removed intervals. Raw water temperature data also occasionally contained impossible values, which we removed in a similar fashion to the raw depth to water data.

After removing outliers, we smoothed noisy data using MATLAB's *filter* function, a moving average filter. We used a window size of 50 for depth data and a window size of 25 for temperature data. We applied a shift to the resulting filtered data to remove the lag introduced by the moving average filter.

Models and Equations

- *Water Temperature Reference Model*

We created a reference model for this study by calculating a simple, single layer energy budget model using a combination of field data collected during the field deployment portion of the study and supplemental basic meteorological data obtained from publicly available sources. We model the rate of change of water temperature using the following equation:

$$\frac{\Delta \boldsymbol{T}}{\Delta \boldsymbol{t}} = \frac{\boldsymbol{E_t}}{(\boldsymbol{\rho_w})(\boldsymbol{Cp_w})(\boldsymbol{depth})} \qquad \textbf{(Equation 1)}$$

where $\Delta \boldsymbol{T}$ is the change in temperature (℃), $\boldsymbol{E_t}$ is the total energy flux (kJ/m^2/ min), $\boldsymbol{\rho_w}$ is the density of water (assumed to be = 999.97 kg m^{-3}), $\boldsymbol{Cp_w}$ is the heat capacity of water (4.185 kJ kg^{-1} °K), and $\boldsymbol{depth}$ is the water depth (m). The change in time $\Delta \boldsymbol{t}$, was set to equal 30 minutes. We averaged all field measured and externally obtained meteorological data used into 30 minute intervals.

The total energy flux $\boldsymbol{E_t}$ is found by:

$$\boldsymbol{E_t = K_a + L_{in} - L_{out} - H - L_e - G_s} \qquad \textbf{(Equation 2)}$$

where $\boldsymbol{K_a}$ is total absorbed shortwave radiation (W m^{-2}), $\boldsymbol{L_{in}}$ is incoming longwave radiation (W m^{-2}), $\boldsymbol{L_{out}}$ is outgoing longwave radiation (W m^{-2}), $\boldsymbol{H}$ is the sensible heat flux at the water surface (W m^{-2}), $\boldsymbol{L_e}$ is the evaporation at the water surface (W m^{-2}), and $\boldsymbol{G_s}$ is the ground energy flux (W m^{-2}). The two methods of determining $\boldsymbol{K_a}$ in this study are (1) field measured data from deployed pyranometers, and (2) a simplified solar radiation modeling approach outlined later in this paper. The field measured data is found by subtracting the reflected shortwave radiation (measured with a downward facing pyranometer) from the total incoming shortwave radiation (measured with an upward facing pyranometer). The resulting value for $\boldsymbol{E_t}$ is in W m^{-2} which we convert to kJ m^{-2} min^{-1} by multiplying by 60 and dividing by 1000.

The incoming longwave radiation $\boldsymbol{L_{in}}$ is calculated as presented in Paaijmans et al. (2008):

$$\boldsymbol{L_{in} = \left(0.56 + 0.067\sqrt{e}\right) \sigma T_{ak}^4 + dm_c} \qquad \textbf{(Equation 3)}$$

where $\boldsymbol{e}$ is the vapor pressure (hPa), $\boldsymbol{\sigma}$ is the Stefan-Boltzmann constant (5.67 x 10^{-8} W m^{-2} °K^{-4}), $\boldsymbol{T_{ak}}$ is the air temperature (°K), $\boldsymbol{d}$ is a constant (0.60), and $\boldsymbol{m_c}$ is the fractional cloud cover which we explain in depth in the cloud cover radiation model presented later in this study. The vapor pressure, $\boldsymbol{e}$ is found by calculating the saturated vapor pressure, $\boldsymbol{e_s}$ using the procedure of Campbell and Norman (1998) and Paaijmans et al. (2008):

$$e = RH(e_s) \quad \textbf{(Equation 4)}$$

$$e_s = 611.2\, exp\left(\frac{17.67T_{ac}}{T_{ac} + 243.5}\right) \quad \textbf{(Equation 5)}$$

where $\boldsymbol{RH}$ is the percent relative humidity and $\boldsymbol{T_{ac}}$ is the air temperature in °C.

$\boldsymbol{L_{out}}$ is the outgoing longwave radiation and is found as presented in Kustas et al. (1994):

$$L_{out} = \varepsilon_w \sigma T_{wk} \quad \textbf{(Equation 6)}$$

where $\boldsymbol{\varepsilon_w}$ is the emissivity of water (0.98) and $\boldsymbol{T_{wk}}$ is the water temperature in °K.

The sensible heat flux $\boldsymbol{H}$ is found by:

$$H = \rho_a c_p u\, C_h(T_{wc} - T_{ac}) \quad \textbf{(Equation 7)}$$

where $\boldsymbol{\rho_a}$ is air density (1.225 kg m^{-3}), $\boldsymbol{c_p}$ is the heat capacity of air (1004 J kg^{-1} K^{-1}), $\boldsymbol{u}$ is the wind speed (m s^{-1}), $\boldsymbol{C_h}$ is a dimensionless heat transfer coefficient parameterized by Paaijmans et al. (2008) equal to 3×10^{-3}, and $\boldsymbol{T_{wc}}$ is the water temperature (°C).

The evaporative heat flux $\boldsymbol{L_e}$ is found by:

$$L_e = f(w)(e_s - e_a) \quad \textbf{(Equation 8)}$$

where $f(w)$ is a wind speed function:

$$f(w) = 6.9 + 0.345w^2 \quad \textbf{(Equation 9)}$$

$$e_s = 6.112\ exp\left(\frac{17.67\ T_{ac}}{T_{ac} + 243.5}\right) \quad \textbf{(Equation 10)}$$

$$e_a = e_s \frac{Rh(\%)}{100} \quad \textbf{(Equation 11)}$$

where w is the wind speed (m/s), e_s is the saturation vapor pressure (mb), T is the air temperature (°C), e_a is the actual vapor pressure (mb), and $Rh(\%)$ is the relative humidity (Ji 2008).

The ground heat flux, G_s is found using (Paaijmans et al., 2008):

$$G_s = 0.15(K_a + L_{in} - L_{out}) \quad \textbf{(Equation 12.a)}$$

The results of an alternate analysis using the following parameterization can be found in Appendix L:

$$G_s = 0.05(K_a + L_{in} - L_{out}) \quad \textbf{(Equation 12.b)}$$

Reference modeled water temperatures were reset to the field measured water temperature for each logger location every night at midnight, to prevent accumulation of errors.

- *Clear Sky Solar Radiation Model*

We apply a clear-sky solar radiation model to parameterize the total absorbed shortwave radiation, $\boldsymbol{K_a}$ in our simple water temperature reference model. Highly detailed radiation budget studies often require site specific field measurements of solar radiation, which preferably requires well maintained and often expensive monitoring equipment that is not typically available for many sites (Norman and Campbell 1998; Paaijmans et al., 2008; Paulescu et al., 2013). In the case of our relatively simple reference model, creating a model of solar radiation fluxes rather than using field measured values allows the study to be repeated at other sites where field measured solar radiation fluxes are unavailable. A detailed description of the equations and process used to create the clear sky solar radiation model can be found in Appendix A.

At its most basic level, a clear sky solar radiation model provides the theoretical maximum of incoming shortwave solar radiation for any given location on earth at a specific time (Kasten and Czeplak, 1980; Muneer and Gul, 2000). The basic process involves starting with a simply modeled value of extraterrestrial shortwave solar radiation incident upon the top of the earth's atmosphere, which uses the relation between earth-sun distance and time of year to provide a well constrained value. The model then uses the relationship between the site location, day of year, and time of day to establish the position of the sun in the sky throughout the modeled period, which is known as the solar zenith angle. We then use the solar zenith angle, extraterrestrial shortwave solar radiation, and several other basic parameters to estimate the total shortwave radiation incident upon the surface of our field site during clear sky periods (Kasten and Czeplak, 1980; Muneer and Gul, 2000; Norman and Campbell, 1998).

- *Cloud Cover Radiation Model (CRM)*

As mentioned previously, clear sky solar radiation models provide a theoretical maximum value of solar radiation at a given site. As the name implies, this type of model assumes uniformly clear skies throughout the modeled time period, whereas in reality the presence of clouds considerably modifies incoming solar radiation. Many detailed models exist which attempt to describe the effect of clouds on radiation budget fluxes, and many of these models rely on accessing highly detailed and complex descriptions of cloud type and height (Reno and Stein, 2013; Luo et al., 2010) or detailed long running field observation that requires onsite field staff for the duration of the study (Kasten and Czeplak, 1980). A more simplified approach uses a parameter known as the *okta*, or fractional cloud cover to describe the relative fraction of the sky containing cloud cover (Muneer and Gul, 2000; Gul et al., 1998; Kasten and Czeplak, 1980). This is not a parameter that is widely available to the public for many field sites, so we propose a method to model the relationship between a commonly available sky type parameter and the amount of solar radiation that reaches the ground surface.

Many major commercial weather services provide both real-time and historical weather data that is easily accessible to the general public via the internet. Most of this data is numeric, however one of the most prominent and recognizable features of a weather report is the weather icon. These weather icons are generally tied to a descriptive string, such as a sun icon tied to the phrase "Clear", a sun partially obscured by a cloud icon tied to the phrase "Partly Cloudy", and a cloud icon tied to the phrase "Cloudy". We refer to these descriptors as "sky type" from here on, which we downloaded from a publicly available commercial weather service as previously described. Each sky type descriptor was assigned an $\boldsymbol{okta}$ value, which was then converted to a $\boldsymbol{m_c}$ value following Luo et al. (2010). Sky type descriptor string and $\boldsymbol{m_c}$ values are presented in Table 1. We use the $\boldsymbol{m_c}$ value to modify the total absorbed shortwave radiation, $\boldsymbol{K_a}$ modeled in

the clear sky solar radiation model to obtain a more accurate representation of the shortwave solar radiation reaching the water surface on Mike Island.

Sky Type	m_c	Sky Type	m_c
Clear	0	Light Rain	1
Scattered Clouds	0.4375	Heavy Rain	1
Partly Cloudy	0.5	Thunderstorm	1
Mostly Cloudy	0.75	Mist	1
Overcast	1	Light Thunderstorm	1
Haze	1	Heavy Thunderstorm	1
Rain	1		

Table 1: Weather Underground Sky Type Predictors and their associated $okta$ and m_c values

Results

We present field measured water temperature time series for each logger location in Appendix B, and field measured water depth time series for each logger location in Appendix C. Appendix D contains graphs of predicted versus observed water temperature time series for each logging location using field measured shortwave solar radiation, while Appendix E presents the results of predicted versus observed water temperature time series for each logging location using our cloud cover radiation model to predict water temperature. We present the resulting fluxes for the clear sky solar radiation model, the cloud cover radiation model, the field measured shortwave radiation, and the difference between field measure and predicted shortwave radiation in Appendix F. Appendix G contains time series data of radiation flux terms at each data logging location.

METHODS, RESULTS, AND DISCUSSION OF INDIVIDUAL ANALYSES

Method 1: Reference Model Anomaly

Introduction

Acknowledging the complexity of various interacting processes contributing to water flow around and within Mike Island and the inherent difficulty of accurately capturing the role of advection when modeling water temperature across the island, this analysis uses a reference model approach to model only a portion of the system that can be more accurately explained. We compare this reference model against field measured values, where the difference between the two is treated not as an error, but as an analyzable, quantitative value indicative of the role of more complex, un-modeled processes.

We borrow the usage of a reference model from the software engineering world and apply a reference model to analyze environmental systems as presented by Power et al. (2005). The specific aspect of a reference model we utilize here is to apply some basic ideas and relationships to create a simplified model of an otherwise exceedingly complex natural system. We accept that this model will not accurately capture the entire complexity of the system. Rather, its role is to identify what, if any, parts of the measured signal reflect the relatively simple, first-order balances defined in the equations of the previous section. With these identified, future work or further analysis can focus on those aspects of the system where more complex processes come into play.

Water temperatures at any point in time on the site are the result of a potentially complex interplay among river channel, stage, discharge and temperature, tides, currents, winds, geomorphic structures (including natural levees, secondary feeder channels connecting river channels with the interior of the islands, inner island geomorphic and vegetative structures) and radiation energy budget. Of these variables, all except radiation energy budget are advection related terms. A separate study conducted by Hiatt and Passalaqua (2015) found that the

dynamics of the advective system on Mike Island are complex. The reference model assumes that the most significant radiation inputs may be accurately modeled using previously established radiation balance modeling techniques. We use our radiation model to predict the water temperature at select locations on the island while ignoring any advective terms, and compare this reference model to water temperature field data obtained via this studies data logging systems. We use the anomaly between the predicted temperature and the measured temperature to infer the presence of possible advection related phenomena.

Paaijmans et al. (2008) conducted a study that provides a relevant and useful analog to our reference model. The study cites the direct link between the growth and development of immature, malaria carrying mosquitoes and the diurnal water temperature regimes of the pools they live in. In an attempt to better predict and manage these populations in sub-Saharan Africa, the authors use a 1-dimensional energy budget model to predict the diurnal water temperature time series of a small, circular "kiddie" pool (0.96 m diameter, 0.33 m deep) filled with water. Two models were employed: (1) an energy budget model using meteorological and radiation data obtained from nearby weather stations, and (2) a simplified version of model (1) using the Angstrom approach for modeling incoming radiation. The authors then compare these results to water temperatures measured in the small test pool (Paaijmans et al., 2008).

The approach taken by Paaijmans et al. (2008) is both similar to and fundamentally different than the reference model approach we use. Like Paaijmans et al. (2008) we create two different 1-dimensional energy budget models, one using measured incoming shortwave radiation inputs and one using a fractional cloud cover derived solar radiation model for inputs. However the fundamental difference is that Paaijmans et al. (2008) develop their model as a means to accurately describe their system of interest (a pool of water) while we use the reference model approach to model only part of a greatly reduced complexity system.

For analysis of our model we make the simple assumption: that the water temperatures we model represent the water temperatures that would exist on Mike Island for each logger location were there to be zero advection occurring on the island. This is analogous to the small pool modeled in Paaijmans et al. (2008) being present at each logger location, with water depths within each pool tracking the measured water depths of each logger location through time. The assumption of zero advection on the inner island areas of Wax Lake Delta is known to be untrue, based on the work of others (Hiatt and Passalacqua, 2015; Shaw et al., 2016), as well as both water depth time series and qualitative field observations made during this study, but the strength, times, and locations of advective effects on temperature are not known. Therefore, we use the difference between modeled and measured water temperatures as an indicator of the presence of advected cooler, more stable temperature main channel water into and throughout the inner island wetland. In this context, we interpret greater positive anomalies as representing areas that have a water temperature signature more characteristic of water recently and/or more strongly advected from the primary channel. We interpret smaller positive anomalies as representing areas where water behaves more like the stagnant water of a small pool, i.e. water that has longer residence time and spends more time in the inner island area.

Method

We calculate the anomaly between the reference model water temperature and the field measured water temperature for each logger location as follows

$$\boldsymbol{Anomaly = T_{mod} - T_{meas}} \qquad \textbf{(Equation 13)}$$

where $\boldsymbol{T_{mod}}$ is the water temperature predicted by the reference model (°C) and $\boldsymbol{T_{meas}}$ is the actual water temperature as measured by the data logger (°C). We then separate anomaly values

for each location based on whether they were positive or negative in order to eliminate any averaging effect that may occur from analyzing the two together. Additionally, we present plots depicting the rate of change of water level versus anomaly at each location as a means to further assess our anomaly model.

Results

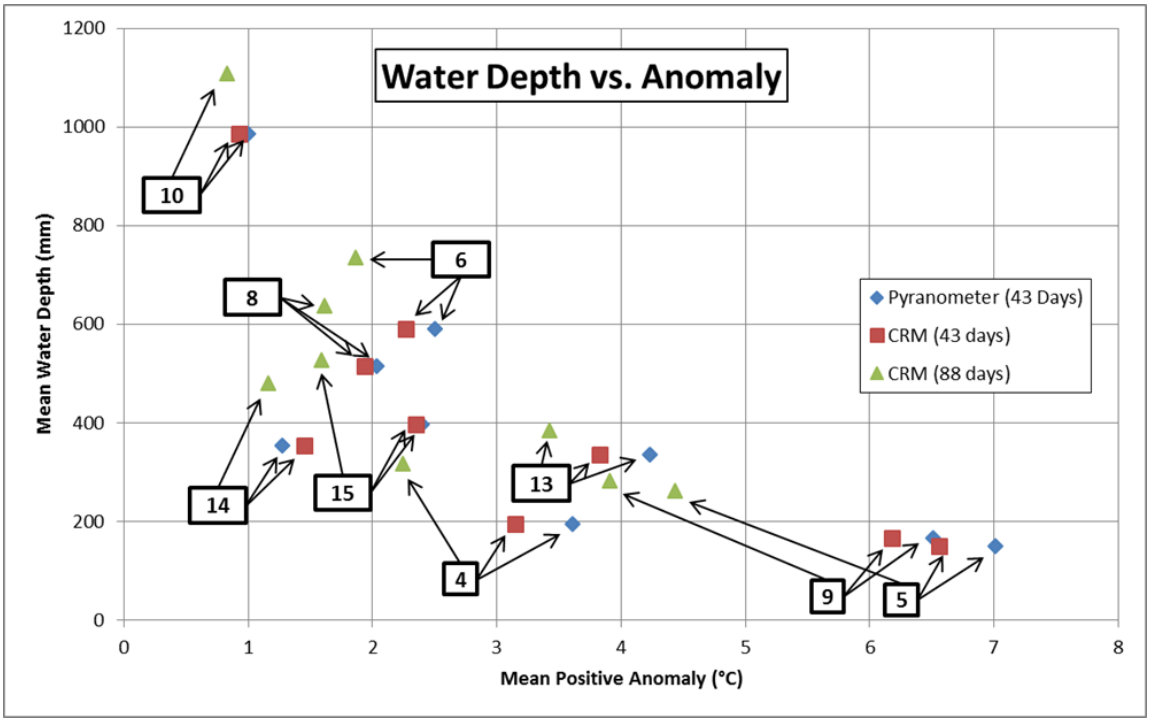

Figure 3: Mean Water Depth vs. Mean Positive Anomaly

Figure 3 shows a graph of mean water depth against mean positive anomaly for both CRM and pyranometer measured water temperature modeling. Pyranometer modeled data is plotted for the first 43 days of data logger deployment, as pyranometer data collection failed on the 43rd day of deployment. CRM modeled data is plotted for the first 43 days of the deployment to compare with the length of record for pyranometer modeled data. Additionally, CRM modeled

data was plotted for the entire length of deployment. We present tables summarizing mean water depth, mean positive anomaly, mean negative anomaly, and mean total anomaly in Appendix H.

Appendix K presents plots of the change in water depth versus the mean total anomaly for all modeled locations. The rate of change of water level is computed at 30 minute intervals. Plots are presented showing change in water depth versus mean total anomaly for the full length of deployment and for days of year 75-85.

Discussion

From Figure 3 it is clear that a primary control on mean positive anomaly at the measured locations is water depth. Shallow logger locations tend to have greater mean positive anomaly, while deeper logger locations have lower mean positive anomaly values. Comparison of mean positive anomaly values for loggers of relatively similar mean water depth provides insight into the hydrologic connectivity between channel water and inner island water. A grouping of the three shallowest logger locations (5, 9, and 4) provides a good example. Loggers 5 and 9 have greatest mean positive anomaly, and are both located in areas where it makes sense that they are closely connected to channel water advection: logger 9 is at the outlet of the primary feeder channel on the northern portion of Mike Island; logger 5 is adjacent to the natural levee on the western side of Mike Island, distally enough that the natural levee provides less of a hydrologic barrier between channel water and inner island water than more proximal locations. In contrast, logger 4 shares a similar mean water depth with loggers 5 and 9, yet has roughly half of the mean positive anomaly as those two locations. We interpret this as evidence that logger 4 represents an area of the island where water residence times are greater than loggers 5 and 9.

Loggers 13, 15, and 14 are another grouping of three logger locations with similar mean water depths. Logger 13 has the highest mean positive anomaly of this group, indicating that it is

the most hydrologically connected to the channel water. Logger 13 is relatively distal and in an area of the island where frequent inundation of the island edge levees allows for a stronger connection between the river channel and this area of the interior of the island. Logger 14 had the lowest mean positive anomaly of this grouping, indicating that it is the least hydrologically connected to channel water of the group. Interestingly, logger 14 is in close proximity to logger 9, which we interpret as having a high degree of hydrologic connectivity with the channel via its proximity to the outlet of the feeder channel. The discrepancy between apparent connectivity with the channel between locations 9 and 14 may point to the presence of a hydrologic barrier or flow divide between the two locations. The apparent presence of standing water during low tide periods at location 14 supports the idea that logger 14 has a different hydrologic regime than most of the other logger locations. Other logger locations in the northern portion of the island tend to go dry during the lowest tidal periods, however during the same periods that these other locations are going dry, location 14 shows standing water. It appears that some kind of isolated water body exists in the north east portion of the island near logger location 14 during low tide, and this could also point to a reason why, despite its relatively low mean depth, location 14 has such a low mean positive anomaly. The relative hydrologic isolation of location 14 means that the standing water assumption we make in our reference model is closer to true than in other areas where advection and close connection to channel water dominate the water temperature signature. Logger 15 produces mean positive anomaly values in between those of loggers 13 and 14, and has a nominally deeper mean water depth than those other two locations. This points to a more moderate connection between channel water and location 15, where water residence times fall somewhere between those of locations 13 and 14. Spatially located in the central portion of the northern half of Mike Island, the connection between the inner island area near location 15 and channel water likely comes as a mixture of water supplied by prominent secondary feeder

channels (such as the main northern feeder channel) and channel water that is able to overtop the less effective levees of the southern portion of the island.

Tables H.5, H.6, and H.9 present the mean total anomaly results for modeling using field measured (pyranometer) radiation values as well as the cloud based radiation modeling for the first 43 days of deployment and for the entire length of deployment. The mean total anomaly for all logger locations using CRM modeling for the entire deployment is 0.73 °C, using pyranometer data for the first 43 days is 1.37 °C, and using CRM data for the first 43 days is 1.08 °C. These values show that our methods of modeling water temperatures on Mike Island may be useful for predicting water temperatures for the purpose of ecological studies in similar settings. The results of an alternate parameterization of Gs found in equation 12.b, which uses 0.05 instead of the 0.15 used by Paaijmans et al. (2008) can be found in Tables L.1-9. These tables show that generally a greater positive, negative, and total anomaly results from using the alternate parameterization.

These results point to the strong role of advection in regulating water temperature on the bar top, and the spatial variability in temperature that this causes. A future study could be designed around this idea and the water temperature anomaly analysis on which it is based. Due to the strong role of water depth in water temperature modeling, it would be interesting to perform a study where logger locations were selected entirely based on sediment surface elevation. Locations could be selected so that larger groups of loggers were placed at similar sediment surface elevations, which would therefore place them in groups of similar water depth. By locating many loggers at similar depths, the role of water depth would be effectively eliminated and intra group comparisons of mean positive anomaly could yield more insight into the hydrologic regime of various portions of a river dominated deltaic wetland island.

Method 2: Correlation Coefficient Analyses

Method

In this method we compute correlation coefficients for measured water temperatures between every possible pair of loggers to assess similarity between time series. We compute cross correlation between logger pairs using the *xcorr* function in Matlab (version 2014a) to eliminate the effect of lagged signals between loggers. We divide logger pairs into 4 different correlation coefficient bins ranging from 1 to 0.9, 0.9 to 0.8, 0.8 to .7, and less than 0.7. We then create a map for each bin, where a line connects logger pairs that share a correlation coefficient occurring in that particular bin. We assign a unique line color for each bin, and create a fifth map that compiles all logger pair correlation coefficients into one map. Finally, we create a map that uses our color coded line connections to display the correlation coefficients between the primary channel logger location and each of the inner island locations.

Results

Appendix I presents the results of our correlation coefficient analysis and contains matrices of cross correlation and lag, as well as maps of correlation coefficient relationships between logger locations.

Discussion

By calculating correlation coefficients for water temperature time series between every logger pair we can assess how closely related various locations on Mike Island are in terms of water temperature. One useful way to approach the larger analysis presented here is to focus solely on the correlation coefficients between logger 6 (the primary channel location) and all others (the inner island locations). This method highlights some general spatial relationships

between water temperatures in the primary channel and inner island areas, while we present a more in depth analysis involving all pairs that highlights relationships between inner island locations later on.

Correlation between inner island locations and river channel location

Analysis of correlation coefficients provides a simple way to assess the degree of hydrologic connectivity between the primary distributary channel and inner island areas. We deployed logger 6 in its specific location with the intention of capturing water temperatures in the primary channel. Thus we assume that correlation coefficients between logger 6 and each inner island logger represent how hydrologically connected each inner island location is to the channel. We suggest that inner island loggers having relatively high correlation with logger 6 have a stronger connection with the primary channel, and view those with relatively low correlation as more hydrologically isolated from the channel.

Loggers 5, 9, 8, 10, and 13 all have correlation coefficients greater than 0.90 with logger 6, which we interpret as a relatively strong hydrologic connectivity between the river channel and these locations, and hence strong advective influence. Loggers 8, 10, and 13 are in the southwest, distal end of Mike Island. In these distal locations, levee development and bed elevations are both less than in the northern portion of the island, which leads to more frequent and longer submergence of these distal levees than the levees in the northern portion (Carle et al., 2013; Hiatt and Passalacqua, 2015). When submerged, these distal levees provide a less effective hydrologic barrier between the inner island and the river channel. Additionally, what appears to be a large feeder channel cuts through the eastern levee just northeast of logger 10. Hiatt and Passalacqua (2015) recorded bi-directional flow in channels similar to this one on Wax Lake Delta, with

reversal of flow between the rising and falling limbs of the tidal cycle. Channels such as this provide an enhanced hydrologic connection between the primary channel and inner island wetlands, and contribute to the relatively strong correlation between the distal loggers and logger 6.

Loggers 5 and 9 also have strong correlation with logger 6. Logger 5 is along the inner edge of western Mike Island levee, roughly midway between logger 6 and the more distal locations. This is an area where levees are more developed than in the distal portions of the island, but are not as often sub aerial as in the more developed northern portion of the island. Logger 9 is near the outlet of the main northern distributary channel, and its high correlation to the river channel water temperature makes it one of the most interesting of the high-correlation group. This high correlation with the river channel verifies that the main northern distributary channel is acting as a significant conduit linking river channel water to portions of the northern inner island.

Logger locations that have the lowest correlation to the river channel water measured by logger 6 demonstrate areas of the island that are more hydrologically isolated from the river channel. Loggers 4 and 14 have the two lowest correlations with logger 6, consistent with their low anomaly results reported in the previous section. We interpret this to mean that they represent portions of Mike Island with higher relative water residence times. It is interesting to note that they both occur in the northeast inner island area, which may point to the presence of a hydrologic barrier to the west of their locations. O'Connor and Moffett (2015) show that the more proximal, northern interior of the nearby Pintail island has layers of more fine grained, lower permeability sediment in the near subsurface that may restrict infiltration related drainage in these regions. The near subsurface of the more distal locations tends to have more coarse, permeable sands that may facilitate greater rates of infiltration related drainage.

Correlation between all logger pairs

This analysis expands on the previous section by considering the correlation coefficients between all logger pairs, which yields additional information about how hydrologically connected various portions of the island are to each other.

Bin 1: Correlation coefficients between 1 and 0.9

Results from Bin 1 show that there is a group of loggers that generally all correlate well with each other as well as with the river channel. This group includes loggers 5, 6, 8, 9, 10, and 13. Logger location 15 is interesting, as it has Bin 1 connections with the three most distal locations (8, 10, and 13), as well as logger 14 which has a poor correlation with the three most distal locations.

Loggers 8, 10, and 13 have the highest number of connections within this group, each having six other Bin 1 connections. Additionally, these three locations have the highest average correlation coefficients in bin 1, with all three locations having a mean correlation of 0.96 with other bin 1 loggers they share a connection with. These three are the most distal locations and the most closely correlated to the primary channel location (logger 6). This indicates that advection leaving the primary channel more directly influences the distal interior areas of Mike Island, where adjacent levees are more subaqueous and hence provide less of a barrier to hydrologic connectivity.

Logger 9 is the northernmost logger, and has the 2nd shallowest mean water depth of any location. In addition, it is in one of the most heavily vegetated inner island logger locations. In light of the close relationship between water depth and ability of incoming solar radiation to

influence the rate of change of water temperature, highlighted in the reference model anomaly portion of this study, along with the ability of heavy vegetation to diminish primary channel momentum flux, one might expect location 9 to have a poor correlation to primary channel water temperature. This is not the case, as logger 9 has five Bin 1 connections, including with the three most connected loggers (8, 10, and 13) and the primary channel location (logger 6). The location of logger 9 is in the vicinity of the outlet of the main northwestern secondary feeder channel, which explains the strong connectivity between logger 9 and the primary channel location. The strong correlation between logger 9 and the three most distal and well connected locations (8, 10, and 13) is further evidence of the high hydrologic connectivity between logger 9 and the primary channel.

Bin 2: Correlation coefficients between 0.9 and 0.8

Five of the six total logger pairs that are in Bin 2 share logger location 15 as a member. Hiatt and Passalacqua (2015) note flow direction reversal in both the inner island and the secondary channels during the rising and falling tides on Mike Island. The location of logger 15 is in an area of the island where levees are moderately well developed, and the bi-directional ebbs and flows of the tidal cycle may play a prominent role in the driving advection. The highest correlation in Bin 2 is between logger 9 and its close neighbor to the south, logger 15. It is interesting to note the discrepancy in the correlations between pairs 9-15, 9-14, and 9-4. Despite being the most proximal locations to logger 9, loggers 4 and 14 share a much lower correlation with logger 9 than the also proximal logger 15. This may be evidence of a feature that limits hydrologic connectivity between loggers 9 and 15 and loggers 4 and 14, which could be in the form of a geomorphic feature, vegetative structure, or advection related phenomena. In this context, the advection of primary channel water in the vicinity of logger 9 through the main northwest feeder channel may be preferentially directed towards logger 15, resulting in the high

correlation between loggers 9 and 15. The relative strength of tides and wind in influencing advection cited in Hiatt and Passalacqua (2015) may play a strong role in the water temperatures at locations 4 and 14 and may be responsible for their poor correlation with locations more hydrologically connected to the primary channel such as loggers 9 and 15.

Bin 3: Correlation coefficients between 0.8 and 0.7

Five of the seven total logger pairs in Bin 3 share logger location 14 in common. The relatively low correlations stemming from location 14 point to poor connectivity between its location and the areas of Mike Island that have been shown to be more influenced by primary channel advection. Location 14 shares Bin 3 connections with loggers 5, 8, 9, 10, and 13, all of which we interpret to be regions with a relatively strong connection with the primary channel. Logger 11 has Bin 3 connectivity with locations 4 and 5, which is interesting given the relative proximity of the three locations.

Bin 4: Correlation coefficients less than 0.7

Logger locations 4 and 11 dominate Bin 4, being a member of six and five pairs respectively. These two locations are the least connected of the logger locations. The relative disconnectivity of logger 4 implies a poor correlation between water temperature time series of logger 4 and those of a majority of the island locations. The three most connected locations identified in Bin 1 (loggers 8, 10, and 13) are all paired with logger 4 in Bin 4, as is the primary channel location (logger 6). This indicates that logger location 4 is a region of Mike Island that is relatively isolated from the influence of water recently advected from the primary channel.

Logger 11 stopped recording data on the 43rd day of the 88 day deployment, meaning our available time series is roughly half as long as all other locations.

Topological Map of Water Temperature Correlation

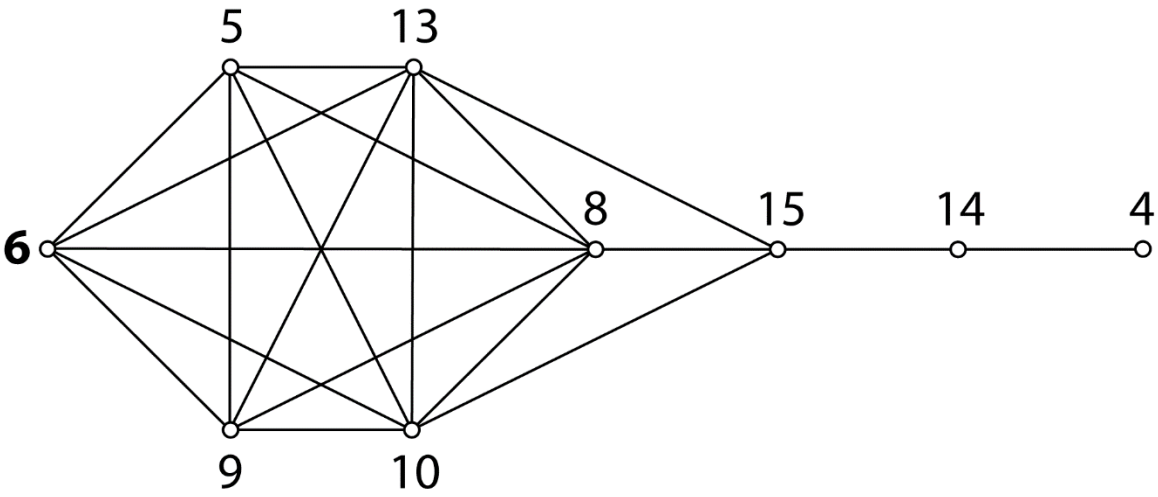

Figure 4: Topological map of water temperature correlation coefficient relationships between data logging locations using correlations greater than 0.90. Logger location 6 is in the primary distributary channel, while the remaining locations are in the interior wetland of Mike Island.

Introduction

We present a topological map (Figure 4) depicting the connections between logger pairs sharing correlation coefficients greater than .90. Topological maps are a graphical means to depict spatial connections in complex data in a simplified form. Perhaps the most recognizable example of a topological map is a subway map, such as that of New York City. Lengths of lines or connections in topological maps are not scaled to or representative of real distances, and are not directionally specific. For example, on a subway map the distance between points is typically not directly scaled to the actual distance between stations. Instead, the goal is to present relative locations and connections as clearly as possible. Similarly, in our topological map the length of a connection between logger pairs does not relate to a specific value and is not indicative of how strong or weak the correlation between that pair is, but merely that the correlation between the

pair is greater than 0.90. Subway maps also do not typically depict a specific direction. The same subway map applies whether the commuter is heading east bound or west bound, it is only the order of stations that changes based on direction. In the case of our topological map, direction also has no value as each connected logger pair shares the same single correlation coefficient (i.e. 6-8 is the same as 8-6).

Results

The topological map in Figure 4 shows a clear connectivity between a large subset of loggers that includes loggers 5, 6, 8, 9, 10, and 13. Each one of these six loggers shares a correlation coefficient greater than 0.90 with each of the other five locations in this core group. Within this group, loggers 5, 6, and 9 each have five total connections, all of which are within this core group. Loggers 8, 10, and 13 each have six total connections, consisting of five connections with the core group and a sixth connection to logger 15. Logger 15 has four total connections, consisting of three connections to core group members (loggers 8, 10, and 13) and one connection to logger 14. Logger 14 has two connections (4 and 15), while logger 4 has only the single connection to logger 14.

Discussion

The members of the highly connected core group we interpret as not only highly hydrologically connected to each other, but also highly hydrologically connected to the river channel. This is evidenced by all members of the group sharing a topological connection with logger 6, which is measures river channel temperature. We conclude that these loggers in are in areas of Mike Island where the advection of river channel water onto the island dominates the hydrology, and are therefore areas where water residence times are relatively low.

Loggers 14 and 4 have significantly less topological connection than the other seven logger locations, which we take as representing areas of the island where hydrologic connections are of a relatively lower magnitude. These represent inner island locations where water residence times are relatively greater.

Logger 15 connects with several members of the core group, as well as the relatively sparingly connected logger 14. This suggests that location 15 represents a transitional location between highly advective areas and more hydrologically isolated areas of the island.

It is interesting to compare the topological connections map with the actual map of Mike Island logger locations, particularly the 15 to 14 to 4 locations. In this context it appears that the northeast portion of the inner island is the most hydrologically isolated of the locations studied. We mentioned previously that the water depth time series indicates that a pool of water often remains at logger location 4 during low tide periods, even when more distal logger locations go dry. The presence of an isolated pool in the vicinity of logger location 4 is consistent with the conclusion of relatively longer water residence time that we reach using the topological map of correlation coefficients. The actual location of logger location 14, taken with its position in the topological study, shows it to be a location that links the more isolated area near logger 4 with some of the more hydrologically connected areas of the inner island. We view location 14 as a station in a pathway of water either entering the northeastern isolated region or leaving it.

Relating correlation coefficient and distance between logger pairs

Method

Next, we attempt to relate the distance between logger pairs to their correlation coefficient. We use ArcMap to determine the distance between the field measured GPS locations of each logger location. We then normalize matrices of distance between every logger pair and correlation coefficients between each logger pair to a range of 0-1 using the following equation:

$$z_i = \frac{x_i - \min(x)}{\max(x) - \min(x)} \qquad \text{Equation 14}$$

where z_i is the normalized value, x_i is the original value, $\min(x)$ is the minimum value in the dataset, and $\max(x)$ is the maximum value in the dataset.

As a means of assessing the extremes of the normalized dataset distribution, the normalized correlation coefficient matrix and the normalized distance matrix were each shifted so that they are centered on 0 and range from 0.5 to -0.5, by subtracting 0.5 from all values. We then compute the product of the zero-centered normalized matrices.

Results

In the analysis of the product of the zero-centered normalized correlation coefficient and distance matrices, we present the highest ten results along with the corresponding zero-centered normalized correlation coefficient and distance values in Table 2. We present matrices of distance between logger pairs, normalized distance between logger pairs, zero-centered normalized distance between logger pairs, normalized correlation coefficients between logger pairs, and zero-centered normalized correlation coefficients between logger pairs in Appendix J.

Top Ten Products			
Logger Pair	Product	Normalized Correlation Coefficient	Normalized Distance
6-8	0.23	0.47	0.50
6-10	0.23	0.47	0.48
8-9	0.18	0.40	0.44
9-10	0.15	0.37	0.41
4-9	0.14	-0.36	-0.38
4-6	0.12	-0.46	-0.27
4-5	0.12	-0.42	-0.29
6-13	0.12	0.46	0.25
6-14	0.09	-0.23	-0.38
9-11	0.08	-0.48	-0.18

Table 2: Top Ten Products of Normalized Correlation Coefficient and Normalized Distance between Logger Pairs

Of the 10 logger pairs presented, 5 values result from the product of positive values and 5 values result from the product of negative values.

Discussion

This analysis uses the product of the zero-centered normalized correlation coefficient and distance matrices to identify surprising results. The null hypothesis is that there will be a negative relation between distance and correlation coefficient, where logger locations that are close to each other show stronger water temperature correlation coefficients and those that are further away from each other show weaker correlation coefficients. By categorizing the largest products of the zero-centered normalized matrices, we identify locations that do not conform to the null hypothesis. As can be seen in Table 2, high products result from either the combination a relatively large distance between logger location and relatively strong correlation coefficient or the combination of a relatively small distance between logger location and relatively weak correlation coefficient.

The two highest products are found between logger pairs 6-8 and 6-10, and are the result of the combination of a relatively large distance and a relatively strong correlation. The location of logger 6 is along the northeast edge of Mike Island and is meant to capture a representative water temperature for the primary delta distributary channel running along the western edge of Mike Island, while loggers 8 and 10 are inner island locations found at the most distal portion of Mike Island. Loggers 6 and 8 are the most distant logging locations, and loggers 6 and 10 are the second most distant pair. The relatively strong correlation between logger 6 and loggers 8 and 10 reflects a strong hydrologic connection between the primary channel and the southern end of Mike Island. This is likely due to a generally decreasing effectiveness of the natural levees along the edge of Mike Island in separating the primary channel water and the inner island water as you travel toward the distal end of the island. The third and fourth largest products are found between logger pairs 8-9 and 9-10, and are again the result of the combination of a relatively large distance between locations and a relatively strong correlation coefficient. Logger 9 is in the north-central portion of Mike Island, and more specifically is near the outlet of a tidal channel linking the interior of the island with the western primary distributary channel. We hypothesize that this secondary tidal channel contributes a supply of primary distributary channel water to the interior of the island. The relatively large product between the zero-centered normalized correlation coefficients and distances of logger pairs 8-9 and 9-10, when considered alongside the conclusions reached in analyzing logger pairs 6-8 and 6-10, indicate that primary distributary channel water plays a strong role in dictating the water temperature of both the distal end of Mike Island and the northern portion of the island near logger 9.

The fifth through seventh highest products represent logger pairs where a relatively short distance is combined with a relatively weak water temperature correlation coefficient, and are associated with logger pairs 4-9, 4-6, and 4-5. Logger 4 is an inner island location along the

north-east portion of Mike Island, and logger 5 is an inner island location in the west-central portion of Mike Island. Although these loggers are relatively close to each other, they do not share a strong water temperature correlation.

Logger pair 6-13 yields the eighth highest product, the result of a relatively high distance and strong water temperature correlation. Logger 13 is along the south-western inner island edge, roughly 1 km north of logger location 8. The zero-centered normalized water temperature correlation coefficient between loggers 8 and 13 is slightly lower, but very similar to the highest products in the dataset found between logger pairs 6-8 and 6-10. Pair 6-13 have the eighth highest product primarily due to the location of logger 13 being roughly 1 km closer to logger 6 than loggers 8 and 10 are.

Logger pairs 6-14 and 9-11 contribute the ninth and tenth highest products, and both are the result of combining negative zero-centered normalized distance and correlation coefficient values. Although they share nearly identical products (0.086 and 0.085 respectively), they differ in how they get to that product. The product of logger pair 6-14 is mostly driven by a relatively short distance between the two locations, coupled with a moderately poor water temperature correlation. The product of logger pair 9-11 is buoyed by the second weakest water temperature correlation coefficient in the data set, coupled with a moderate distance value.

CONCLUSIONS

We have presented several methods that use analysis of water temperature time series to reveal details of the hydrologic connectivity between a primary distributary channel and the interior wetland of an adjacent interdistributary island on Wax Lake Delta. These distinctly different methods yield similar conclusions regarding the hydrologic connectivity between the

primary distributary channel and the interior of Mike Island. Distal regions of Mike Island show a high degree of connectivity with the primary distributary channel, yielding short water residence times. Proximal locations show differing levels of connectivity to the primary distributary channel depending on proximity to various advection influencing structures. The northeast interior of Mike Island is relatively isolated from primary channel advection. The presence of a hydrologic barrier that allows persistent standing water in the area contributes to longer residence time for water in this region of the island. At our data logging location in the northwest interior of the island, we find that a secondary feeder channel bisecting the western island edge levee plays a prominent role in maintaining a high degree of hydrologic connectivity to the primary distributary channel. Furthermore, we show that the use of a simple, inexpensive, and open source data logging platform can generate high quality continuous field data, allowing enhanced spatial data coverage for a fraction of the price of conventional systems. We show the utility of using a reference model to accurately describe a component of a more complex system, and deduct useful information about the difference between our reference model and field measured observations.

REFERENCES

Campbell, G. S. & Norman, J. M. *Introduction to environmental biophysics*. (Springer, 1998).

Carle, M. V., Sasser, C. E. & Roberts, H. H. Accretion and Vegetation Community Change in Wax Lake Delta Following the Historic 2011 Mississippi River Flood. *Journal of Coastal Research* **313,** 569–587 (2015).

Cogley, J. G. The Albedo of Water as a Function of Latitude. *Monthly Weather Review* **107,** 775–781 (1979).

Duffie, J. A. & Beckman, W. A. *Solar Engineering of Thermal Processes*. (J Wiley and Sons, New York).

Gul, M. S., Muneer, T. & Kambezidis, H. D. Models for obtaining solar radiation from other meteorological data. *Solar Energy* **64,** 99–108 (1998).

Henry, K. M. & Twilley, R. R. Nutrient Biogeochemistry During the Early Stages of Delta Development in the Mississippi River Deltaic Plain. *Ecosystems* **17,** 327–343 (2014).

Hiatt, M. & Passalacqua, P. Hydrological connectivity in river deltas: The first-order importance of channel-island exchange: Connectivity in river deltas. *Water Resources Research* **51,** 2264–2282 (2015).

Ji, Z.-G. *Hydrodynamics and water quality: modeling rivers, lakes, and estuaries*. (Wiley-Interscience, 2008).

Kasten, F. & Czeplak, g. Solar and terrestrial radiation dependent on the amount and type of cloud. *Solar Energy* **24,** 177–189 (1980).

Kelley, C. *et al.* An Affordable Open-Source Turbidimeter. *Sensors* **14,** 7142–7155 (2014).

Kustas, W. P., Rango, A. & Uijlenhoet, R. A simple energy budget algorithm for the snowmelt runoff model. *Water Resources Research* **30,** 1515–1527 (1994).

Laks, H., Dmochowski, J. R. & Couch, N. P. The relationship between muscle surface pH and oxygen transport. *Ann. Surg.* **183,** 193–198 (1976).

Lane, R. R., Madden, C. J., Day Jr., J. W. & Solet, D. J. Hydrologic and nutrient dynamics of a coastal bay and wetland receiving discharge from the Atchafalaya River. *Hydrobiologia* 658:55-66 (2011).

Leeuw, T., Boss, E. & Wright, D. In situ Measurements of Phytoplankton Fluorescence Using Low Cost Electronics. *Sensors* **13,** 7872–7883 (2013).

Li, C., Roberts, H., Stone, G. W., Weeks, E. & Luo, Y. Wind surge and saltwater intrusion in Atchafalaya Bay during onshore winds prior to cold front passage. *Hydrobiologia* 658:27-39 (2011).

Luo, L., Hamilton, D. & Han, B. Estimation of total cloud cover from solar radiation observations at Lake Rotorua, New Zealand. *Solar Energy* **84,** 501–506 (2010).

Muneer, T. & Gul, M. S. Evaluation of sunshine and cloud cover based models for generating solar radiation data. *Energy Conversion and Management* 461–482 (2000).

O'Connor, M. T. & Moffett, K. B. Groundwater dynamics and surface water–groundwater interactions in a prograding delta island, Louisiana, USA. *Journal of Hydrology* **524,** 15–29 (2015).

Paaijmans, K. P., Heusinkveld, B. G. & Jacobs, A. F. G. A simplified model to predict diurnal water temperature dynamics in a shallow tropical water pool. *International Journal of Biometeorology* **52,** 797–803 (2008).

Partridge, G. W. & Platt, C. M. R. *Radiative Processes in Meteorology and Climatology.*

Paulescu, M., Paulescu, E., Gravila, P. & Badescu, V. *Weather Modeling and Forecasting of PV Systems Operation*. (2013).

Paola, C., Twilley, R. R., Edmonds, D. A., Kim, W., Mohrig, D., Parker, G., Voller, V. R. Natural Processes in Delta Restoration: Application to the Mississippi Delta. *Annual Review of Marine Science*, **3(1)**, 67–91 (2011).

Power, M. E., Brozović, N., Bode, C. & Zilberman, D. Spatially explicit tools for understanding and sustaining inland water ecosystems. *Frontiers in Ecology and the Environment* **3,** 47–55 (2005).

Reno, M. J. & Stein, J. Using cloud classification to model solar variability. in *ASES National Solar Conference, Baltimore, MD* (2013).

Shaw, J. B. & Mohrig, D. The importance of erosion in distributary channel network growth, Wax Lake Delta, Louisiana, USA. *Geology* **42,** 31–34 (2014).

Shaw, J. B., Mohrig, D. & Wagner, R. W. Flow patterns and morphology of a prograding river delta: DELTA FLOW PATTERNS. *Journal of Geophysical Research: Earth Surface* **121,** 372–391 (2016).

Smesrud, J. K., Boyd, M. S., Cuenca, R. H. & Eisner, S. L. A mechanistic energy balance model for predicting water temperature in surface flow wetlands. *Ecological Engineering* **67,** 11–24 (2014).

Theriot, J. M., Conkle, J. L., Reza Pezeshki, S., DeLaune, R. D. & White, J. R. Will hydrologic restoration of Mississippi River riparian wetlands improve their critical biogeochemical functions? *Ecological Engineering* **60,** 192–198 (2013).

Wagner, R. W., Stacey, M., Brown, L. R. & Dettinger, M. Statistical Models of Temperature in the Sacramento–San Joaquin Delta Under Climate-Change Scenarios and Ecological Implications. *Estuaries and Coasts* **34,** 544–556 (2011).

Wellner, R., Beaubouef, R., Van Wagoner, J., Roberts, H. & Tao, S. Jet-Plume Depositional Bodies - The Primary Building Blocks of Wax Lake Delta. *Gulf Coast Association of Geological Societies Transactions* **55,** 867–909 (2005).

Wickert, A. D. The ALog: Inexpensive, Open-Source, Automated Data Collection in the Field. *Bulletin of the Ecological Society of America* **95(2),** 68–78

Wood, S. L., Wheeler, E. F., Berghage, R. D. & Graves, R. E. Temperature effects on wastewater nitrate removal in laboratory-scale constructed wetlands. *Transactions of the ASAE* **42,** 185 (1999).

Appendix A: Clear Sky Radiation Model

Incoming shortwave solar radiation is the dominant term controlling the diurnal warming of shallow surface waters. We construct a clear sky radiation model for the field site (Mike Island, Wax Lake Delta, LA) over the length of the deployment that provides a theoretical maximum of incoming shortwave radiation at minute intervals. We create our clear sky model following the process outlined in Campbell and Norman (1998) as follows.

$$\cos\psi = \sin\beta = \sin\phi\sin\delta + \cos\phi\cos\delta\cos[15(t - t_0)] \quad \textbf{(Equation A.1)}$$

where ψ is the solar zenith angle measured in degrees from vertical, β is the altitude angle of the sun as measured in degrees above the horizon, ϕ is the latitude, δ is the solar declination, t is the standard local time in decimal hours, and t_0 is the time of solar noon (Campbell and Norman, 1998).

$$\sin\delta = 0.39785\ \sin[278.97 + 0.9856J + 1.9165\ \sin(356.6 + 0.9856J)] \quad \textbf{(Equation A.2)}$$

where J is the Julian day, the number of days since January 1 of that year.

$$t_0 = 12 - LC - ET \quad \textbf{(Equation A.3)}$$

where $\boldsymbol{LC}$ is a longitude correction that adjusts for site position relative to the nearest meridian, and $\boldsymbol{ET}$ is the equation of time which is found using

$$\boldsymbol{ET} = \left(\frac{-104.7sin\, f + 596.2sin\, 2f + 4.3sin3f - 12.7sin4f - 429.3cosf - 2.0cos2f + 19.3cos3f}{3600}\right)$$

(Equation A.4)

where $\boldsymbol{f}$ is in degrees and is found using

$$\boldsymbol{f = 279.575 + 0.9856\, J}$$ **(Equation A.5)**

The next step in creating the clear sky radiation model is to calculate the amount of incident extra-terrestrial shortwave radiation at the top of the atmosphere, $\boldsymbol{I_o}$ using a method from Partridge and Platt (1976)

$$\boldsymbol{I_o = 1367\left(\frac{R_{av}}{R}\right)^2}$$ **(Equation A.6)**

where $\boldsymbol{R_{av}}$ is the annual mean distance between the earth and the sun while $\boldsymbol{R}$ is the actual distance between the earth and the sun based on the day of the year, found by

$$\left(\frac{\boldsymbol{R_{av}}}{\boldsymbol{R}}\right)^{\mathbf{2}} = \mathbf{1.00011} + \mathbf{0.034221}\ \boldsymbol{cos}\ \boldsymbol{b} + \mathbf{0.001280}\ \boldsymbol{sin}\ \boldsymbol{b} + \mathbf{0.000719}\ \boldsymbol{cos}\ \mathbf{2}\boldsymbol{b} + \mathbf{0.000077}\ \boldsymbol{sin}\ \mathbf{2}\boldsymbol{b}$$

(Equation A.7)

where $\boldsymbol{b}$ is found by

$$\boldsymbol{b} = \frac{\mathbf{2}\ \boldsymbol{\pi}\ \boldsymbol{J}}{\mathbf{365}} \qquad \textbf{(Equation A.8)}$$

Once the solar zenith angle and extraterrestrial shortwave radiation are found, several components of shortwave solar radiation can be calculated for a given site through time. $\boldsymbol{S_p}$ is the direct irradiance as measured on an imaginary plane perpendicular to the beam, $\boldsymbol{S_b}$ is the direct beam irradiance, $\boldsymbol{S_d}$ is the diffuse beam irradiance, and $\boldsymbol{S_t}$ is the total irradiance occurring on a horizontal surface. These components are found by the following relationships

$$\boldsymbol{S_p} = \boldsymbol{I_o}\ \boldsymbol{\tau^m} \qquad \textbf{(Equation A.9)}$$

$$\boldsymbol{S_b} = \boldsymbol{S_p}\ \boldsymbol{cos}\ \boldsymbol{\psi} \qquad \textbf{(Equation A.10)}$$

$$\boldsymbol{S_d} = \mathbf{0.3}(\mathbf{1} - \boldsymbol{\tau^m})\boldsymbol{I_o}\ \boldsymbol{cos}\ \boldsymbol{\psi} \qquad \textbf{(Equation A.11)}$$

$$S_t = S_b + S_d \qquad \textbf{(Equation A.12)}$$

where τ is the atmospheric transmissivity and m is the optical air mass number. A value of $\tau = 0.75$ was used, which Norman and Campbell (1998) point out is representative of a very clear sky. m was calculated using

$$m = \frac{p_a}{101.3\ cos\ \psi} \qquad \textbf{(Equation A.13)}$$

where p_a is the atmospheric pressure as found by

$$p_a = 101.3\ exp(-1/8200) \qquad \textbf{(Equation A.14)}$$

The final step in determining how much clear sky shortwave radiation is reaching the water at the field site is to model the effect of albedo to determine how much of the total radiation is being reflected off of the water surface. Following a method put forth in Cogley (1979), the first step is to find the Fresnel albedo, a_f which is a simplified approximation assuming direct radiation upon a horizontal plane of pure water and is found by

$$a_f = 50\left(\frac{sin^2(Z-r)}{sin^2(Z+r)} + \frac{tan^2(Z-r)}{tan^2(Z+r)}\right) \qquad \textbf{(Equation A.15)}$$

where Z is the zenith angle and r is the angle of refraction found respectively by

$$Z = cos^{-1}(cos\,\psi) \qquad \textbf{(Equation A.16)}$$

$$r = sin^{-1}\left(\frac{sin\,Z}{1.33}\right) \qquad \textbf{(Equation A.17)}$$

Finally, the albedo percent a_p can be found using

$$a_p = 1 - \left(\frac{a_f}{100}\right) \qquad \textbf{(Equation A.18)}$$

Appendix B: Field Measured Water Temperature

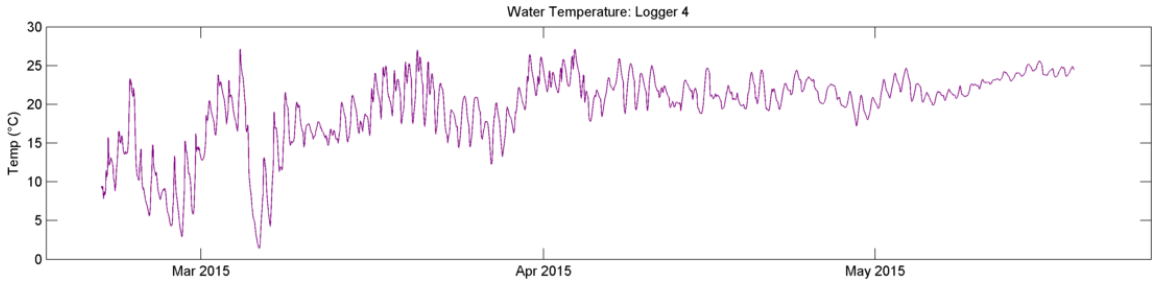

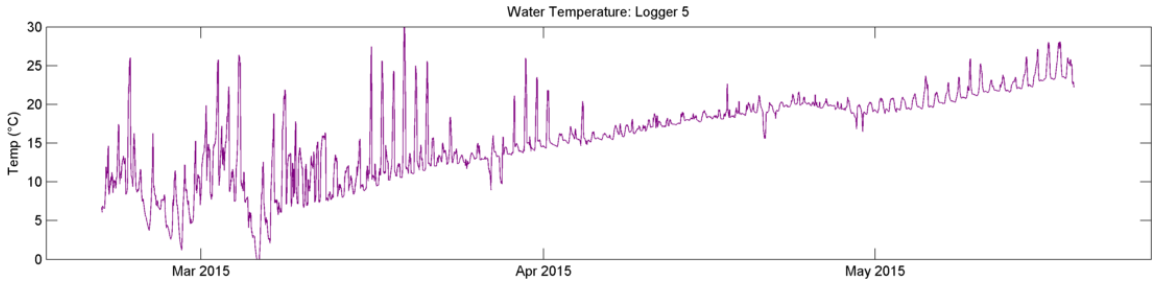

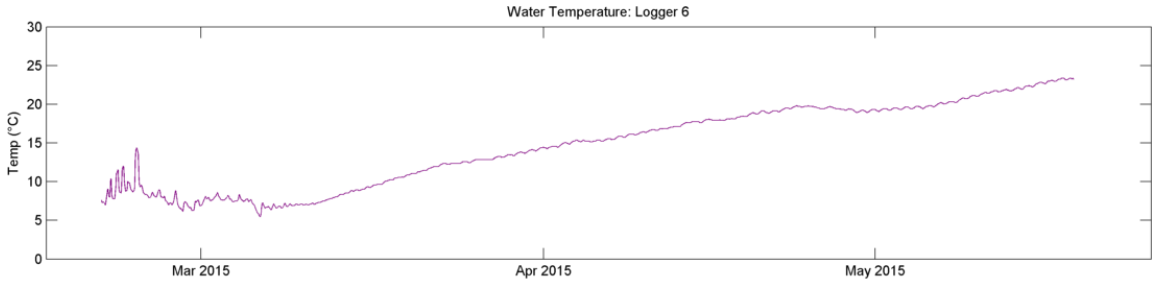

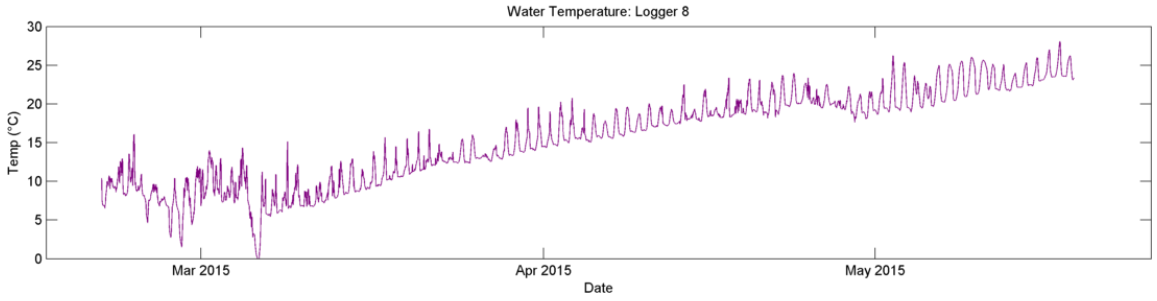

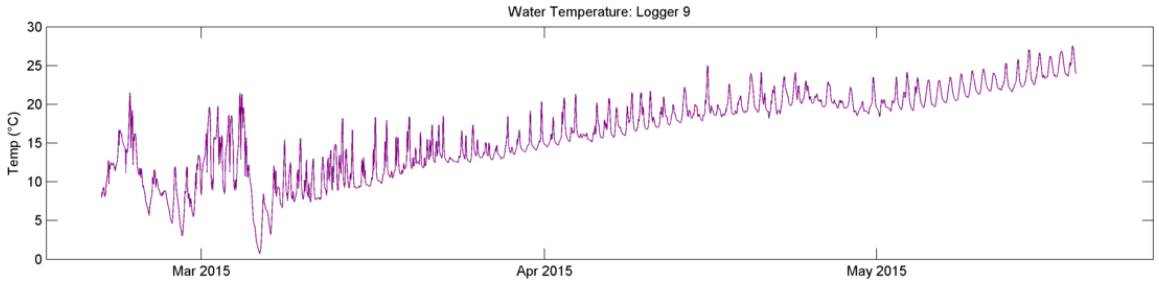
Water Temperature: Logger 9
Temp (°C)
0
5
10
15
20
25
30
Mar 2015
Apr 2015
May 2015

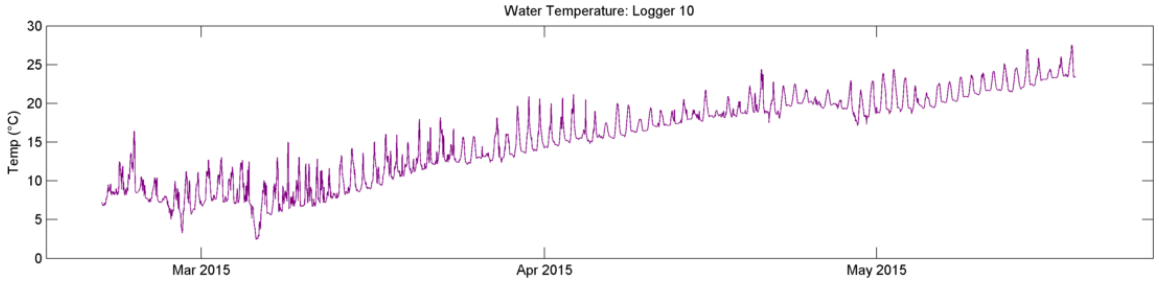
Water Temperature: Logger 10
Temp (°C)
0
5
10
15
20
25
30
Mar 2015
Apr 2015
May 2015

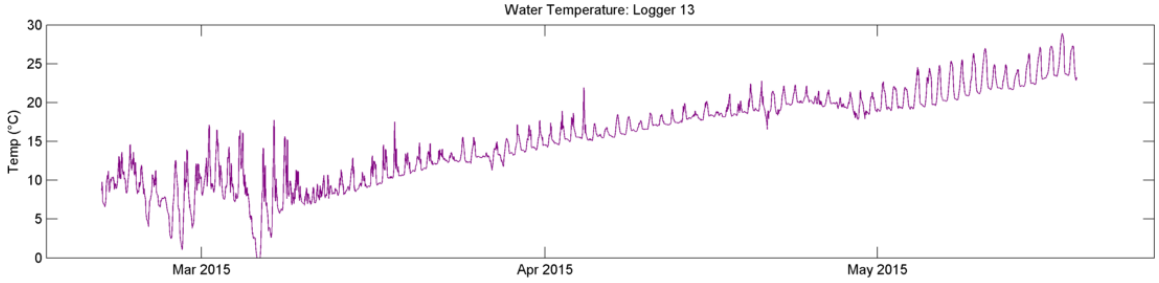
Water Temperature: Logger 13
Temp (°C)
0
5
10
15
20
25
30
Mar 2015
Apr 2015
May 2015

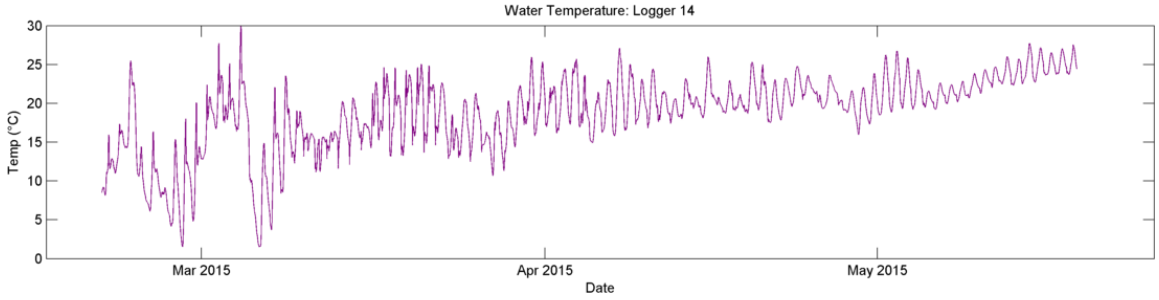
Water Temperature: Logger 14
Temp (°C)
0
5
10
15
20
25
30
Mar 2015
Apr 2015
May 2015
Date

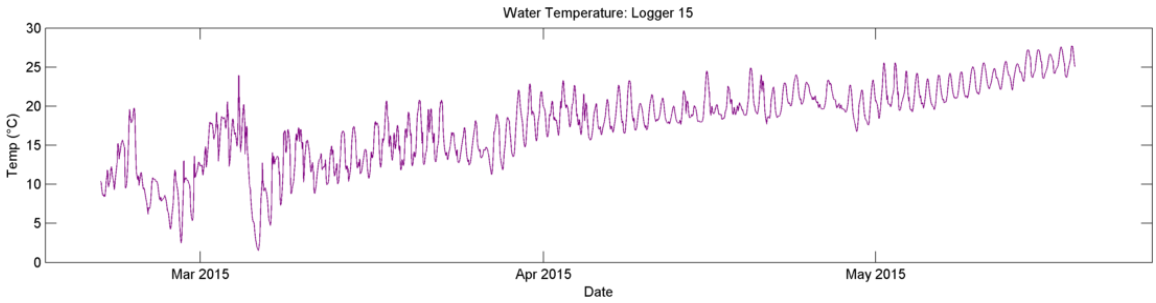
Water Temperature: Logger 15
Temp (°C)
30
25
20
15
10
5
0
Mar 2015
Apr 2015
May 2015
Date

Appendix C: Field Measured Water Depth

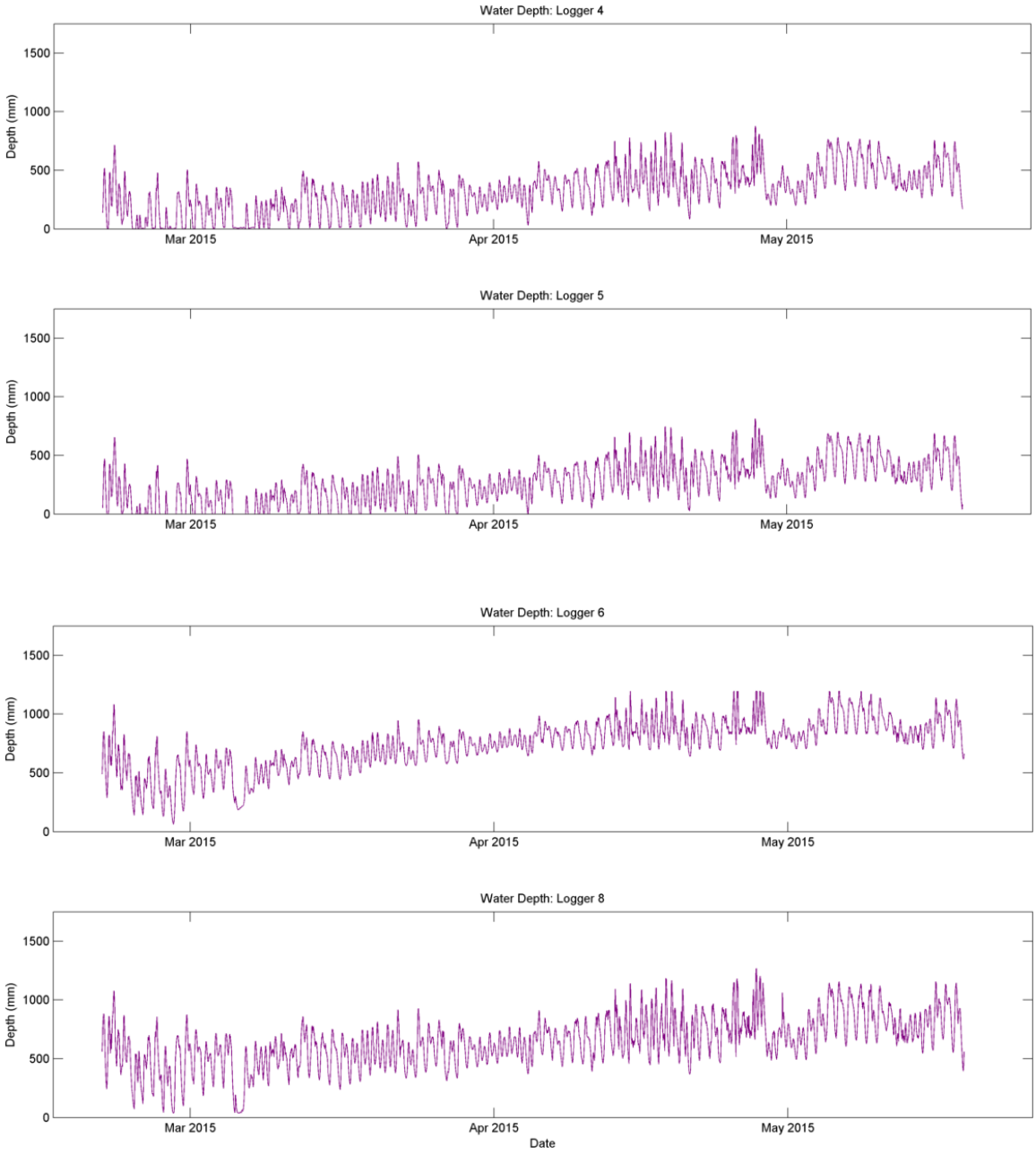

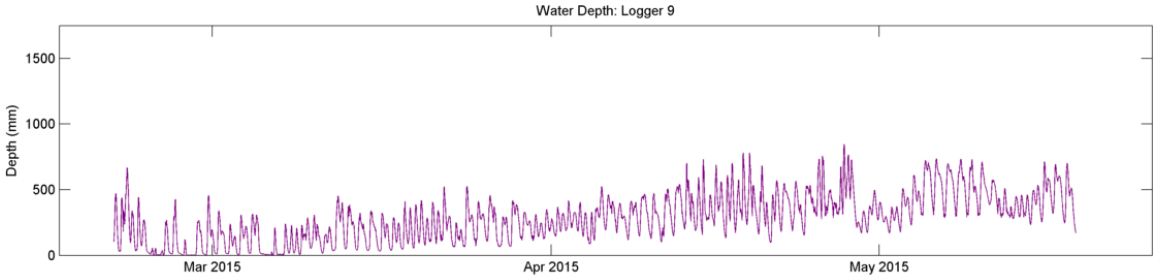
Water Depth: Logger 9
Depth (mm)
1500
1000
500
0
Mar 2015
Apr 2015
May 2015

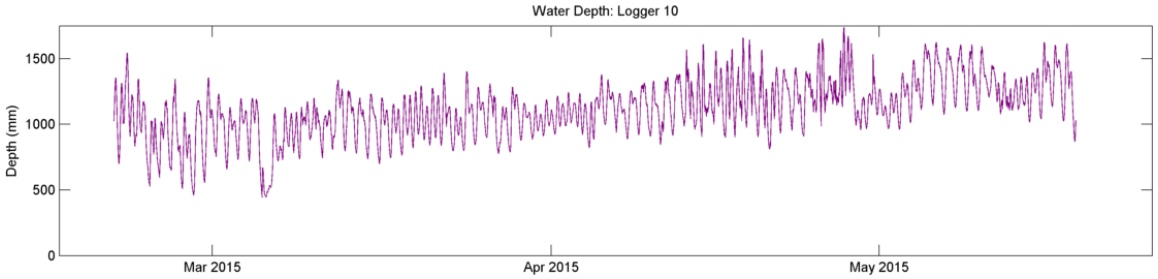
Water Depth: Logger 10
Depth (mm)
1500
1000
500
0
Mar 2015
Apr 2015
May 2015

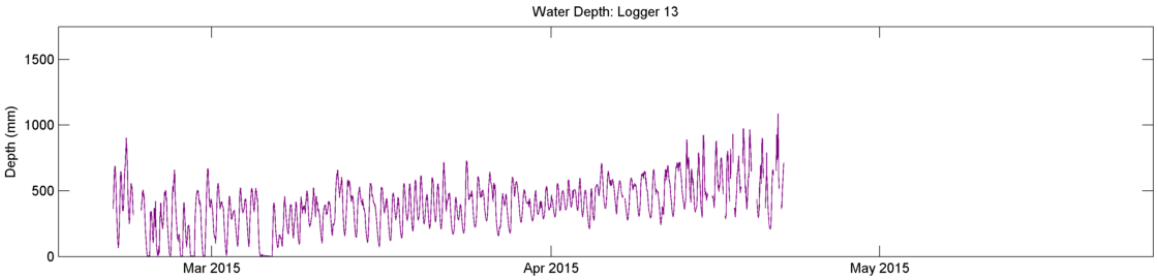
Water Depth: Logger 13
Depth (mm)
1500
1000
500
0
Mar 2015
Apr 2015
May 2015

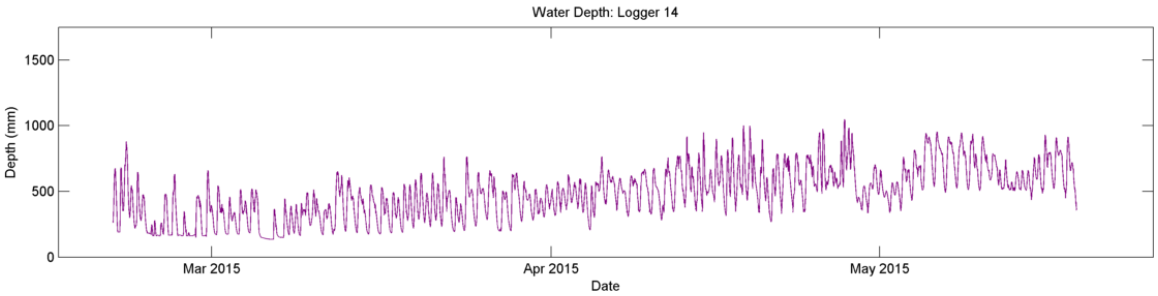
Water Depth: Logger 14
Depth (mm)
1500
1000
500
0
Mar 2015
Apr 2015
May 2015
Date

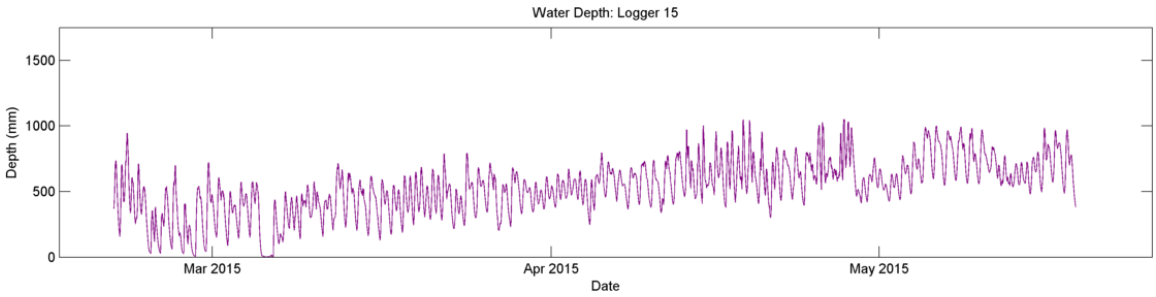

Logger	Mean Depth (mm)
10	987.09
6	589.41
8	514.12
15	396.72
14	353.91
13	335.27
4	195.05
9	166.16
5	149.58

Table C.1: Mean Depth, Pyranometer Length Deployment (43 Days)

Logger	Mean Depth (mm)
10	1108.22
6	736.14
8	637.84
15	527.79
14	480.55
13	384.28
4	317.06
9	281.55
5	261.38

Table C.2: Mean Depth, Full Length Deployment (88 Days)

Appendix D: Predicted Water Temperature vs. Measured Water Temperature using Field Measured Shortwave Solar Radiation

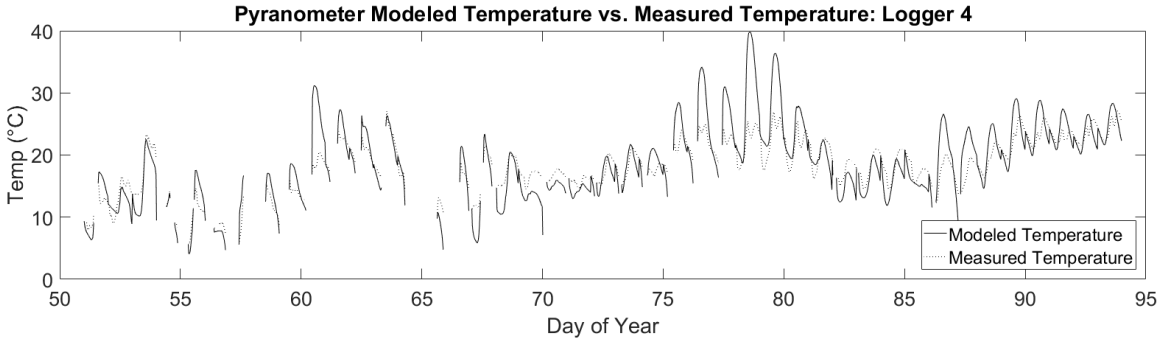

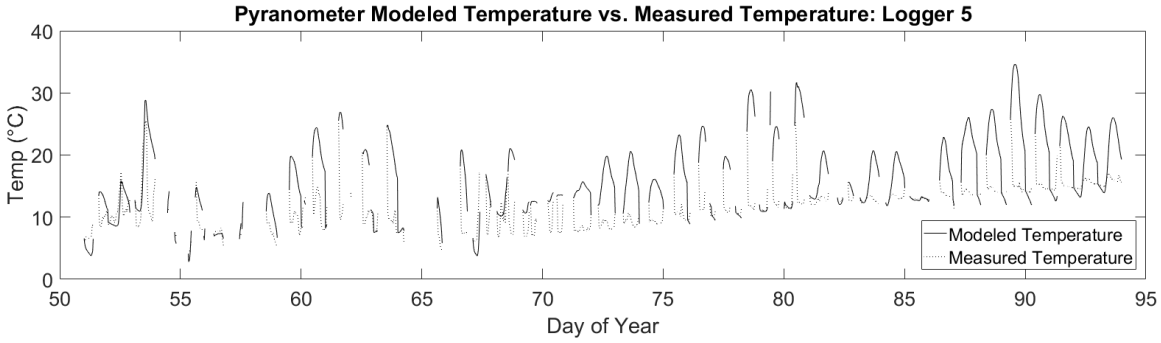

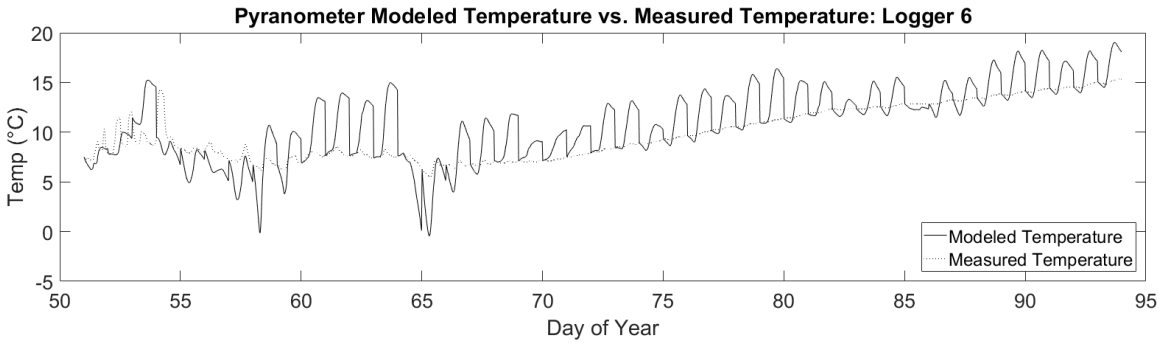

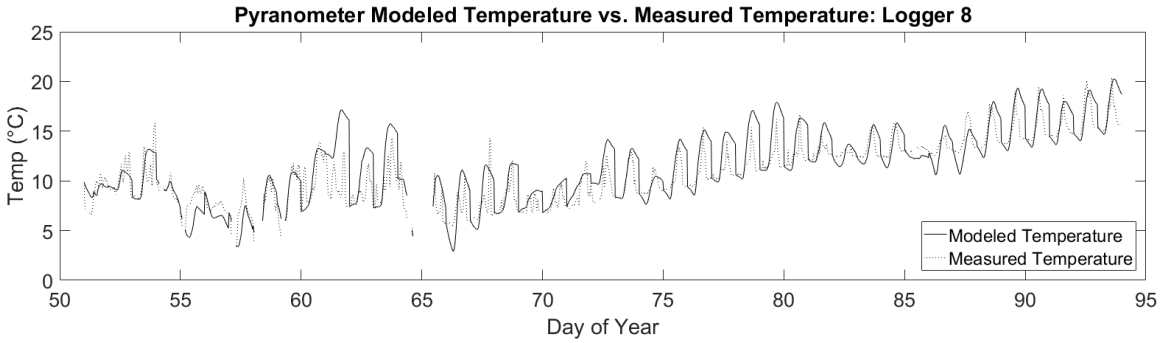
Pyranometer Modeled Temperature vs. Measured Temperature: Logger 8
Temp (°C)
Day of Year
Modeled Temperature
Measured Temperature

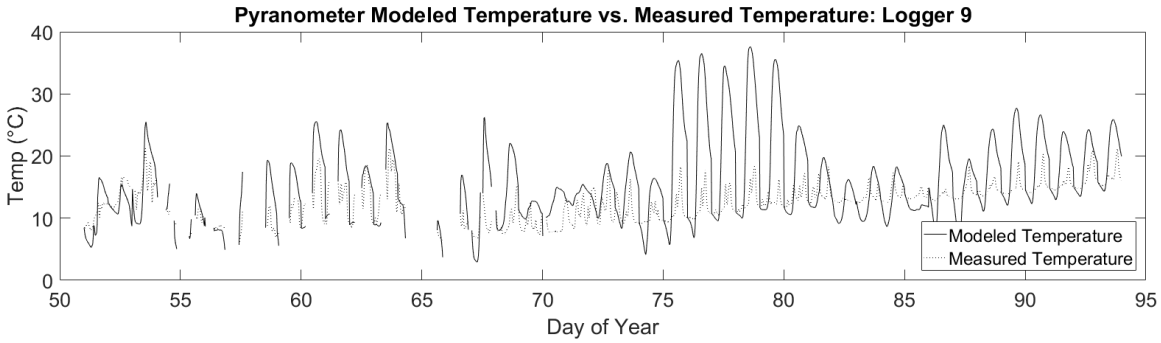
Pyranometer Modeled Temperature vs. Measured Temperature: Logger 9
Temp (°C)
Day of Year
Modeled Temperature
Measured Temperature

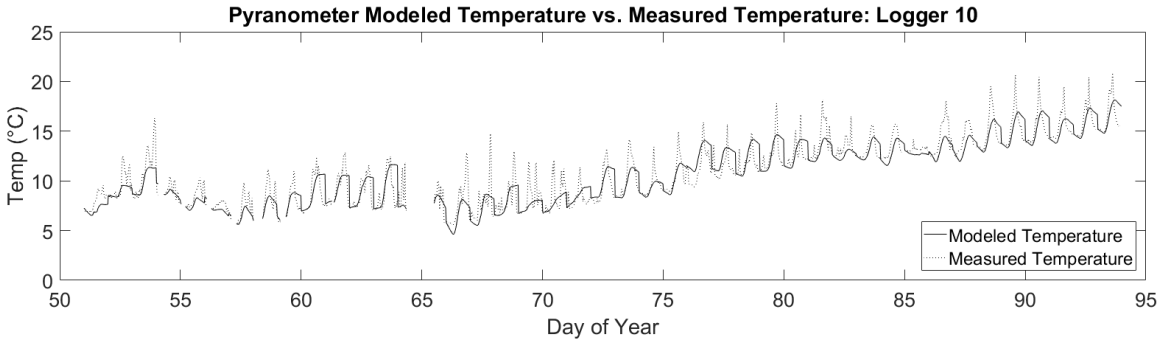
Pyranometer Modeled Temperature vs. Measured Temperature: Logger 10
Temp (°C)
Day of Year
Modeled Temperature
Measured Temperature

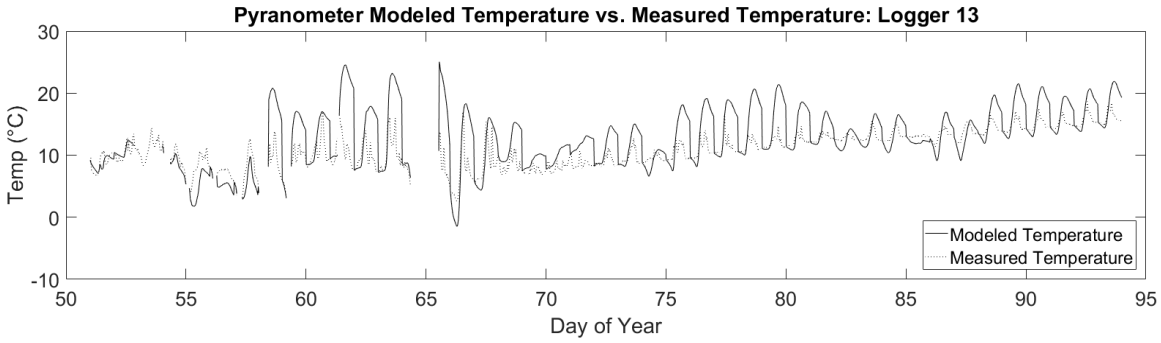
Pyranometer Modeled Temperature vs. Measured Temperature: Logger 13
Temp (°C)
Day of Year
Modeled Temperature
Measured Temperature

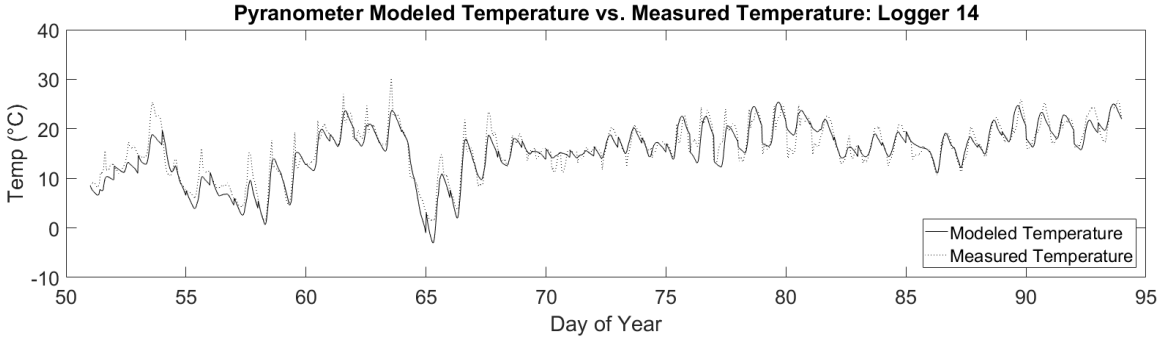
Pyranometer Modeled Temperature vs. Measured Temperature: Logger 14
Temp (°C)
Day of Year
Modeled Temperature
Measured Temperature

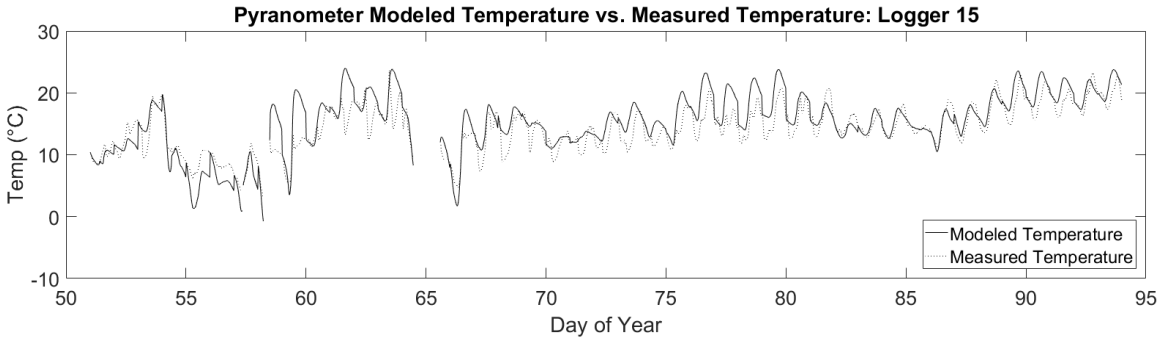
Pyranometer Modeled Temperature vs. Measured Temperature: Logger 15
Temp (°C)
Day of Year
Modeled Temperature
Measured Temperature

Appendix E: Predicted Water Temperature vs. Measured Water Temperature using Cloud Cover Radiation Model

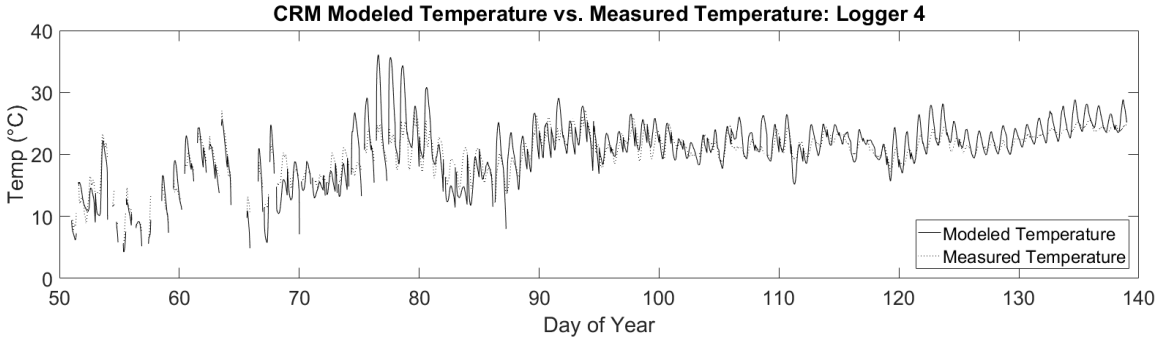

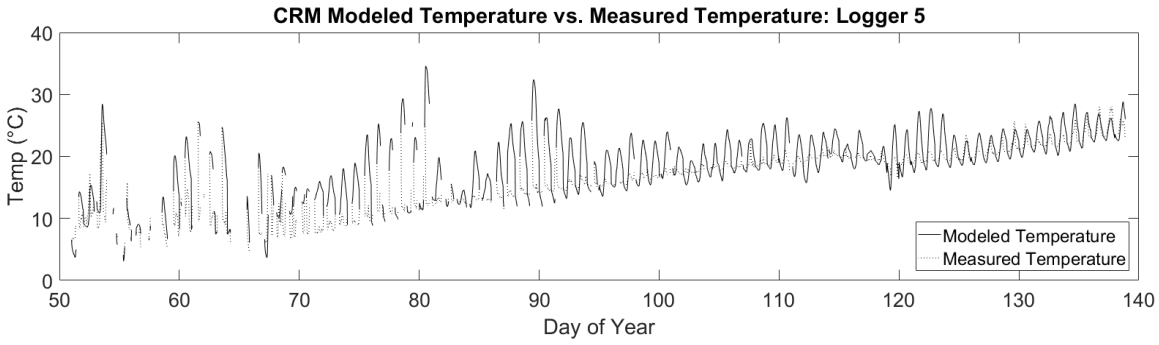

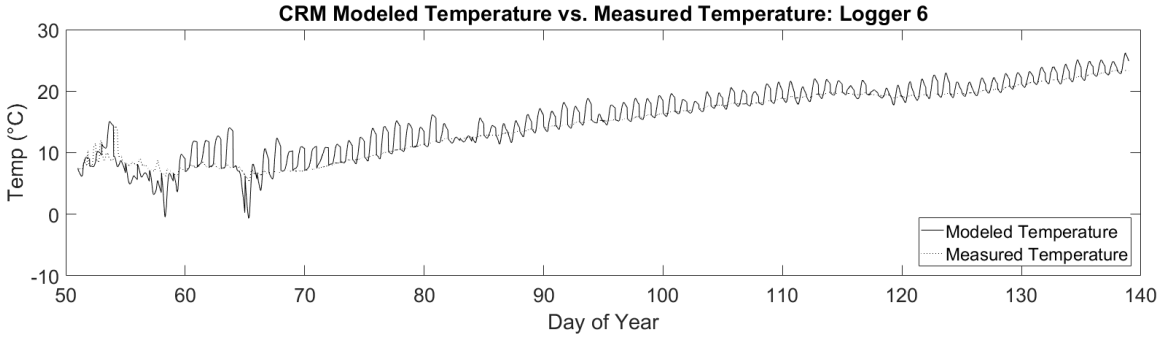

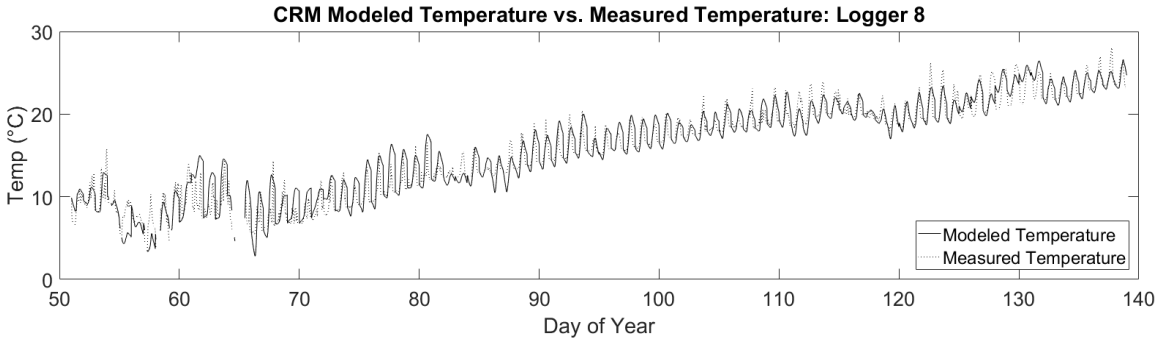

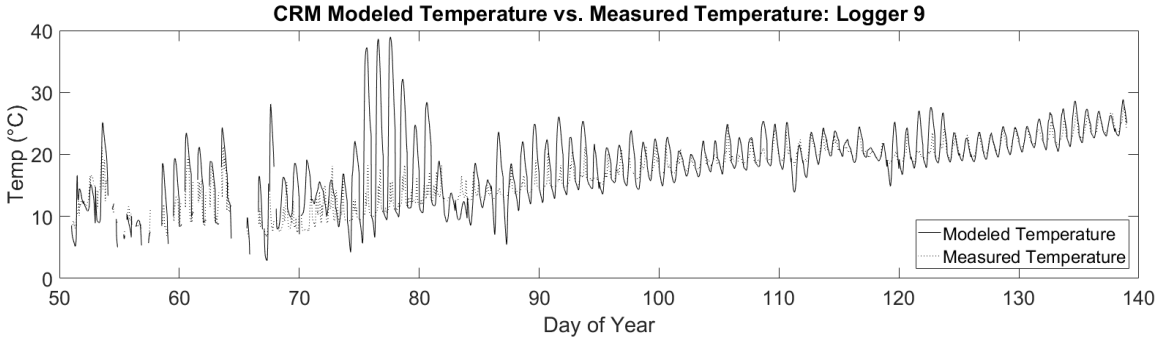
CRM Modeled Temperature vs. Measured Temperature: Logger 9
Temp (°C)
Day of Year
Modeled Temperature
Measured Temperature

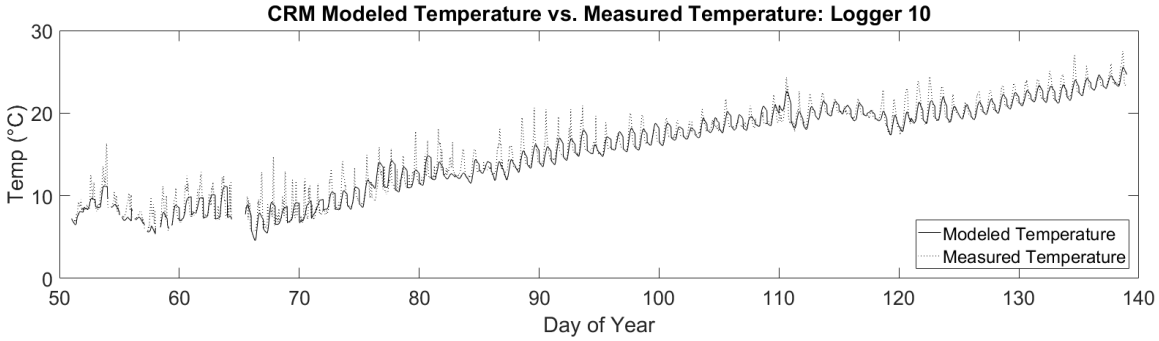
CRM Modeled Temperature vs. Measured Temperature: Logger 10
Temp (°C)
Day of Year
Modeled Temperature
Measured Temperature

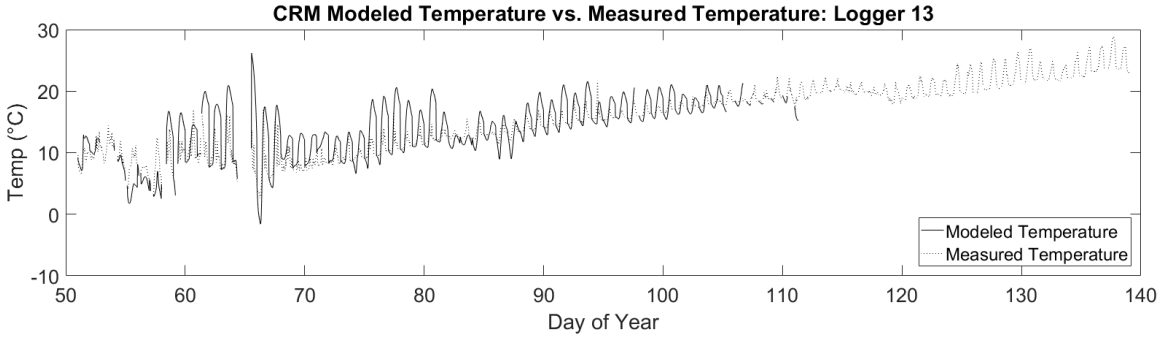
CRM Modeled Temperature vs. Measured Temperature: Logger 13
Temp (°C)
Day of Year
Modeled Temperature
Measured Temperature

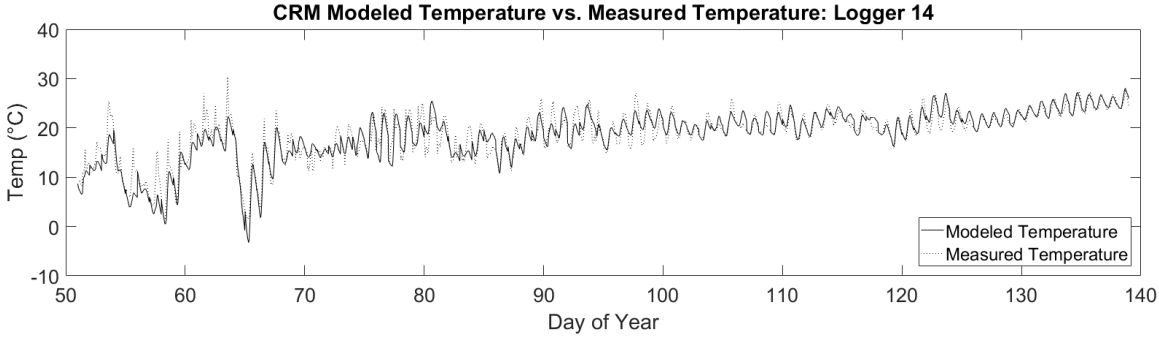
CRM Modeled Temperature vs. Measured Temperature: Logger 14
Temp (°C)
Day of Year
Modeled Temperature
Measured Temperature

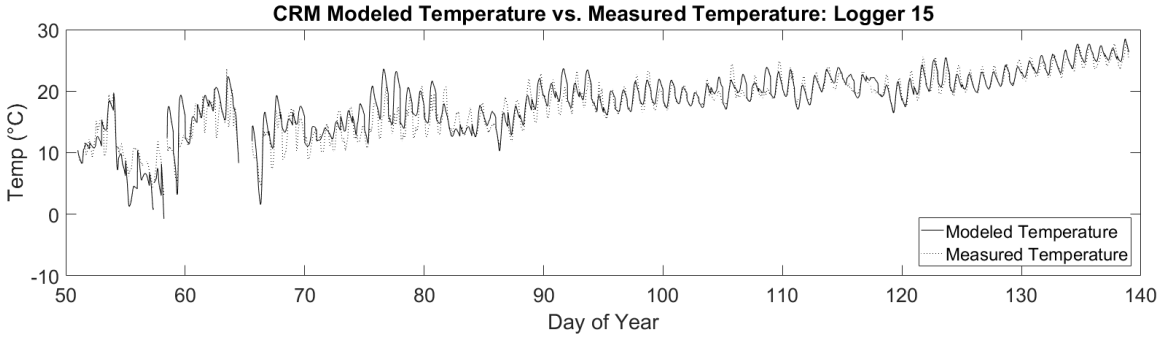
CRM Modeled Temperature vs. Measured Temperature: Logger 15
Temp (°C)
Day of Year
Modeled Temperature
Measured Temperature
30
20
10
0
-10
50
60
70
80
90
100
110
120
130
140

Appendix F: Measured vs. Modeled Shortwave Solar Radiation

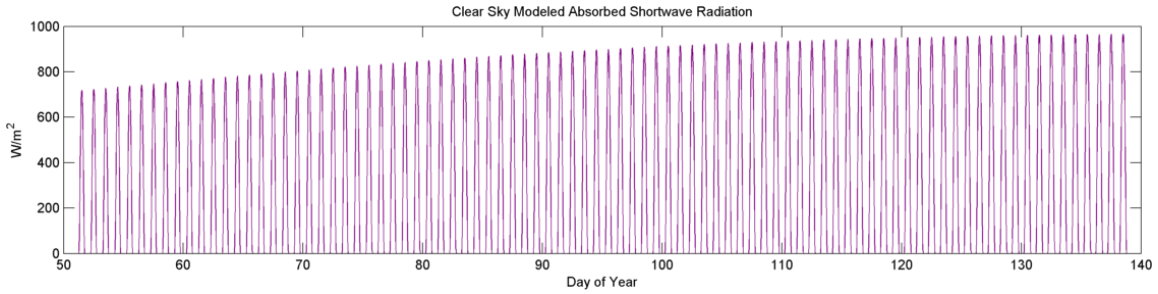

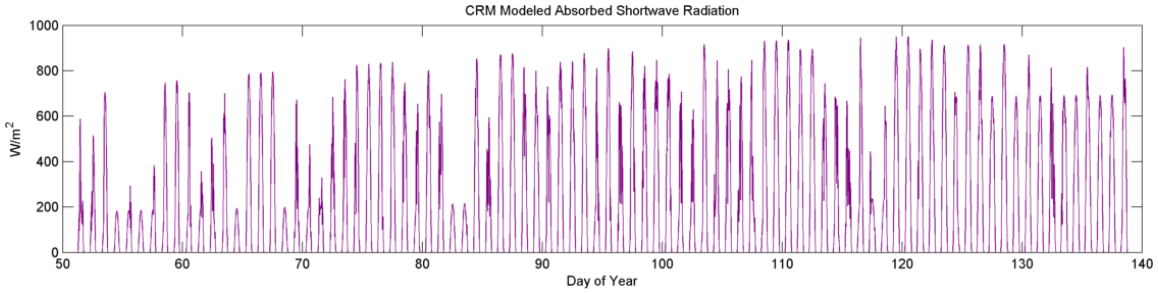

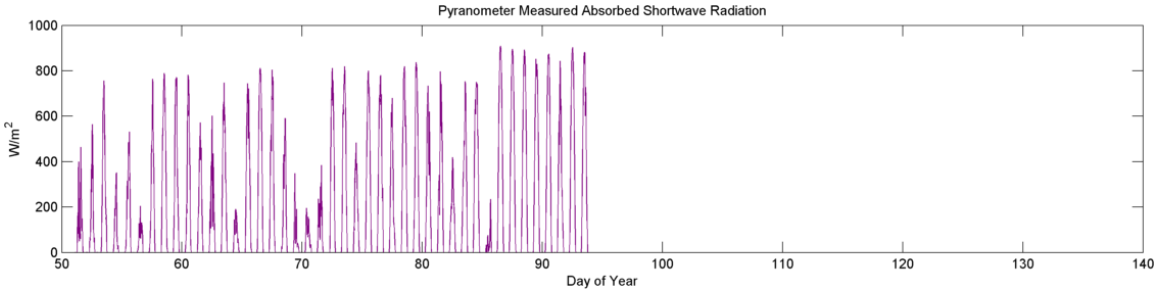

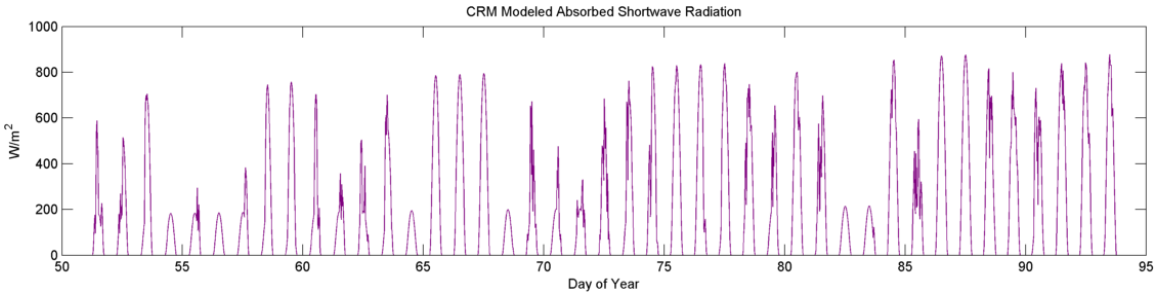

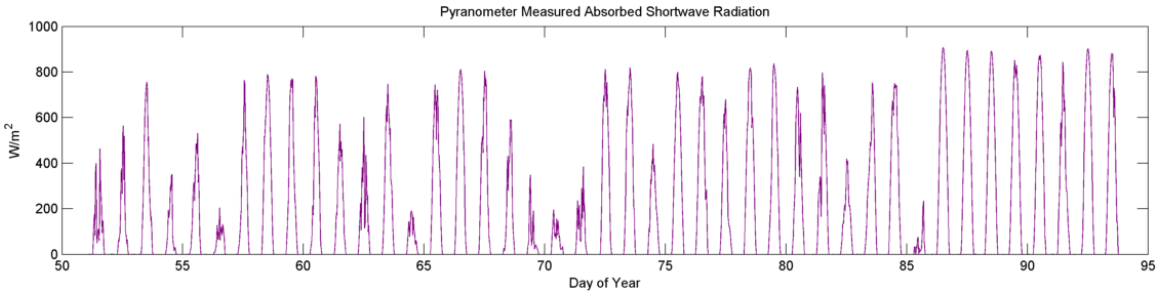
Pyranometer Measured Absorbed Shortwave Radiation
W/m2
Day of Year

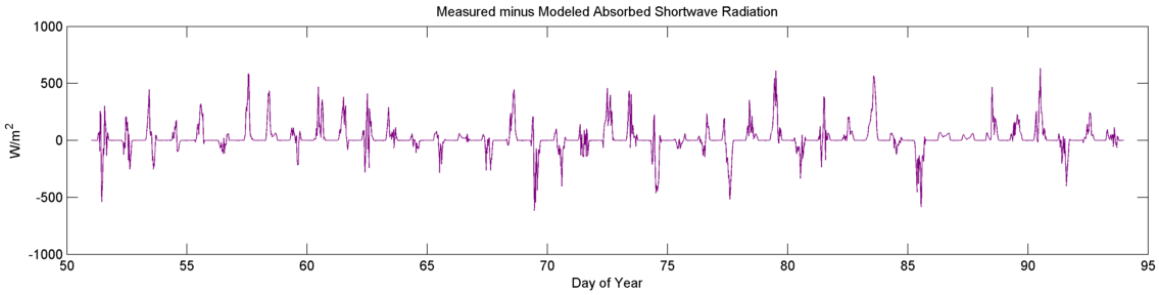
Measured minus Modeled Absorbed Shortwave Radiation
W/m2
Day of Year

Appendix G: Radiation Flux Values

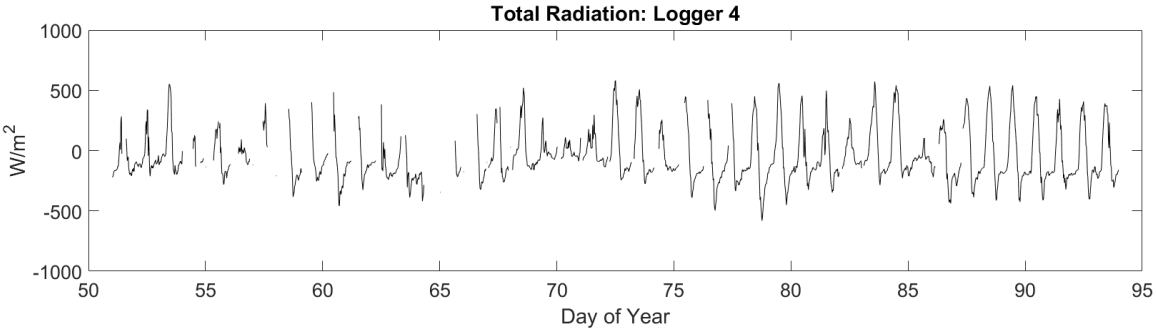

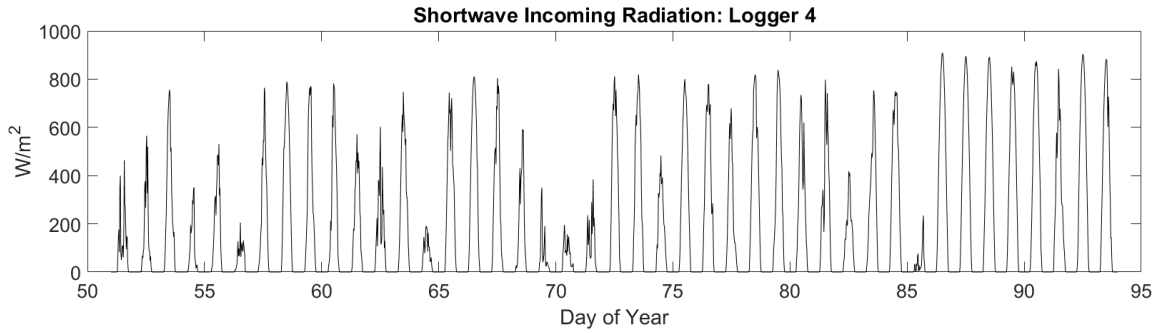

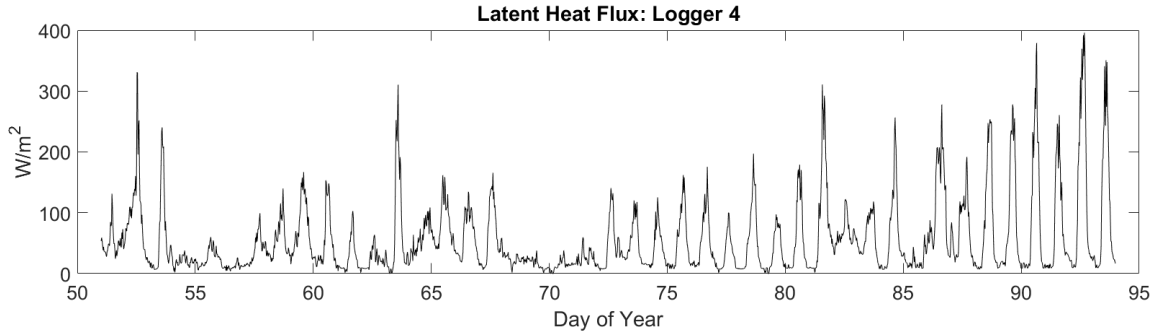

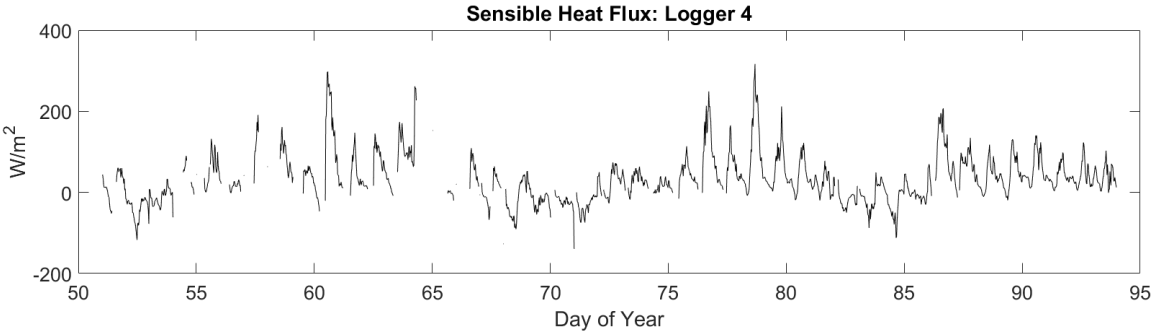

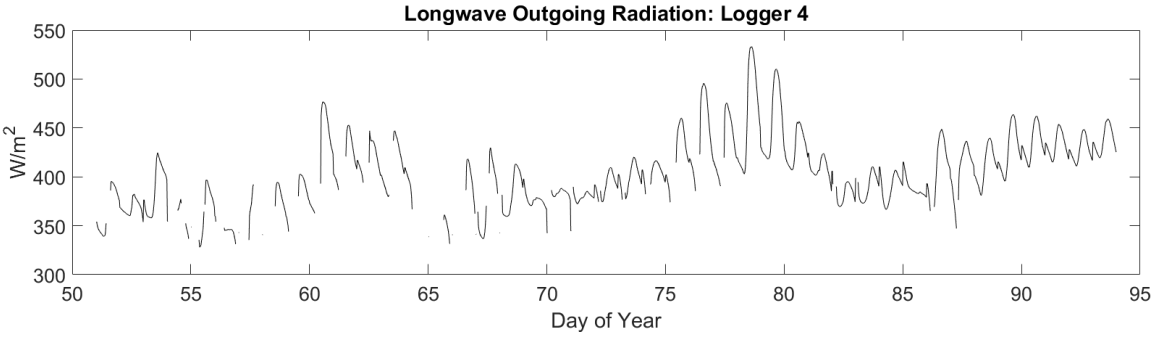
Longwave Outgoing Radiation: Logger 4
W/m2
550
500
450
400
350
300
50
55
60
65
70
75
80
85
90
95
Day of Year

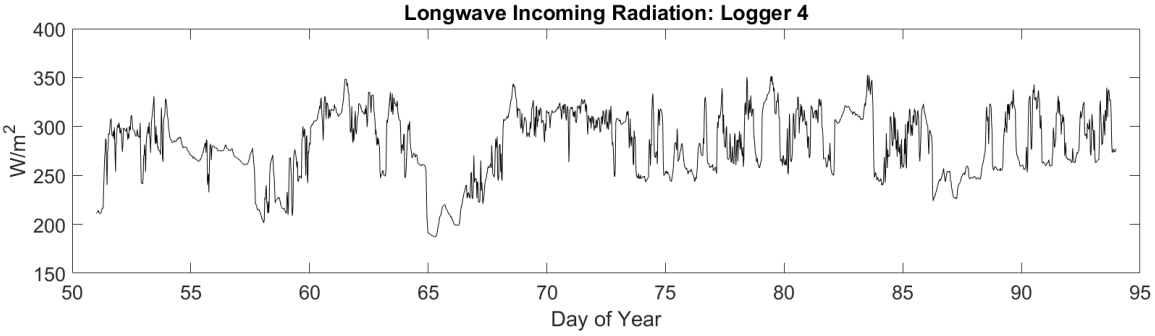
Longwave Incoming Radiation: Logger 4
W/m2
400
350
300
250
200
150
50
55
60
65
70
75
80
85
90
95
Day of Year

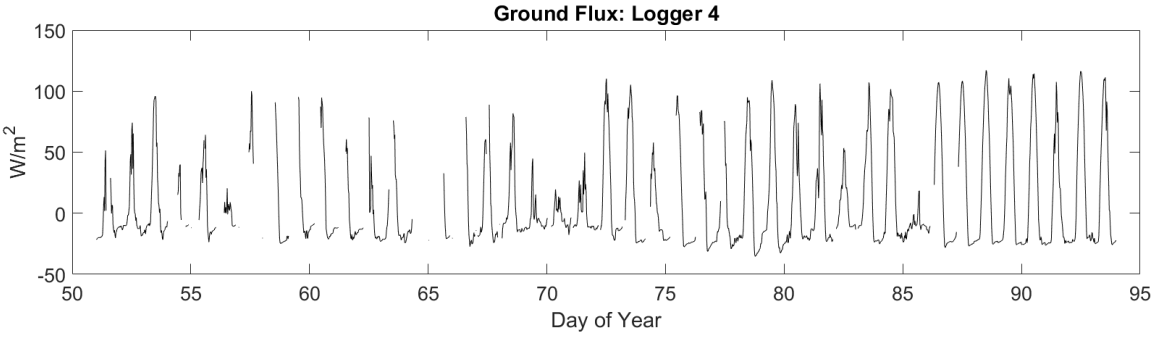
Ground Flux: Logger 4
W/m2
150
100
50
0
-50
50
55
60
65
70
75
80
85
90
95
Day of Year

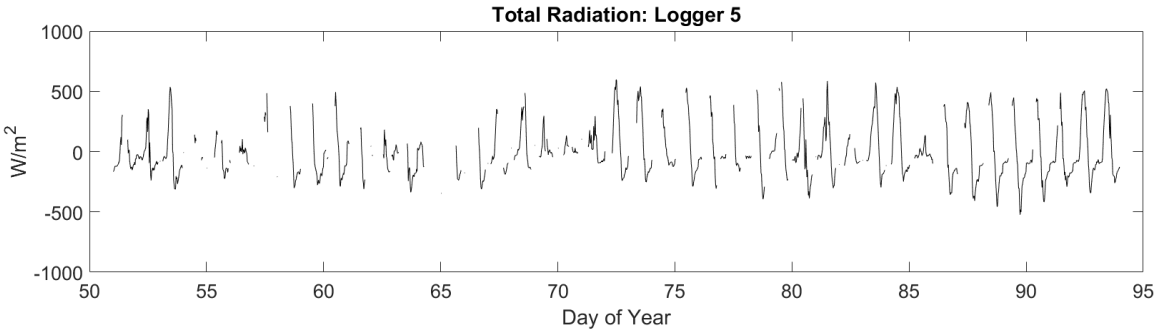
Total Radiation: Logger 5
W/m2
1000
500
0
-500
-1000
50
55
60
65
70
75
80
85
90
95
Day of Year

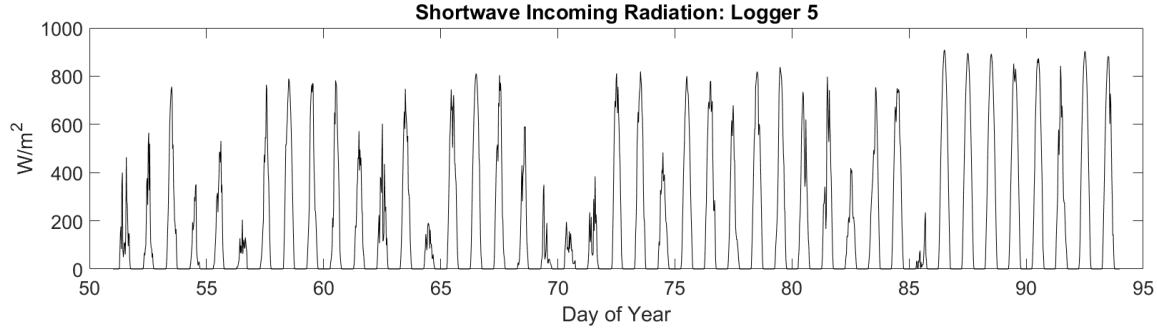
Shortwave Incoming Radiation: Logger 5
W/m2
1000
800
600
400
200
0
50
55
60
65
70
75
80
85
90
95
Day of Year

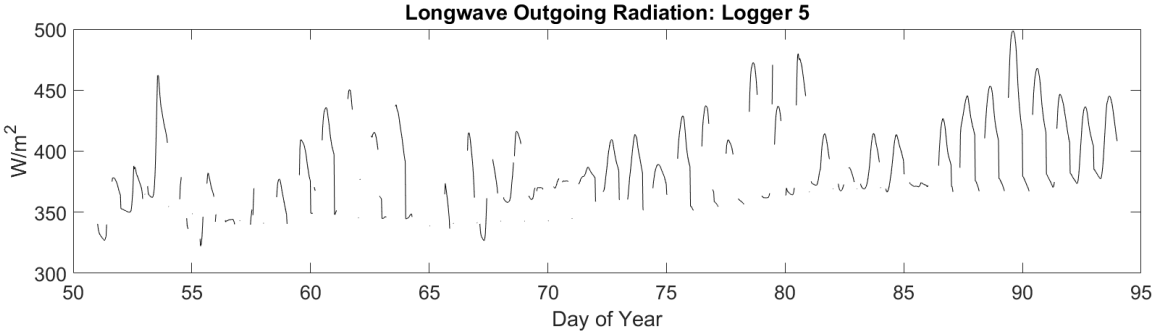
Longwave Outgoing Radiation: Logger 5
W/m2
500
450
400
350
300
50
55
60
65
70
75
80
85
90
95
Day of Year

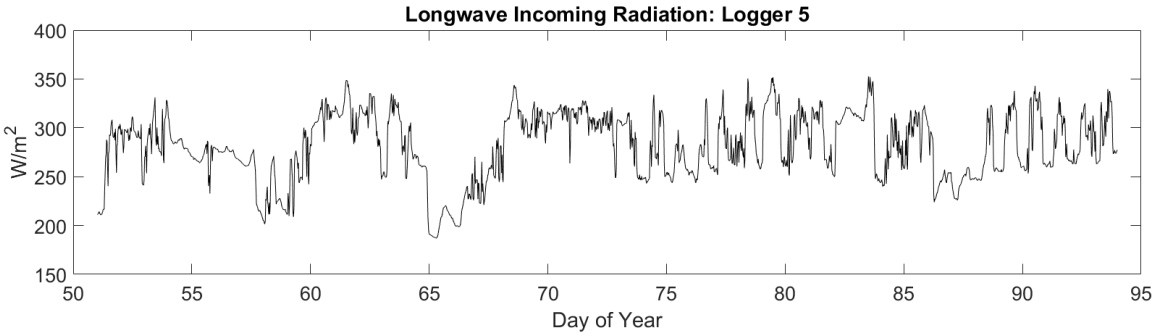
Longwave Incoming Radiation: Logger 5
W/m2
400
350
300
250
200
150
50
55
60
65
70
75
80
85
90
95
Day of Year

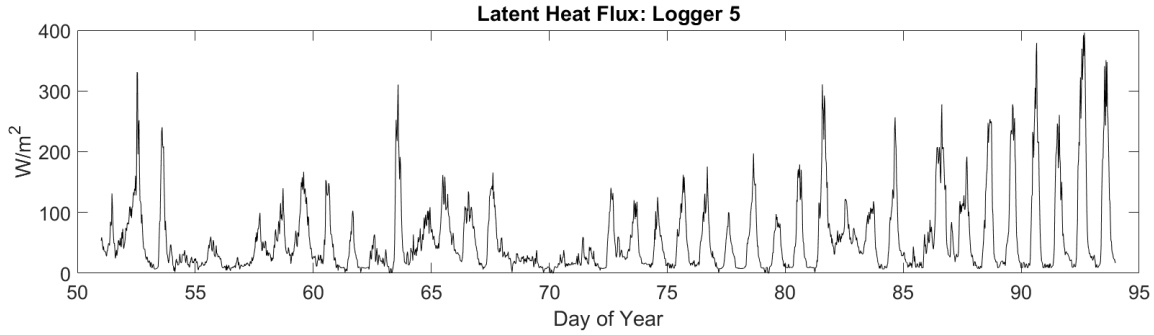
Latent Heat Flux: Logger 5
W/m2
Day of Year

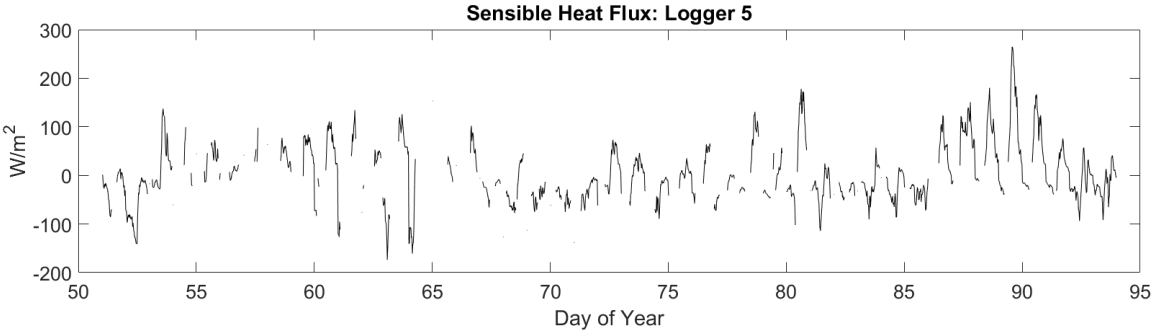
Sensible Heat Flux: Logger 5
W/m2
Day of Year

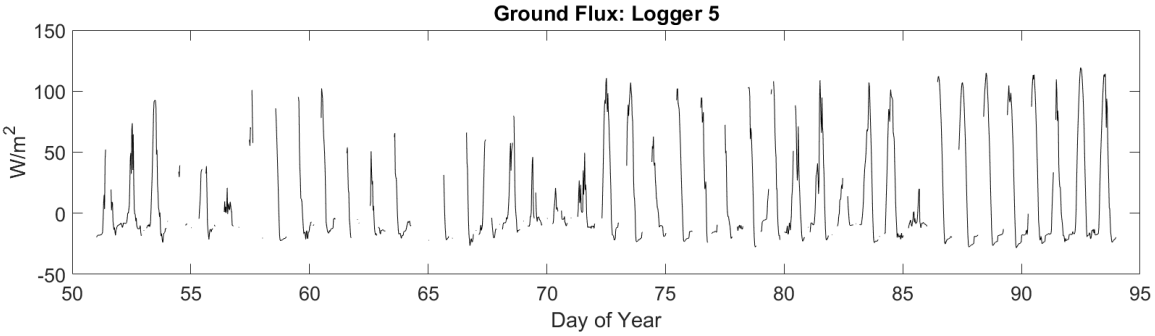
Ground Flux: Logger 5
W/m2
Day of Year

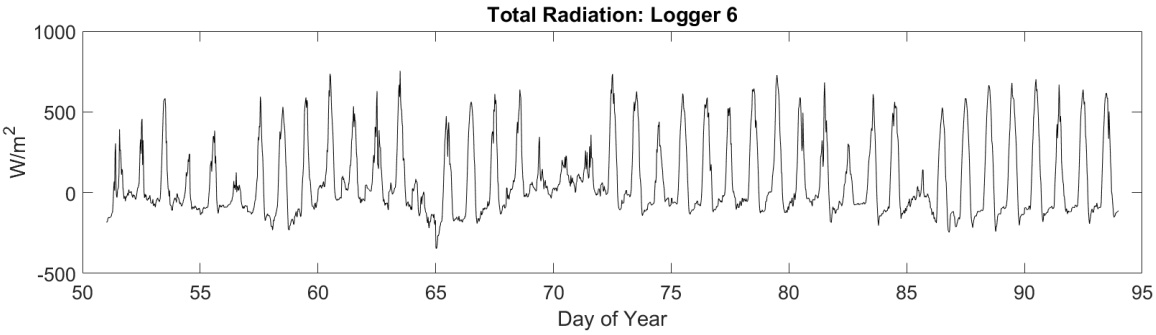
Total Radiation: Logger 6
1000
500
0
-500
W/m2
50
55
60
65
70
75
80
85
90
95
Day of Year

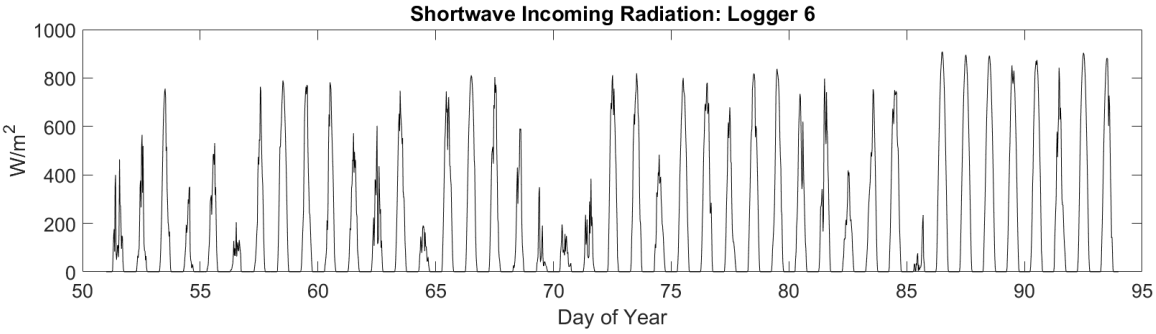
Shortwave Incoming Radiation: Logger 6
1000
800
600
400
200
0
W/m2
50
55
60
65
70
75
80
85
90
95
Day of Year

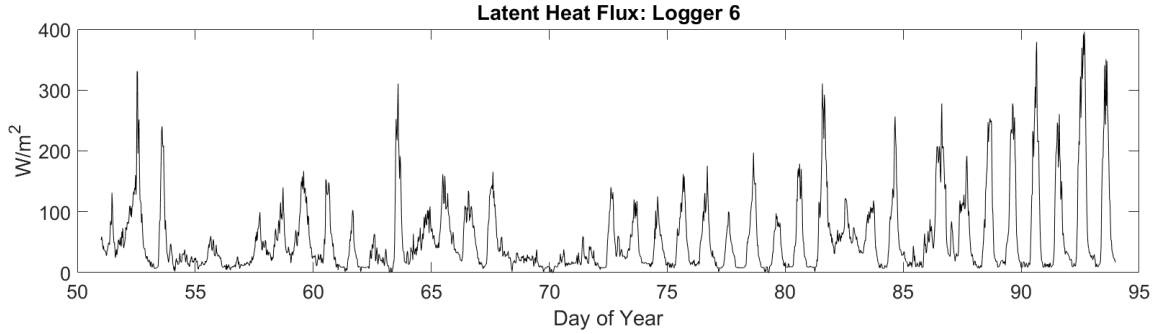
Latent Heat Flux: Logger 6
400
300
200
100
0
W/m2
50
55
60
65
70
75
80
85
90
95
Day of Year

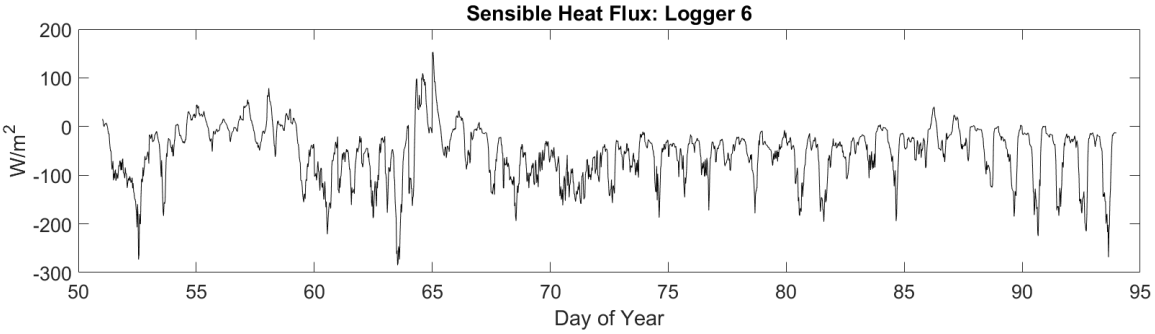
Sensible Heat Flux: Logger 6
200
100
0
-100
-200
-300
W/m2
50
55
60
65
70
75
80
85
90
95
Day of Year

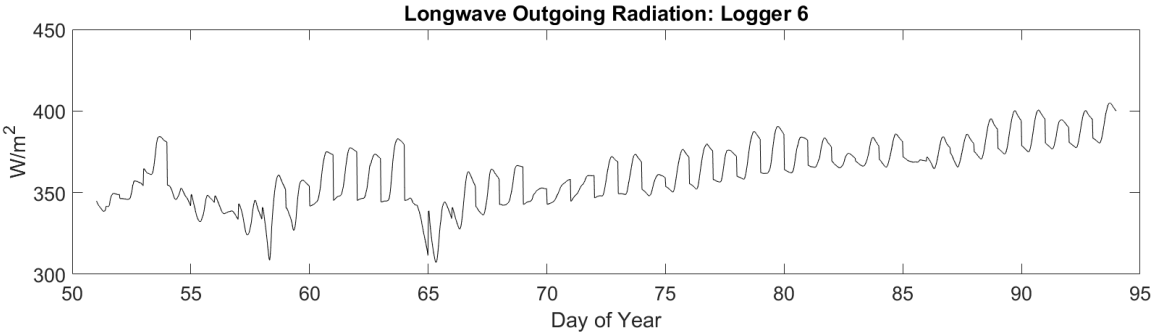
Longwave Outgoing Radiation: Logger 6
W/m2
Day of Year

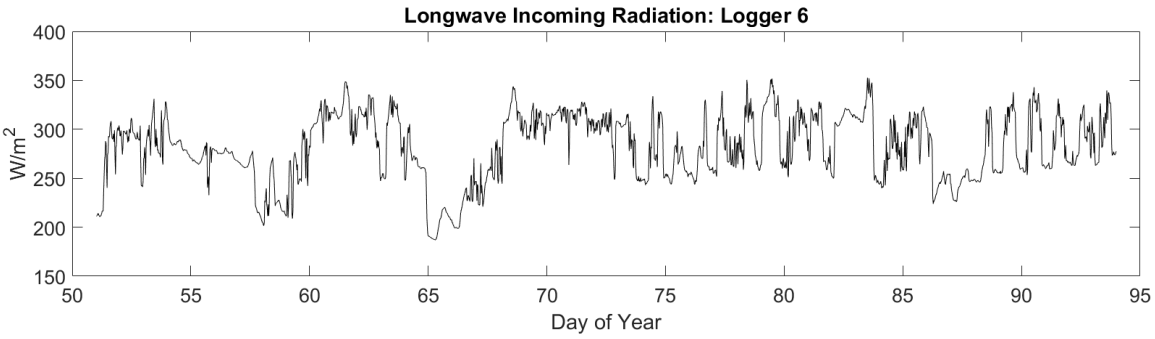
Longwave Incoming Radiation: Logger 6
W/m2
Day of Year

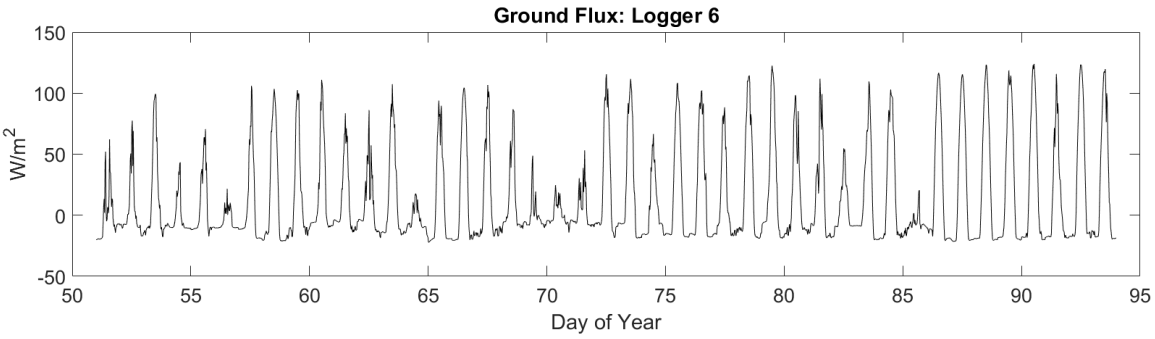
Ground Flux: Logger 6
W/m2
Day of Year

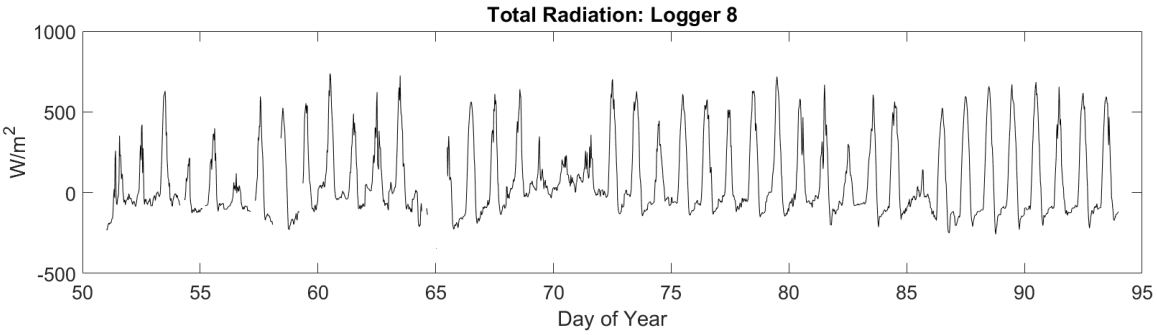
Total Radiation: Logger 8
W/m2
Day of Year

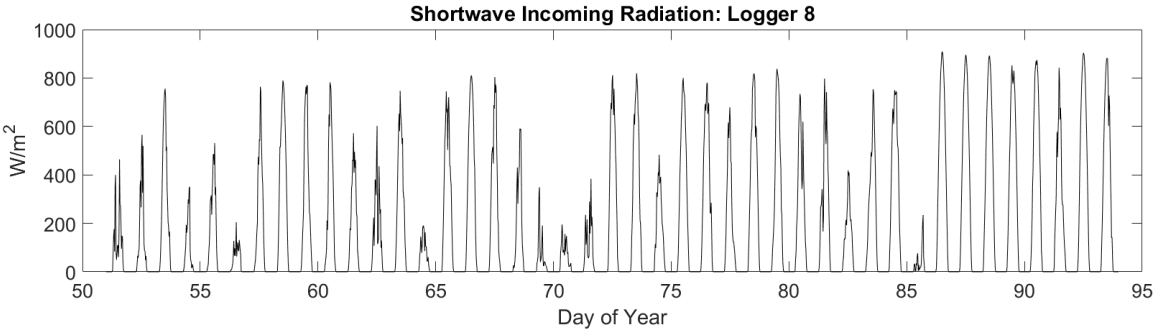
Shortwave Incoming Radiation: Logger 8
W/m2
Day of Year

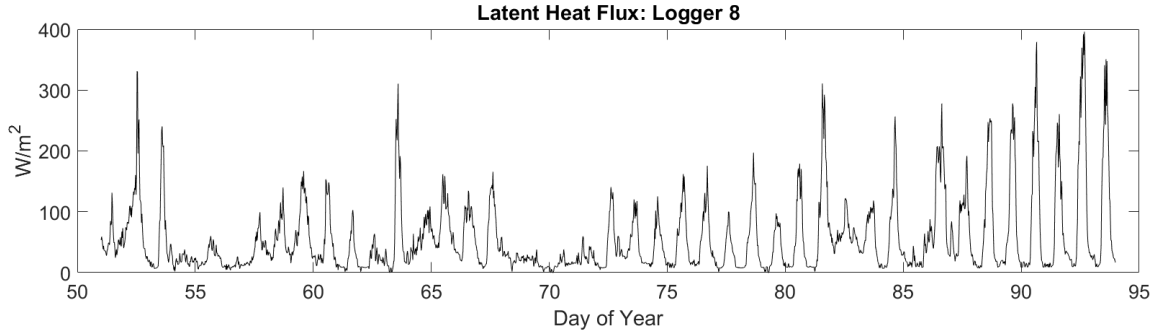
Latent Heat Flux: Logger 8
W/m2
Day of Year

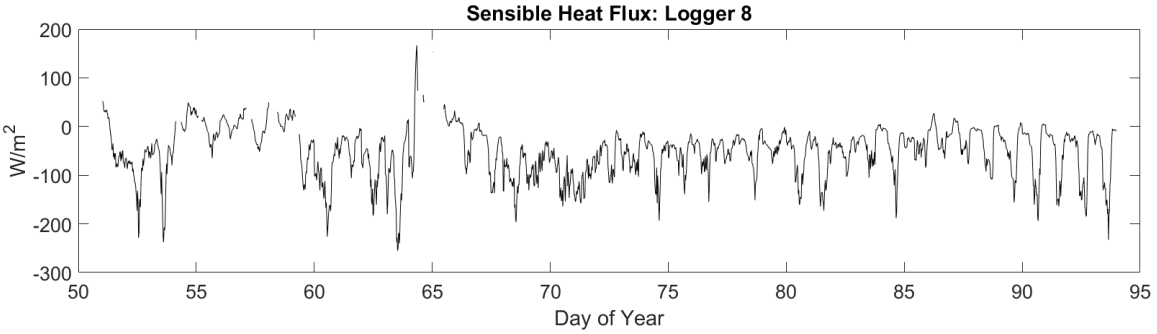
Sensible Heat Flux: Logger 8
W/m2
Day of Year

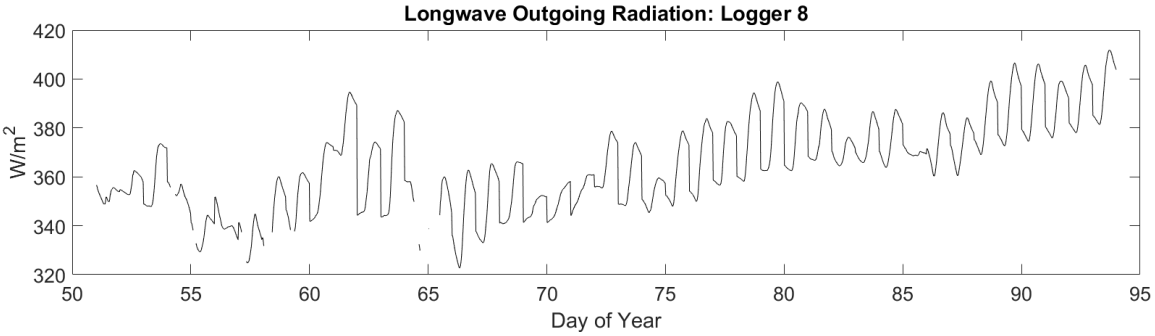
Longwave Outgoing Radiation: Logger 8
W/m2
Day of Year

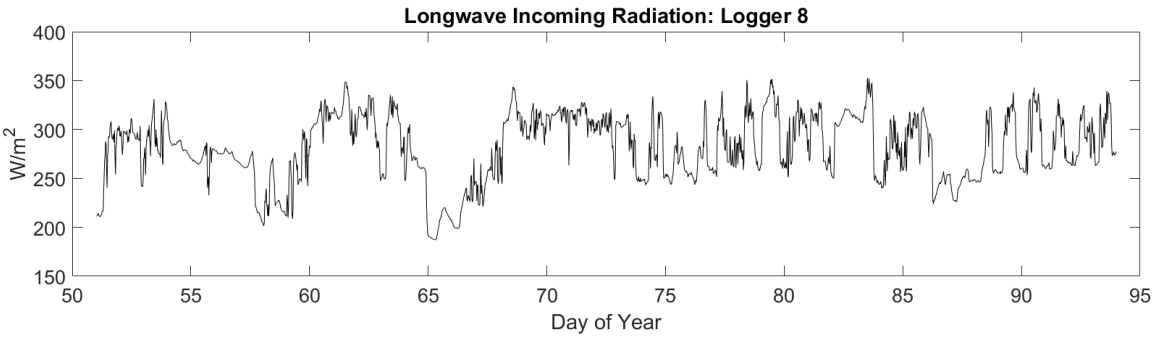
Longwave Incoming Radiation: Logger 8
W/m2
Day of Year

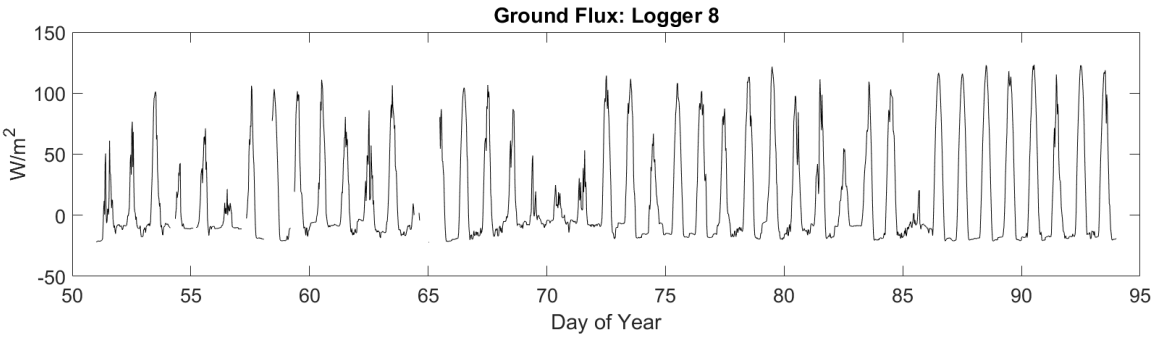
Ground Flux: Logger 8
W/m2
Day of Year

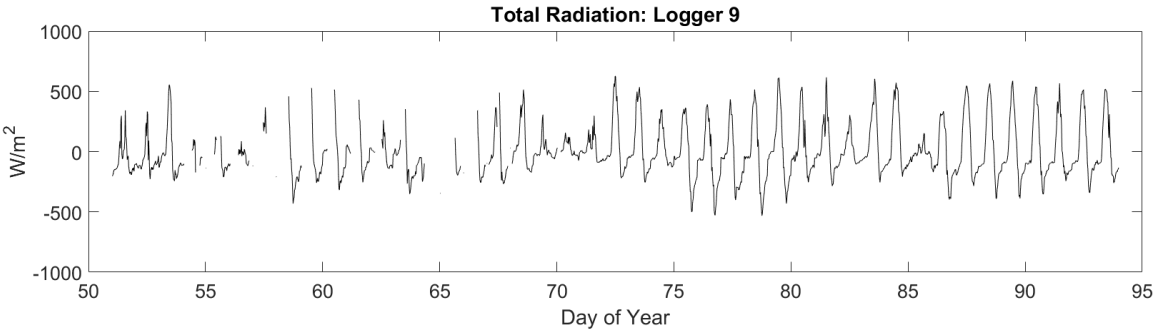
Total Radiation: Logger 9
W/m2
1000
500
0
-500
-1000
50
55
60
65
70
75
80
85
90
95
Day of Year

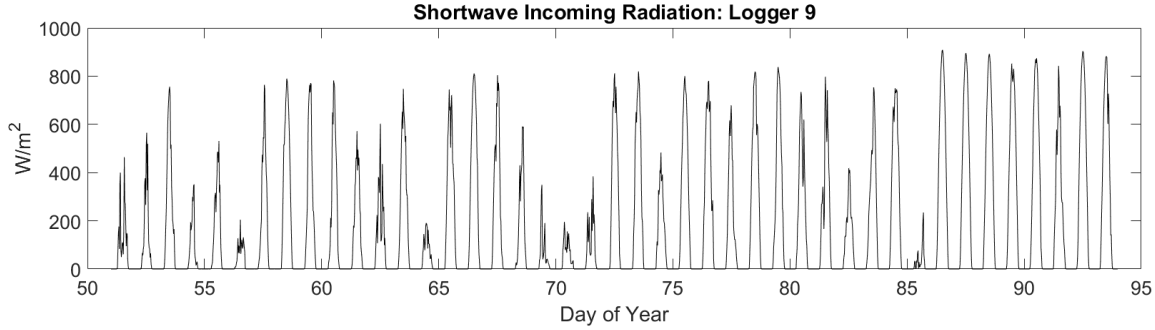
Shortwave Incoming Radiation: Logger 9
W/m2
1000
800
600
400
200
0
50
55
60
65
70
75
80
85
90
95
Day of Year

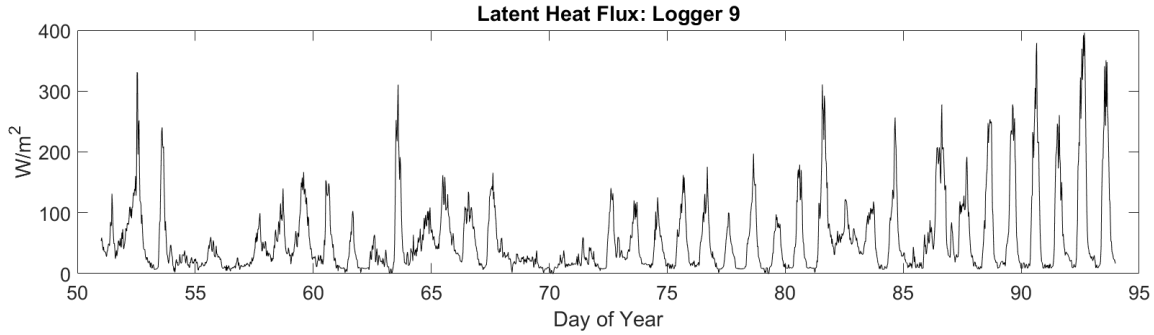
Latent Heat Flux: Logger 9
W/m2
400
300
200
100
0
50
55
60
65
70
75
80
85
90
95
Day of Year

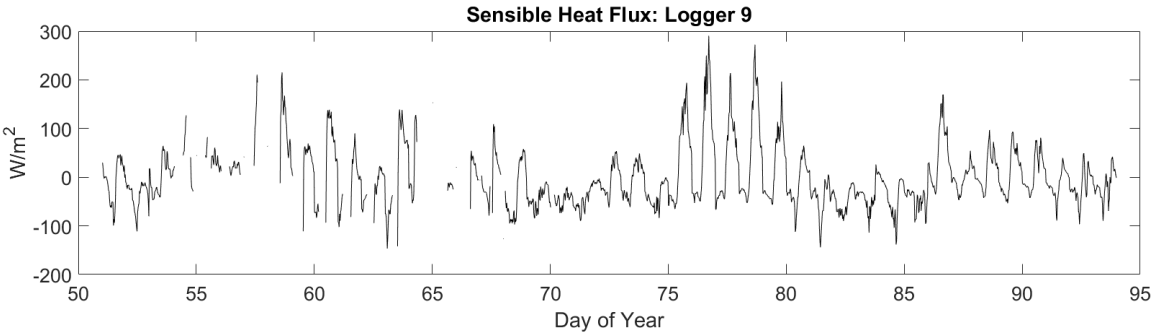
Sensible Heat Flux: Logger 9
W/m2
300
200
100
0
-100
-200
50
55
60
65
70
75
80
85
90
95
Day of Year

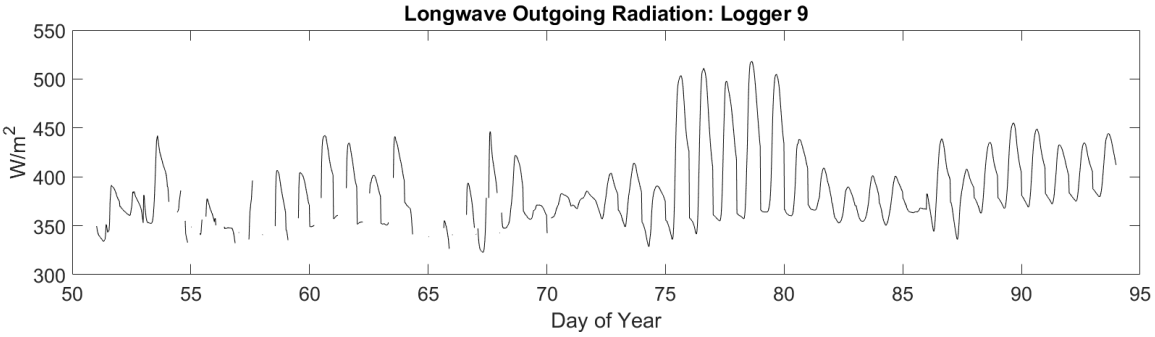
Longwave Outgoing Radiation: Logger 9
W/m2
Day of Year

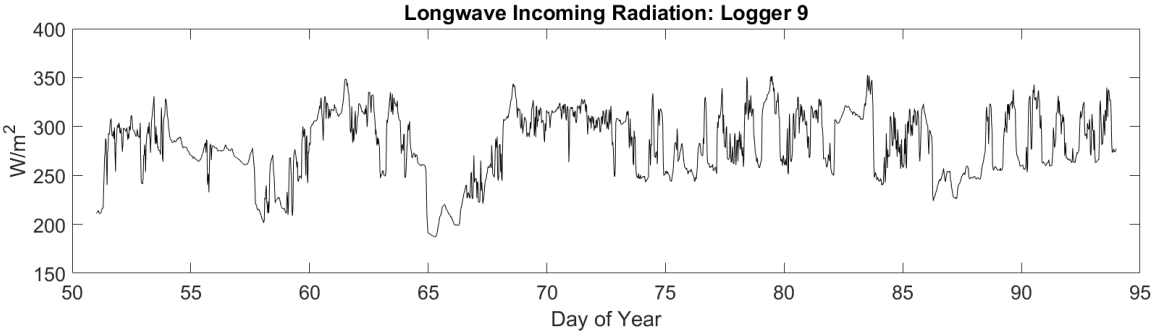
Longwave Incoming Radiation: Logger 9
W/m2
Day of Year

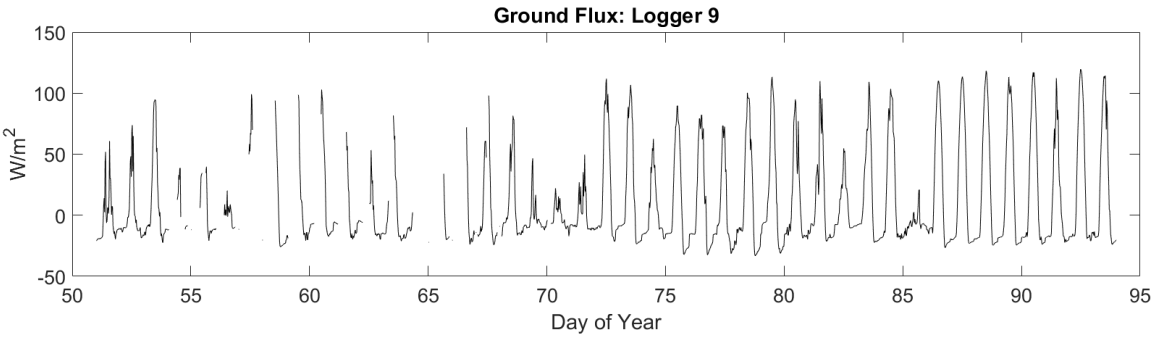
Ground Flux: Logger 9
W/m2
Day of Year

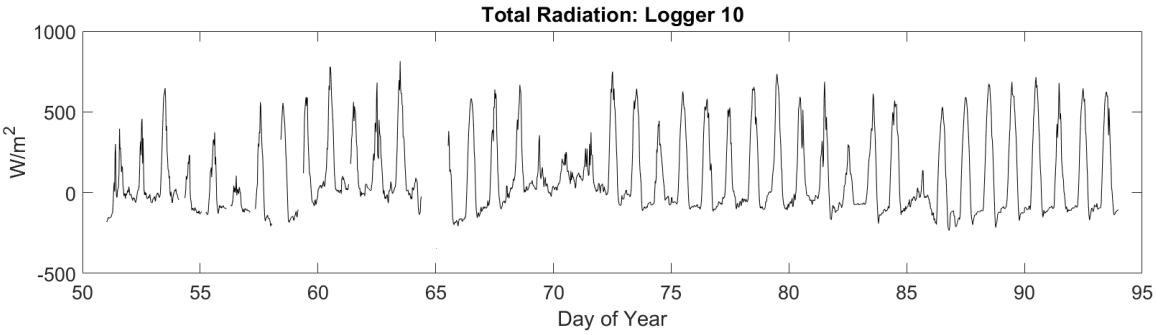
Total Radiation: Logger 10
W/m2
Day of Year

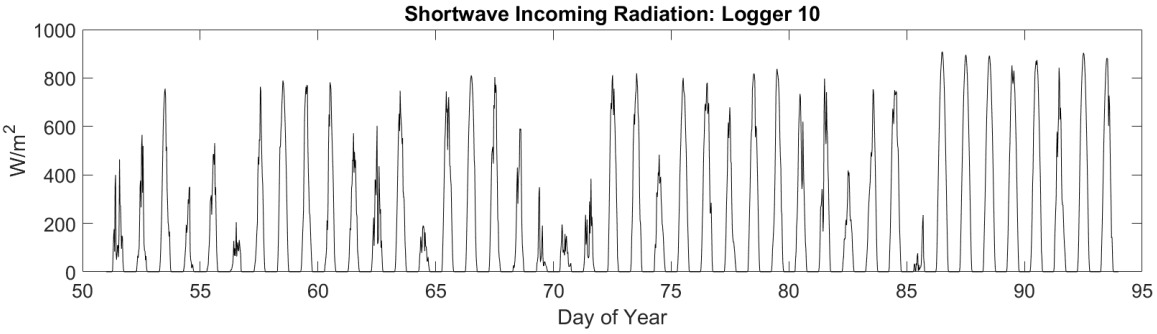
Shortwave Incoming Radiation: Logger 10
W/m2
Day of Year

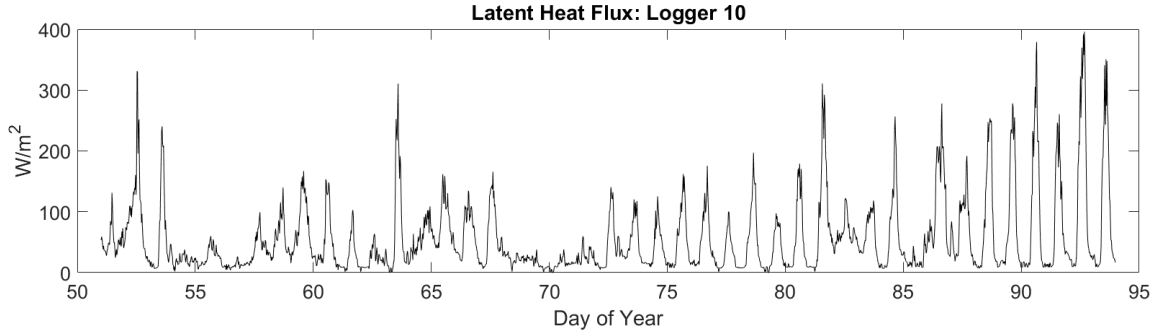
Latent Heat Flux: Logger 10
W/m2
Day of Year

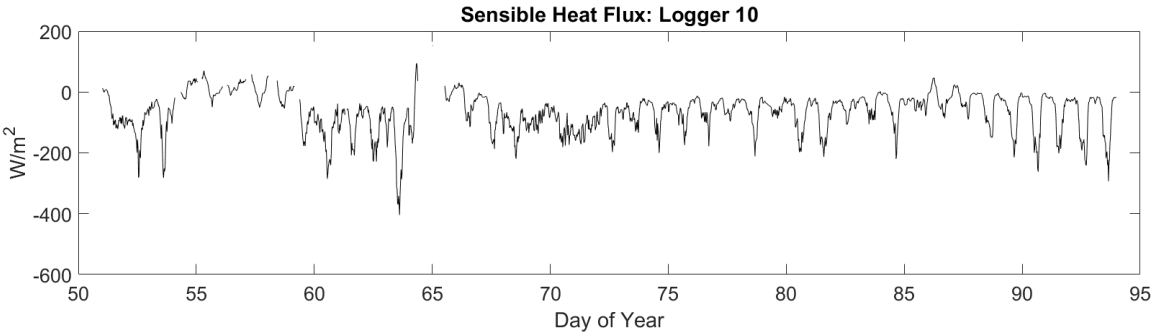
Sensible Heat Flux: Logger 10
W/m2
Day of Year

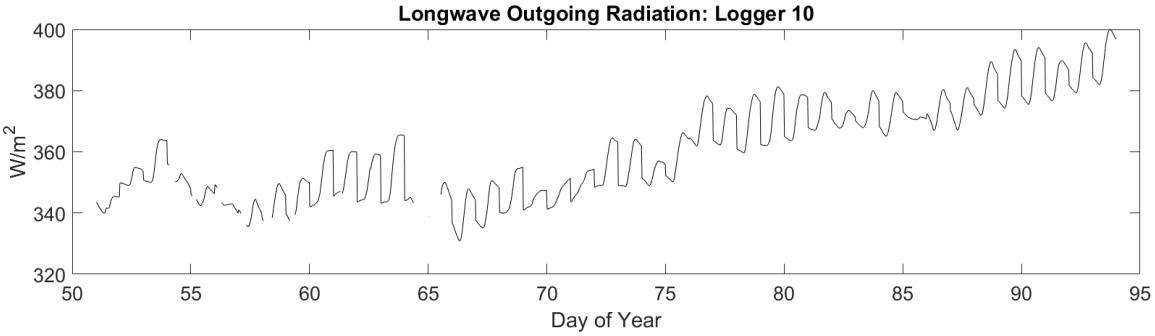
Longwave Outgoing Radiation: Logger 10
W/m2
Day of Year

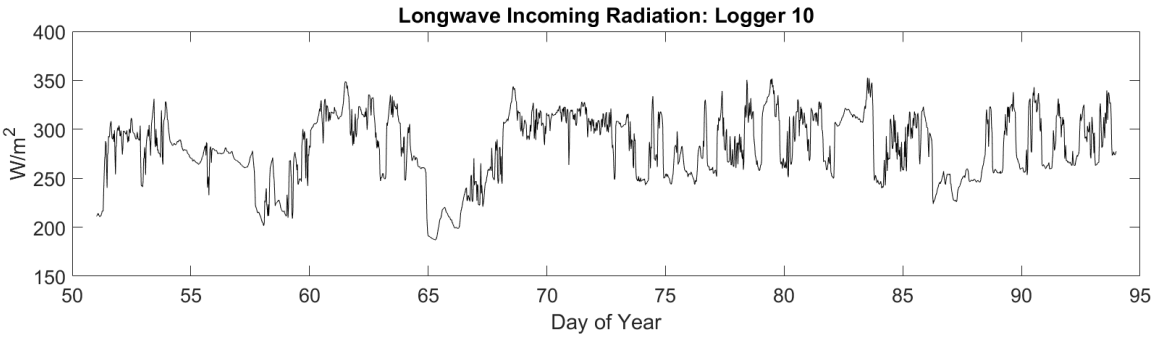
Longwave Incoming Radiation: Logger 10
W/m2
Day of Year

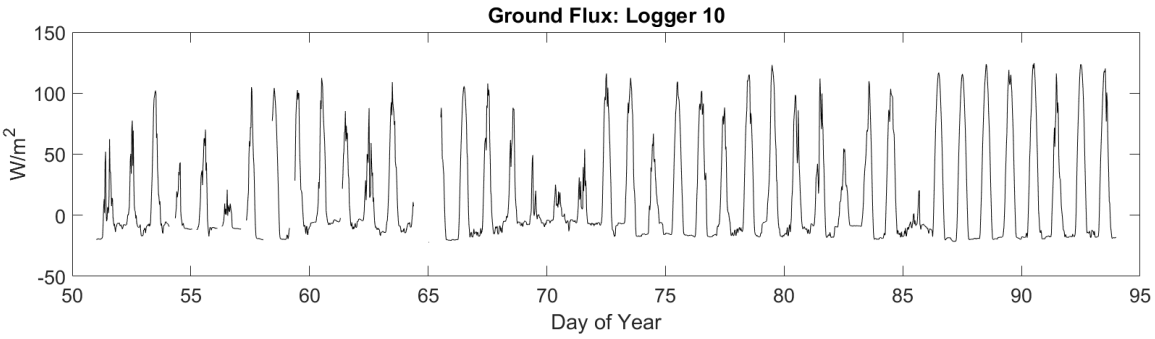
Ground Flux: Logger 10
W/m2
Day of Year

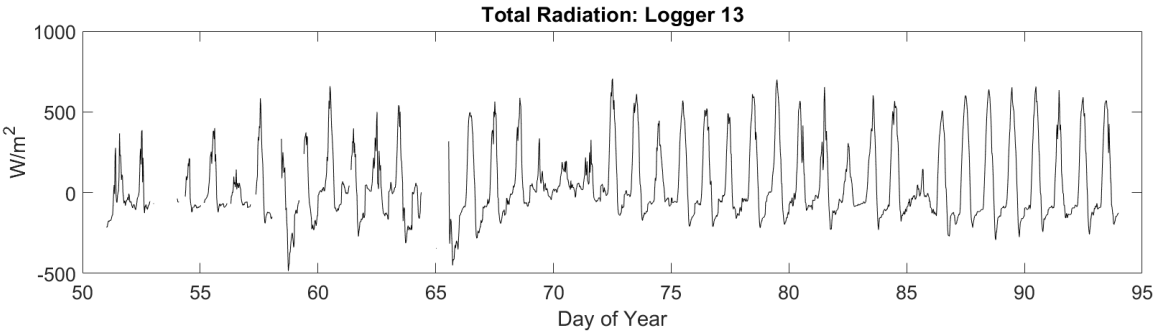
Total Radiation: Logger 13
W/m2
Day of Year

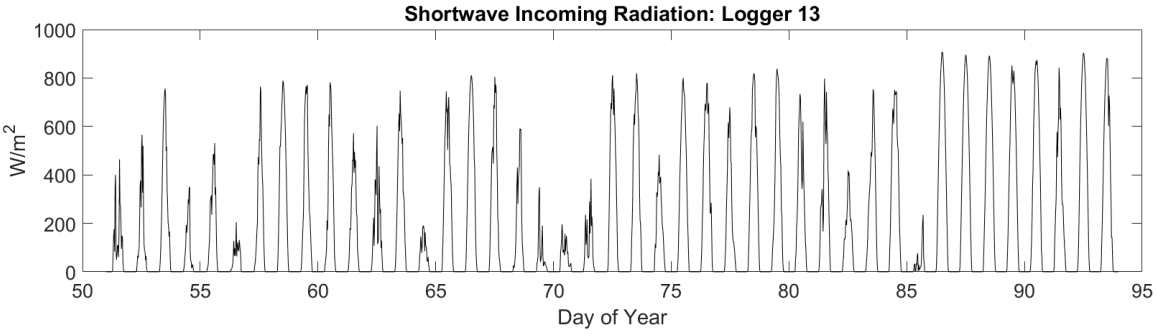
Shortwave Incoming Radiation: Logger 13
W/m2
Day of Year

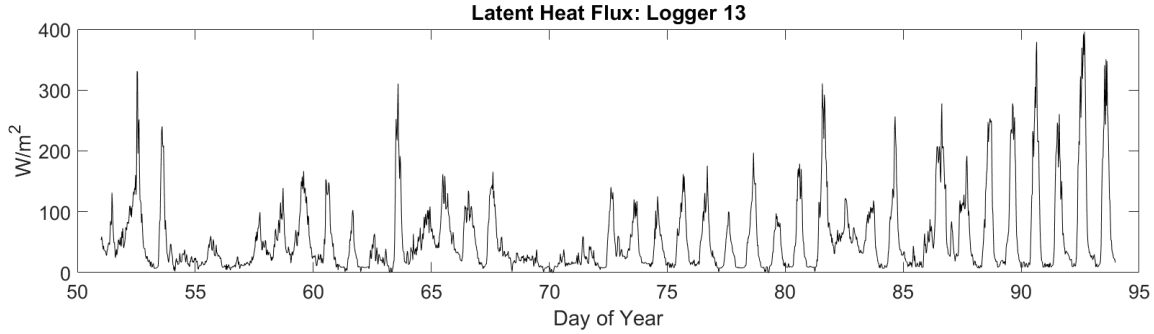
Latent Heat Flux: Logger 13
W/m2
Day of Year

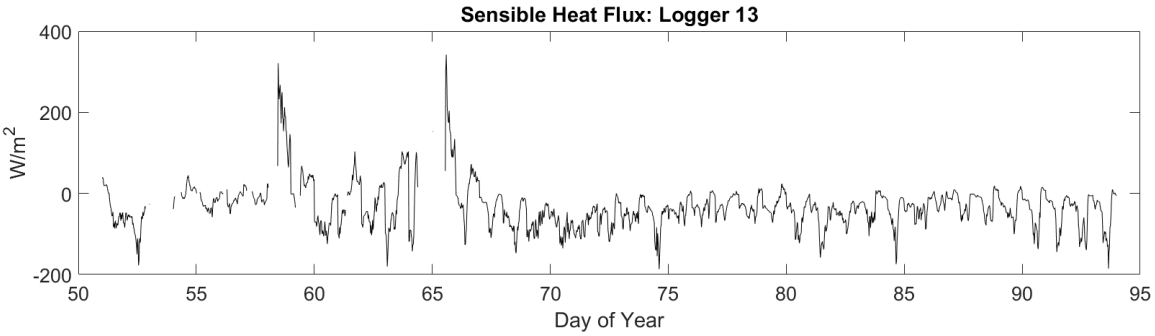
Sensible Heat Flux: Logger 13
W/m2
Day of Year

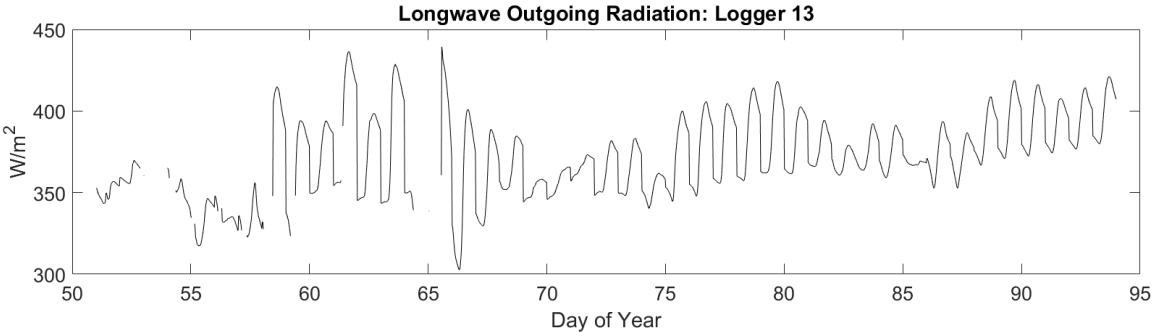
Longwave Outgoing Radiation: Logger 13
W/m2
Day of Year

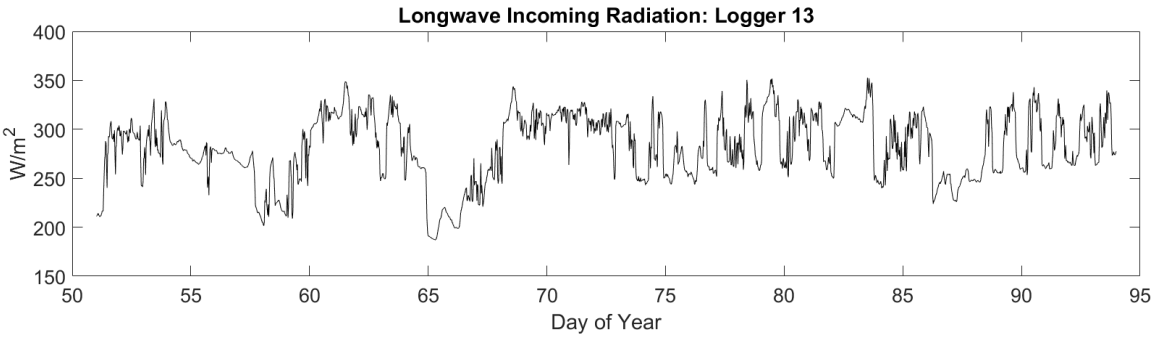
Longwave Incoming Radiation: Logger 13
W/m2
Day of Year

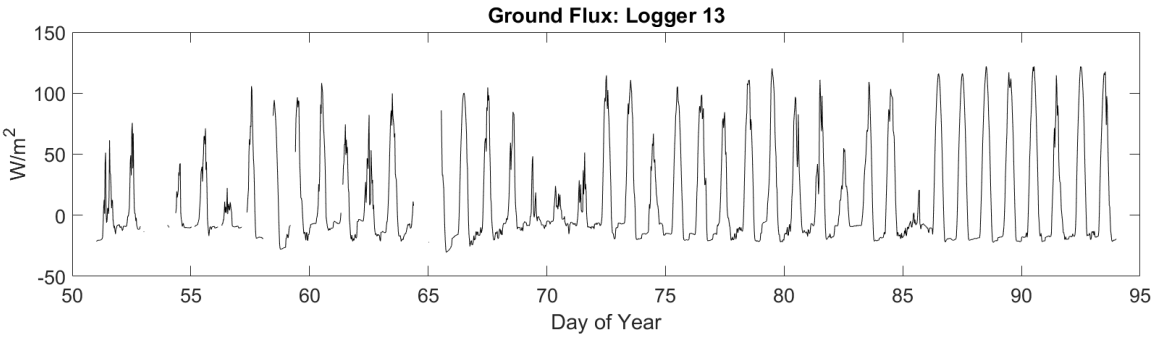
Ground Flux: Logger 13
W/m2
Day of Year

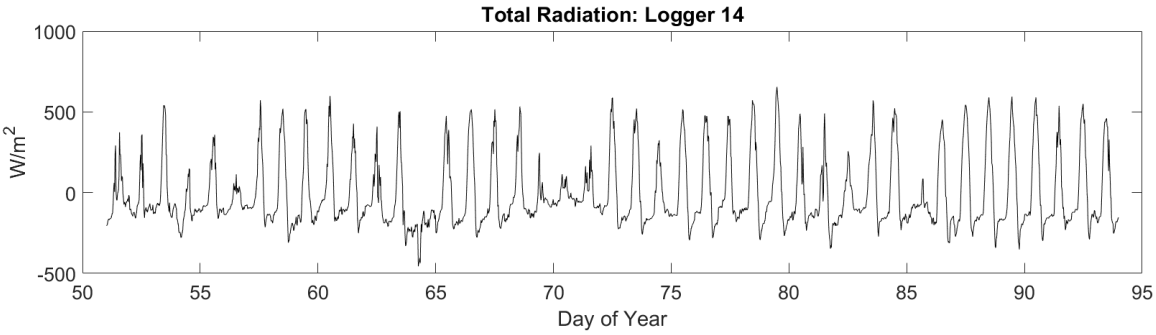
Total Radiation: Logger 14
W/m2
Day of Year

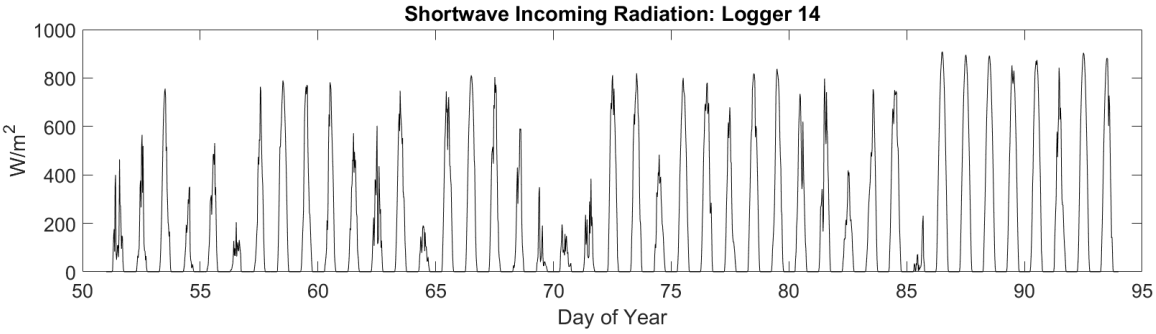
Shortwave Incoming Radiation: Logger 14
W/m2
Day of Year

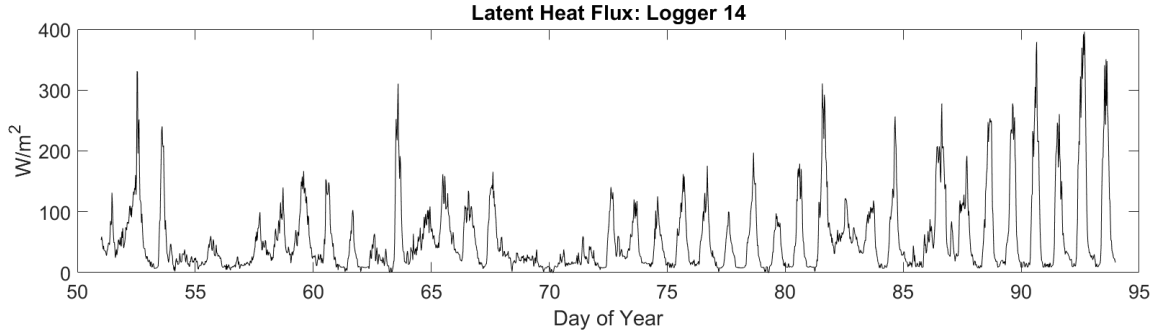
Latent Heat Flux: Logger 14
W/m2
Day of Year

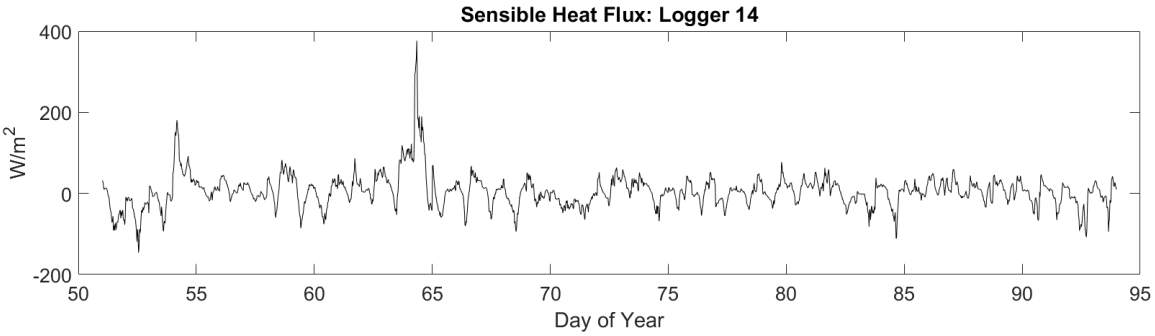
Sensible Heat Flux: Logger 14
W/m2
Day of Year

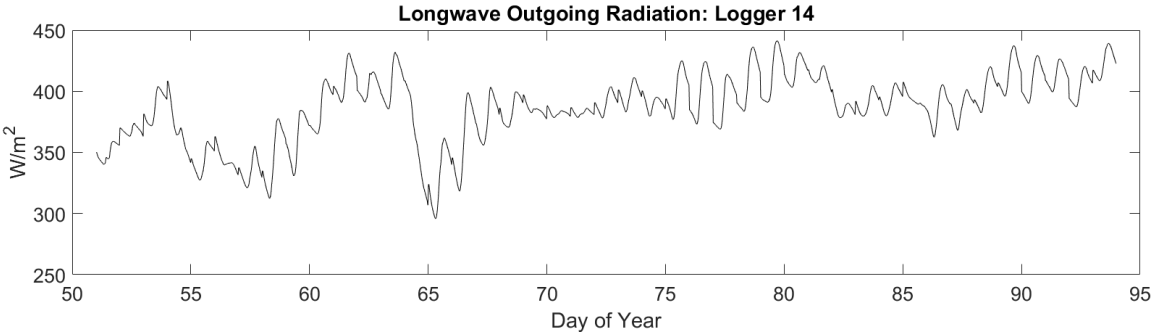
Longwave Outgoing Radiation: Logger 14
W/m2
Day of Year

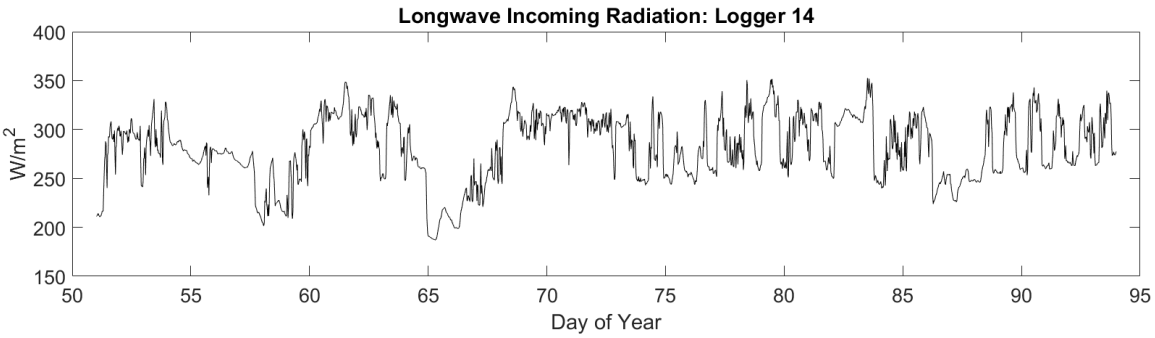
Longwave Incoming Radiation: Logger 14
W/m2
Day of Year

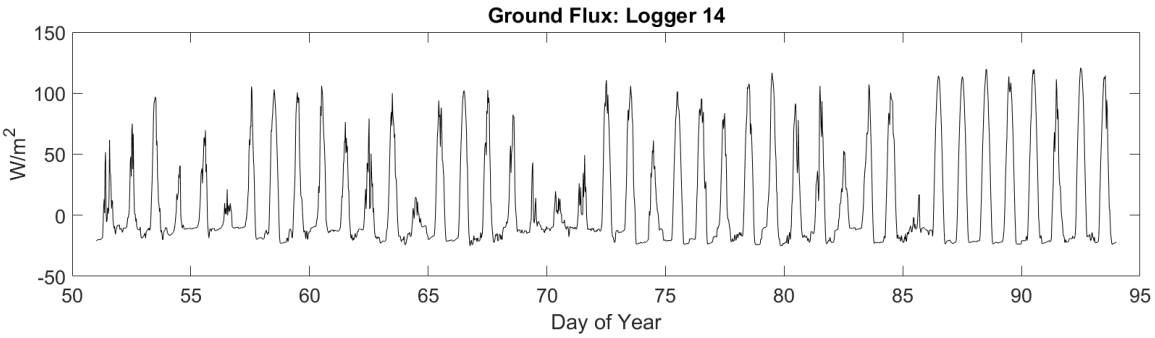
Ground Flux: Logger 14
W/m2
Day of Year

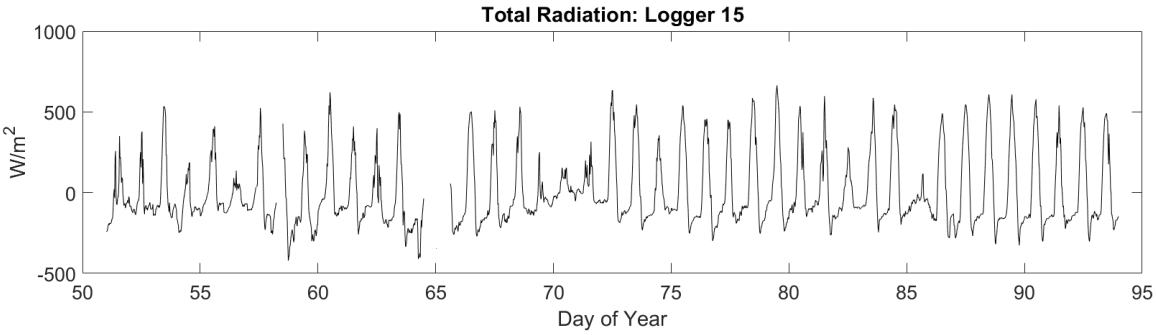
Total Radiation: Logger 15
W/m2
Day of Year

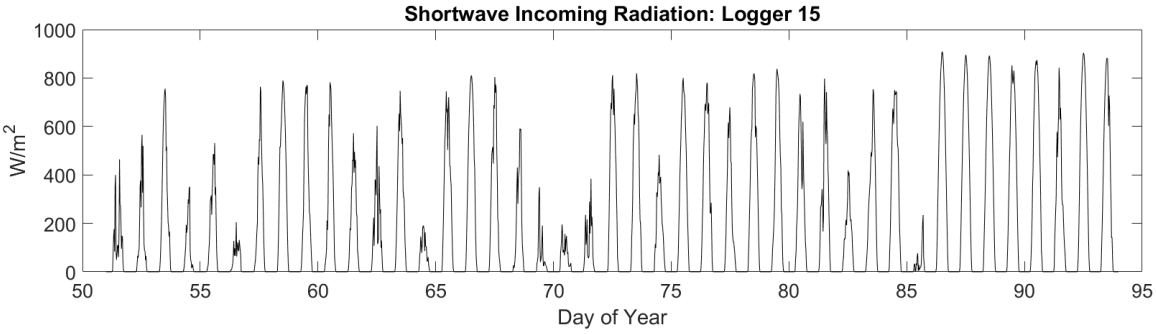
Shortwave Incoming Radiation: Logger 15
W/m2
Day of Year

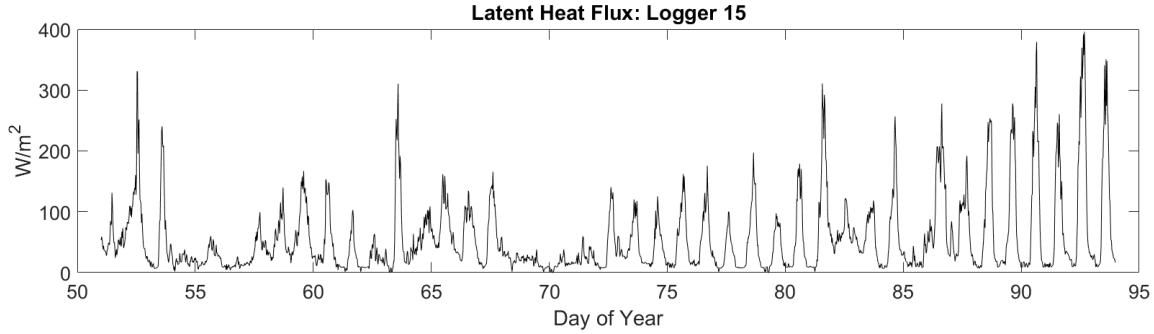
Latent Heat Flux: Logger 15
W/m2
Day of Year

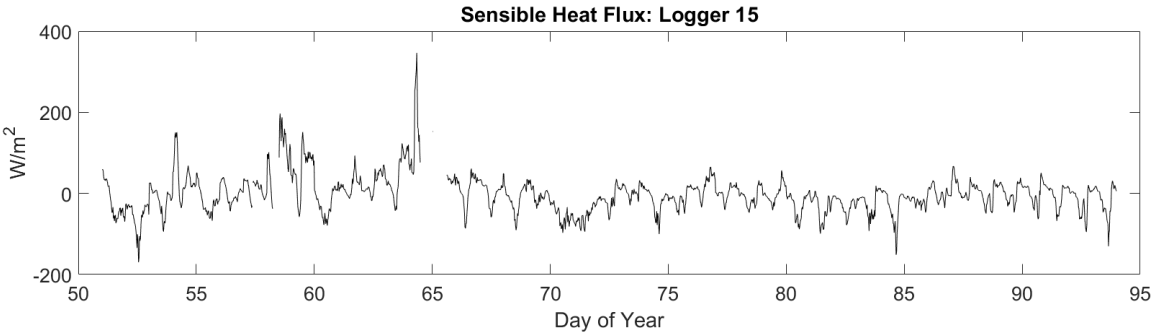
Sensible Heat Flux: Logger 15
W/m2
Day of Year

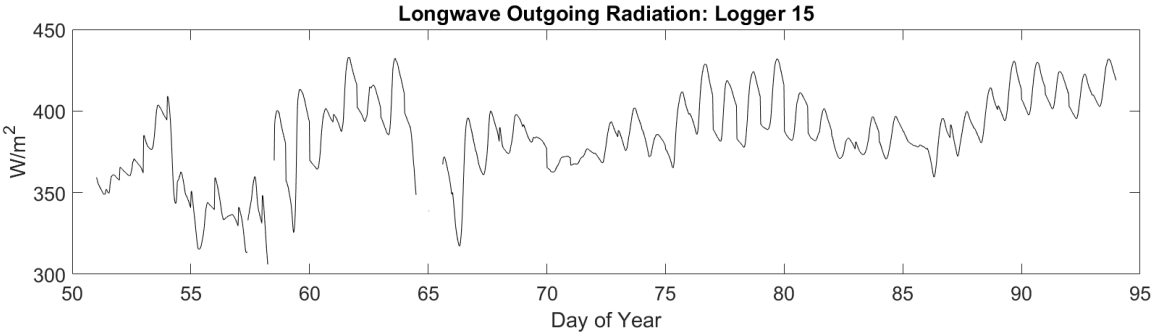
Longwave Outgoing Radiation: Logger 15
W/m2
Day of Year

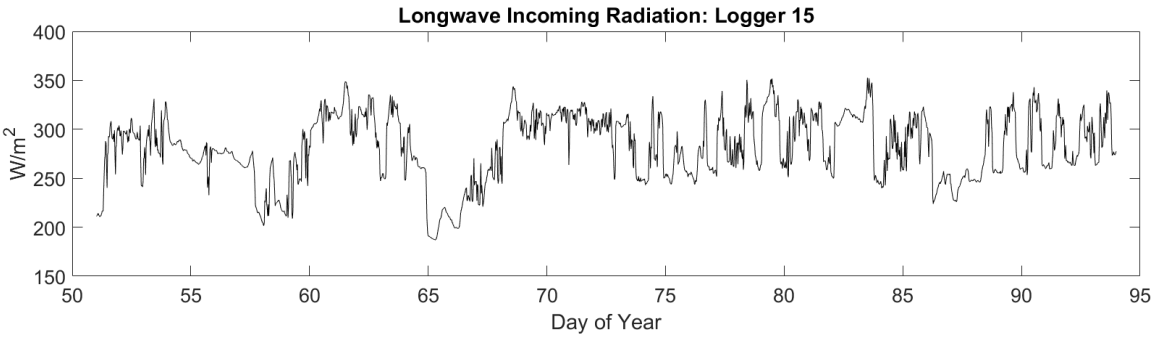
Longwave Incoming Radiation: Logger 15
W/m2
Day of Year

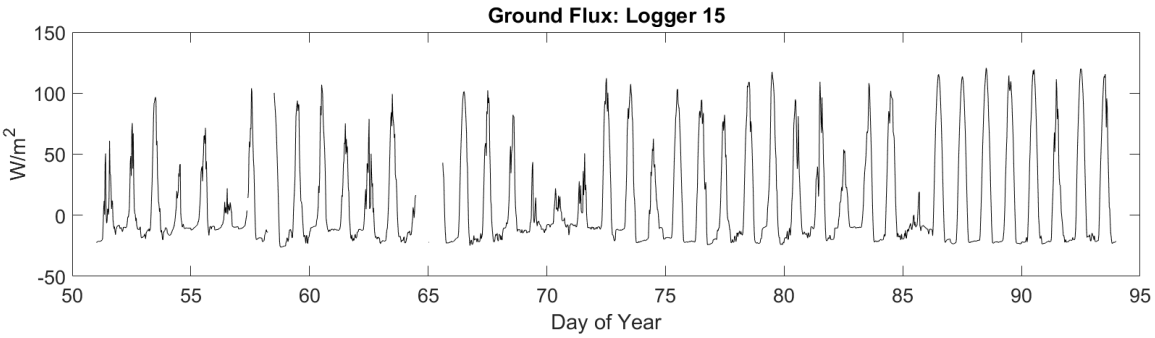
Ground Flux: Logger 15
W/m2
Day of Year

Appendix H: Anomaly between Measured and Modeled Water Temperature

Logger	Mean Anomaly (°C)
10	1.00
14	1.28
8	2.03
15	2.39
6	2.50
4	3.61
13	4.24
9	6.51
5	7.01

Table H.1: Mean Positive Anomaly, Pyranometer (43 Days)

Logger	Mean Anomaly (°C)
10	0.93
14	1.45
8	1.94
6	2.27
15	2.35
4	3.15
13	3.83
9	6.18
5	6.56

Table H.2: Mean Positive Anomaly, CRM (43 Days)

Logger	Mean Anomaly (°C)
8	-0.86
10	-0.95
6	-1.09
5	-1.14
13	-1.22
15	-1.29
14	-1.66
4	-1.85
9	-1.91

Table H.3: Mean Negative Anomaly, Pyranometer (43 Days)

Logger	Mean Anomaly (°C)
8	-1.00
10	-1.07
6	-1.20
5	-1.35
13	-1.37
15	-1.62
9	-1.93
14	-2.13
4	-2.14

Table H.4: Mean Negative Anomaly, CRM (43 Days)

Logger	Mean Anomaly (°C)
14	-0.56
10	-0.25
4	0.45
8	0.71
15	1.01
6	1.01
13	1.90
9	3.27
5	4.83
Mean of All Loggers	**1.37**

Table H.5: Mean Total Anomaly, Pyranometer (43 Days)

Logger	Mean Anomaly (°C)
14	-0.88
10	-0.36
4	-0.07
8	0.51
15	0.71
6	0.78
13	1.57
9	2.90
5	4.56
Mean of All Loggers	**1.08**

Table H.6: Mean Total Anomaly, CRM (43 Days)

Logger	Mean Anomaly (°C)
10	0.83
14	1.16
15	1.59
8	1.61
6	1.86
4	2.24
13	3.43
9	3.91
5	4.43

Table H.7: Mean Positive Anomaly, CRM (88 Days)

Logger	Mean Anomaly (°C)
6	-0.76
8	-0.82
10	-0.85
5	-0.97
15	-1.14
13	-1.17
9	-1.20
4	-1.54
14	-1.62

Table H.8: Mean Negative Anomaly, CRM (88 Days)

Logger	Mean Anomaly (°C)
14	-0.25
10	-0.24
8	0.28
4	0.31
15	0.50
6	0.80
13	1.26
9	1.54
5	2.39
Mean of All Loggers	**0.73**

Table H.9: Mean Total Anomaly, CRM (88 Days)

Appendix I: Cross Correlation Matrices and Maps

Table I.1 : Lag Corrected Correlation Coefficients										
Logger	**4**	**5**	**6**	**8**	**9**	**10**	**11**	**13**	**14**	**15**
4	-	0.64	0.61	0.63	0.65	0.66	0.79	0.63	0.90	0.82
5	0.64	-	0.95	0.94	0.93	0.94	0.74	0.96	0.73	0.86
6	0.61	0.95	-	0.97	0.92	0.97	0.62	0.96	0.70	0.86
8	0.63	0.94	0.97	-	0.94	0.98	0.62	0.97	0.76	0.90
9	0.65	0.93	0.92	0.94	-	0.93	0.61	0.95	0.77	0.89
10	0.66	0.94	0.97	0.98	0.93	-	0.60	0.97	0.76	0.90
11	0.79	0.74	0.62	0.62	0.61	0.60	-	0.67	0.86	0.83
13	0.63	0.96	0.96	0.97	0.95	0.97	0.67	-	0.77	0.90
14	0.90	0.73	0.70	0.76	0.77	0.76	0.86	0.77	-	0.91
15	0.82	0.86	0.86	0.90	0.89	0.90	0.83	0.90	0.91	-
Mean	0.70	0.85	0.84	0.86	0.84	0.86	0.70	0.86	0.79	0.88

Table I.2 : Correlation Coefficients 1 to 0.90										
Logger	**4**	**5**	**6**	**8**	**9**	**10**	**11**	**13**	**14**	**15**
4									0.90	
5			0.95	0.94	0.93	0.94		0.96		
6		0.95		0.97	0.92	0.97		0.96		
8		0.94	0.97		0.94	0.98		0.97		0.90
9		0.93	0.92	0.94		0.93		0.95		
10		0.94	0.97	0.98	0.93			0.97		0.90
11										
13		0.96	0.96	0.97	0.95	0.97				0.90
14	0.90									0.91
15				0.90		0.90		0.90	0.91	

Table I.3 : Correlation Coefficients 0.90 to 0.80										
Logger	**4**	**5**	**6**	**8**	**9**	**10**	**11**	**13**	**14**	**15**
4										0.82
5										0.86
6										0.86
8										
9										0.89
10										
11									0.86	0.83
13										
14							0.86			
15	0.82	0.86	0.86		0.89		0.83			

Table I.4 : Correlation Coefficients 0.80 to 0.70										
Logger	**4**	**5**	**6**	**8**	**9**	**10**	**11**	**13**	**14**	**15**
4							0.79			
5							0.74		0.73	
6										
8									0.76	
9									0.77	
10									0.76	
11	0.79	0.74								
13									0.77	
14		0.73		0.76	0.77	0.76		0.77		
15										

Table I.5 : Correlation Coefficients < 0.70										
Logger	**4**	**5**	**6**	**8**	**9**	**10**	**11**	**13**	**14**	**15**
4		0.64	0.61	0.63	0.65	0.66		0.63		
5	0.64									
6	0.61						0.62		0.69	
8	0.63						0.62			
9	0.65						0.61			
10	0.66						0.60			
11			0.62	0.62	0.61	0.60		0.67		
13	0.63						0.67			
14			0.69							
15										

Figure I.1: Logger pairs sharing correlation coefficient connections greater than 0.90

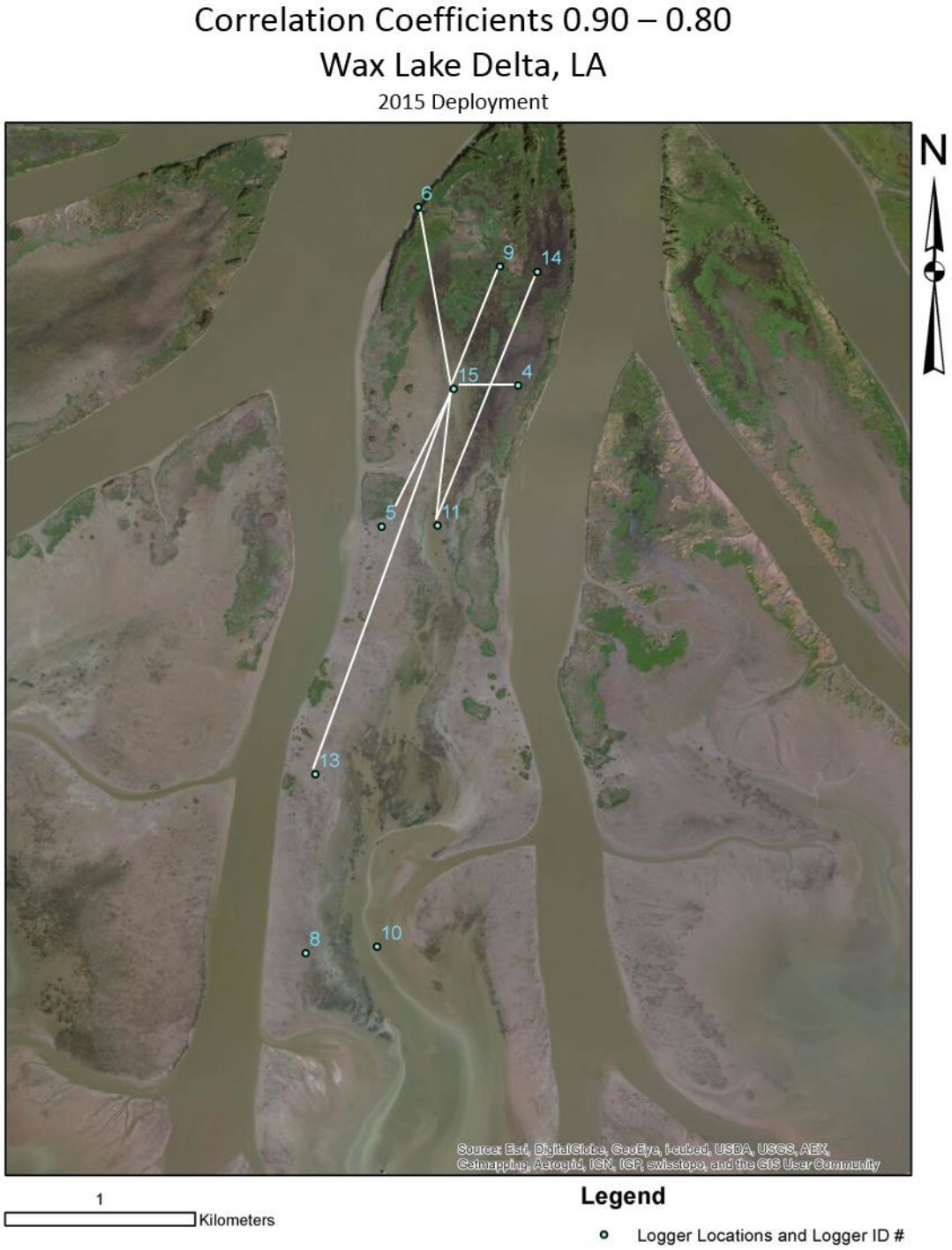

Figure I.2: Logger pairs sharing correlation coefficient connections between 0.90 and 0.80

Figure I.3: Logger pairs sharing correlation coefficient connections between 0.80 and 0.70

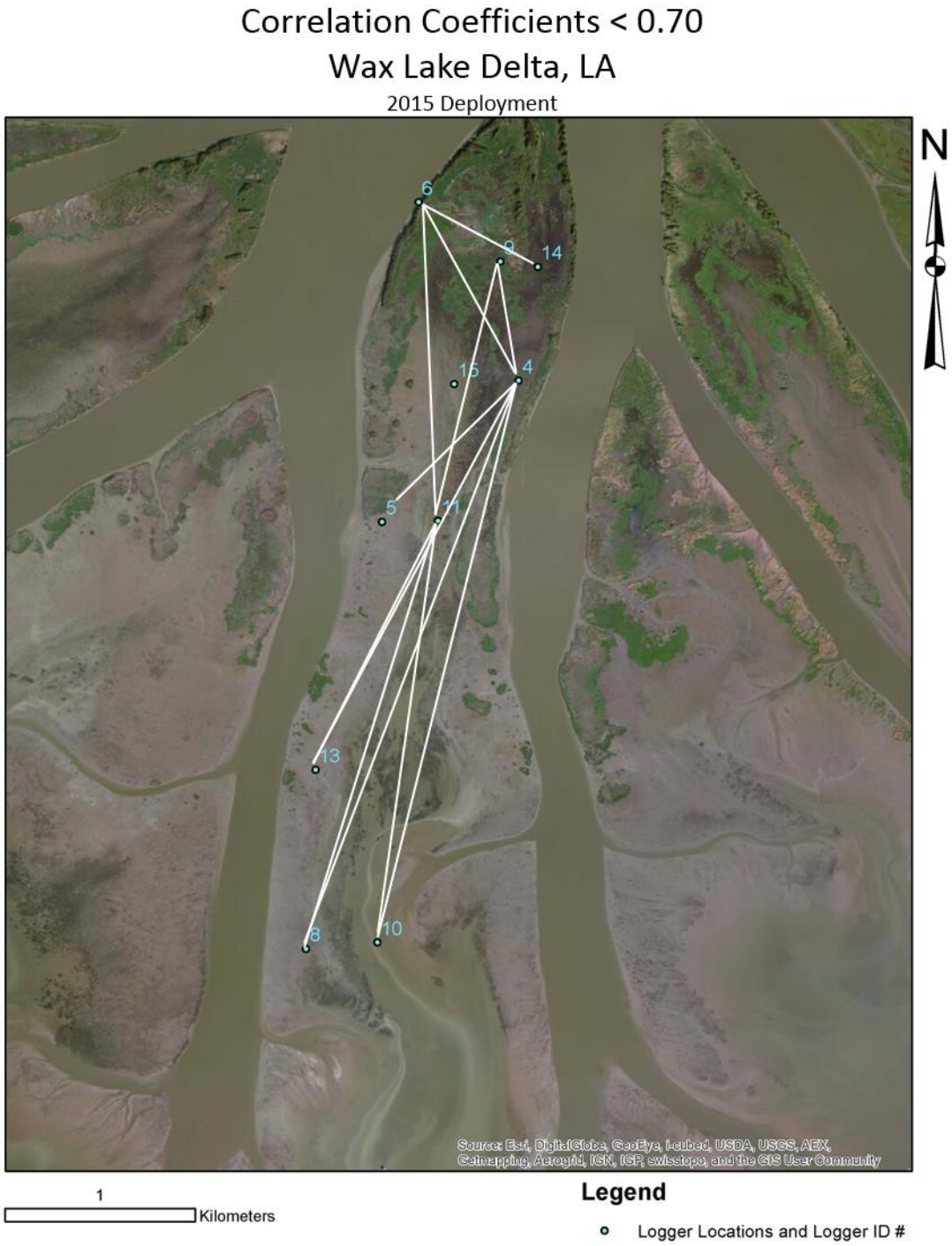

Figure I.4: Logger pairs sharing correlation coefficient connections less than 0.70

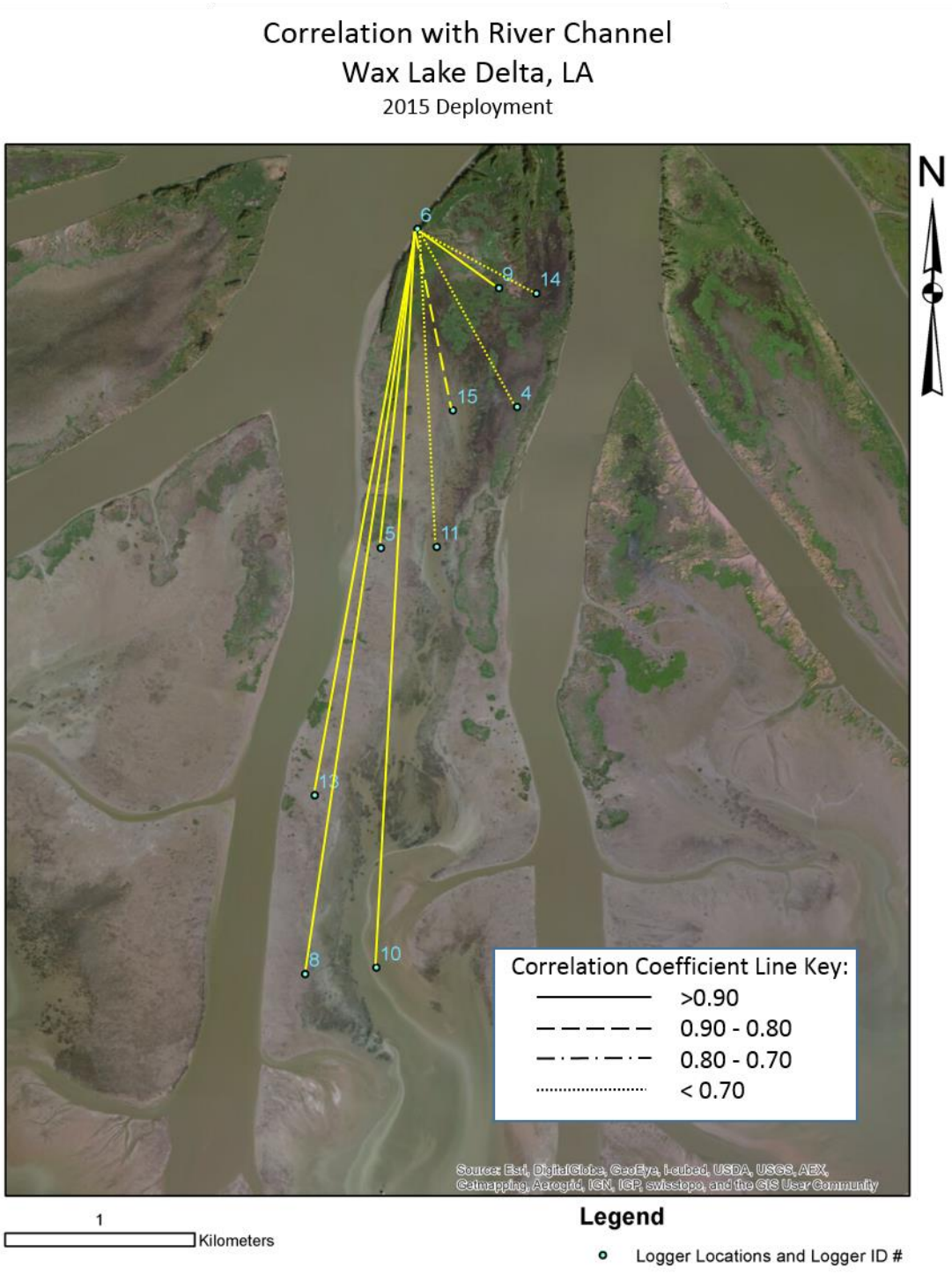

Figure I.5: Strength of correlation coefficient connection between the primary distributary channel and inner island locations

Appendix J: Data used for Cross Correlation and Distance Analysis

Table J.1: Distance Between Logger Locations (m)										
Logger	**4**	**5**	**6**	**8**	**9**	**10**	**11**	**13**	**14**	**15**
4	-	972	1044	3143	632	3024	825	2248	605	296
5	972	-	1689	2271	1472	2210	257	1338	1520	796
6	1044	1689	-	3959	488	3896	1678	3021	644	970
8	3143	2271	3959	-	3722	330	2330	942	3741	3046
9	632	1472	488	3722	-	3623	1393	2803	174	678
10	3024	2210	3896	330	3623	-	2233	950	3628	2956
11	825	257	1678	2330	1393	2233	-	1424	1413	722
13	2248	1338	3021	942	2803	950	1424	-	2835	2125
14	605	1520	644	3741	174	3628	1413	2835	-	727
15	296	796	970	3046	678	2956	722	2125	727	-
Mean	1421	1392	1932	2609	1665	2539	1364	1965	1699	1368

Table J.2: Normalized Distance Between Logger Locations (m)										
Logger	**4**	**5**	**6**	**8**	**9**	**10**	**11**	**13**	**14**	**15**
4	-	0.21	0.23	0.78	0.12	0.75	0.17	0.55	0.11	0.03
5	0.21	-	0.40	0.55	0.34	0.54	0.02	0.31	0.36	0.16
6	0.23	0.40	-	1.00	0.08	0.98	0.40	0.75	0.12	0.21
8	0.78	0.55	1.00	-	0.94	0.04	0.57	0.20	0.94	0.76
9	0.12	0.34	0.08	0.94	-	0.91	0.32	0.69	0.00	0.13
10	0.75	0.54	0.98	0.04	0.91	-	0.54	0.21	0.91	0.74
11	0.17	0.02	0.40	0.57	0.32	0.54	-	0.33	0.33	0.14
13	0.55	0.31	0.75	0.20	0.69	0.21	0.33	-	0.70	0.52
14	0.11	0.36	0.12	0.94	0.00	0.91	0.33	0.70	-	0.15
15	0.03	0.16	0.21	0.76	0.13	0.74	0.14	0.52	0.15	-

Table J.3: Zero-Centered Normalized Distance Between Logger Locations (m)										
Logger	**4**	**5**	**6**	**8**	**9**	**10**	**11**	**13**	**14**	**15**
4	-	-0.29	-0.27	0.28	-0.38	0.25	-0.33	0.05	-0.39	-0.47
5	-0.29	-	-0.10	0.05	-0.16	0.04	-0.48	-0.19	-0.14	-0.34
6	-0.27	-0.10	-	0.50	-0.42	0.48	-0.10	0.25	-0.38	-0.29
8	0.28	0.05	0.50	-	0.44	-0.46	0.07	-0.30	0.44	0.26
9	-0.38	-0.16	-0.42	0.44	-	0.41	-0.18	0.19	-0.50	-0.37
10	0.25	0.04	0.48	-0.46	0.41	-	0.04	-0.29	0.41	0.24
11	-0.33	-0.48	-0.10	0.07	-0.18	0.04	-	-0.17	-0.17	-0.36
13	0.05	-0.19	0.25	-0.30	0.19	-0.29	-0.17	-	0.20	0.02
14	-0.39	-0.14	-0.38	0.44	-0.50	0.41	-0.17	0.20	-	-0.35
15	-0.47	-0.34	-0.29	0.26	-0.37	0.24	-0.36	0.02	-0.35	-

Table J.4: Normalized Correlation Coefficient										
Logger	**4**	**5**	**6**	**8**	**9**	**10**	**11**	**13**	**14**	**15**
4	-	0.08	0.04	0.08	0.14	0.15	0.50	0.07	0.78	0.58
5	0.08	-	0.84	0.83	0.81	0.82	0.39	0.89	0.51	0.68
6	0.04	0.84	-	0.97	0.86	0.97	0.05	0.96	0.27	0.69
8	0.08	0.83	0.97	-	0.90	1.00	0.06	0.99	0.39	0.75
9	0.14	0.81	0.86	0.90	-	0.87	0.02	0.92	0.46	0.76
10	0.15	0.82	0.97	1.00	0.87	-	0.00	0.97	0.41	0.74
11	0.50	0.39	0.05	0.06	0.02	0.00	-	0.18	0.68	0.62
13	0.07	0.89	0.96	0.99	0.92	0.97	0.18	-	0.40	0.74
14	0.78	0.51	0.27	0.39	0.46	0.41	0.68	0.40	-	0.82
15	0.58	0.68	0.69	0.75	0.76	0.74	0.62	0.74	0.82	-

Table J.5: Zero-Centered Normalized Correlation Coefficient										
Logger	**4**	**5**	**6**	**8**	**9**	**10**	**11**	**13**	**14**	**15**
4	-	-0.42	-0.46	-0.42	-0.36	-0.35	0.00	-0.43	0.28	0.08
5	-0.42	-	0.34	0.33	0.31	0.32	-0.11	0.39	0.01	0.18
6	-0.46	0.34	-	0.47	0.36	0.47	-0.45	0.46	-0.23	0.19
8	-0.42	0.33	0.47	-	0.40	0.50	-0.44	0.49	-0.11	0.25
9	-0.36	0.31	0.36	0.40	-	0.37	-0.48	0.42	-0.04	0.26
10	-0.35	0.32	0.47	0.50	0.37	-	-0.50	0.47	-0.09	0.24
11	0.00	-0.11	-0.45	-0.44	-0.48	-0.50	-	-0.32	0.18	0.12
13	-0.43	0.39	0.46	0.49	0.42	0.47	-0.32	-	-0.10	0.24
14	0.28	0.01	-0.23	-0.11	-0.04	-0.09	0.18	-0.10	-	0.32
15	0.08	0.18	0.19	0.25	0.26	0.24	0.12	0.24	0.32	-

Appendix K: Change in Water Depth vs. Anomaly

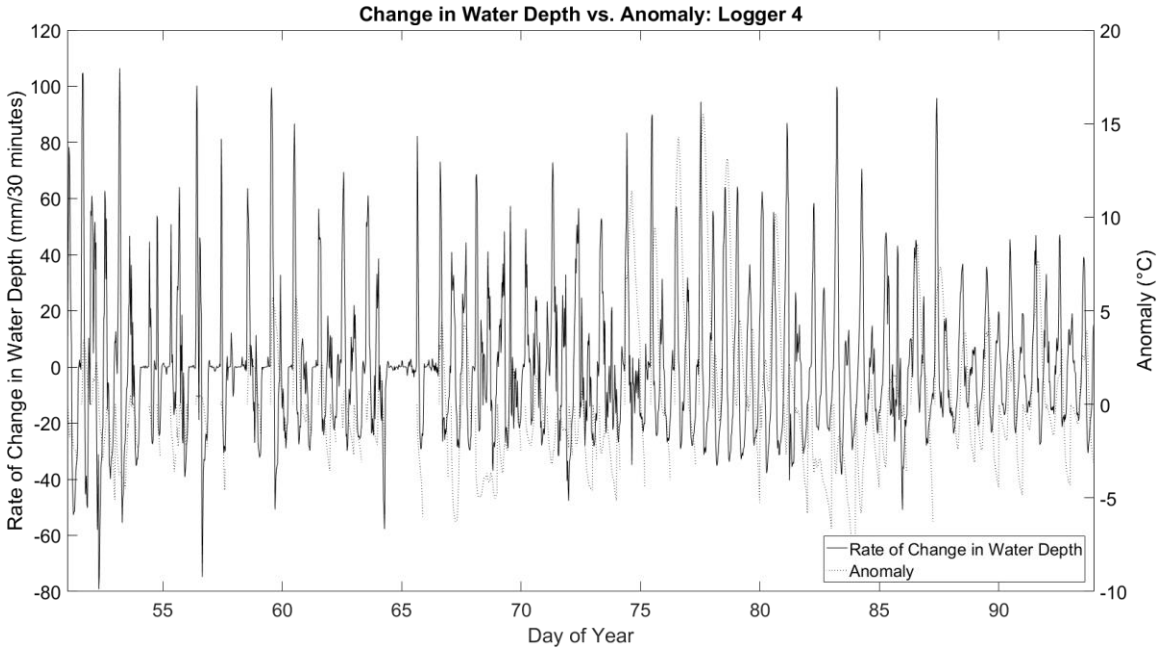

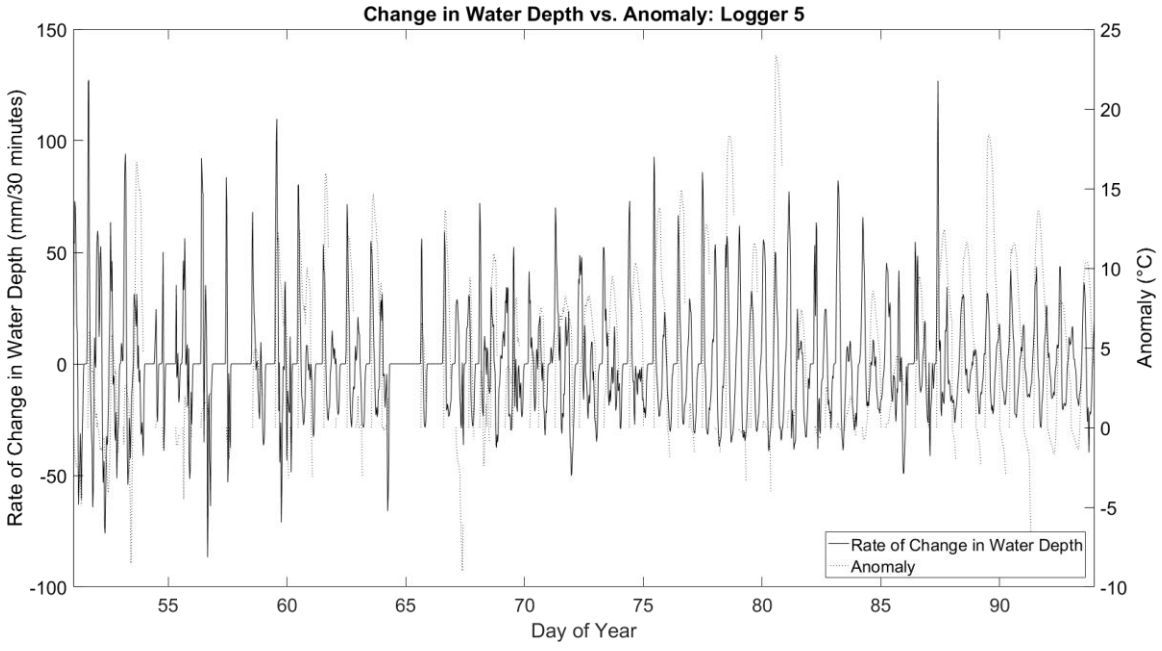

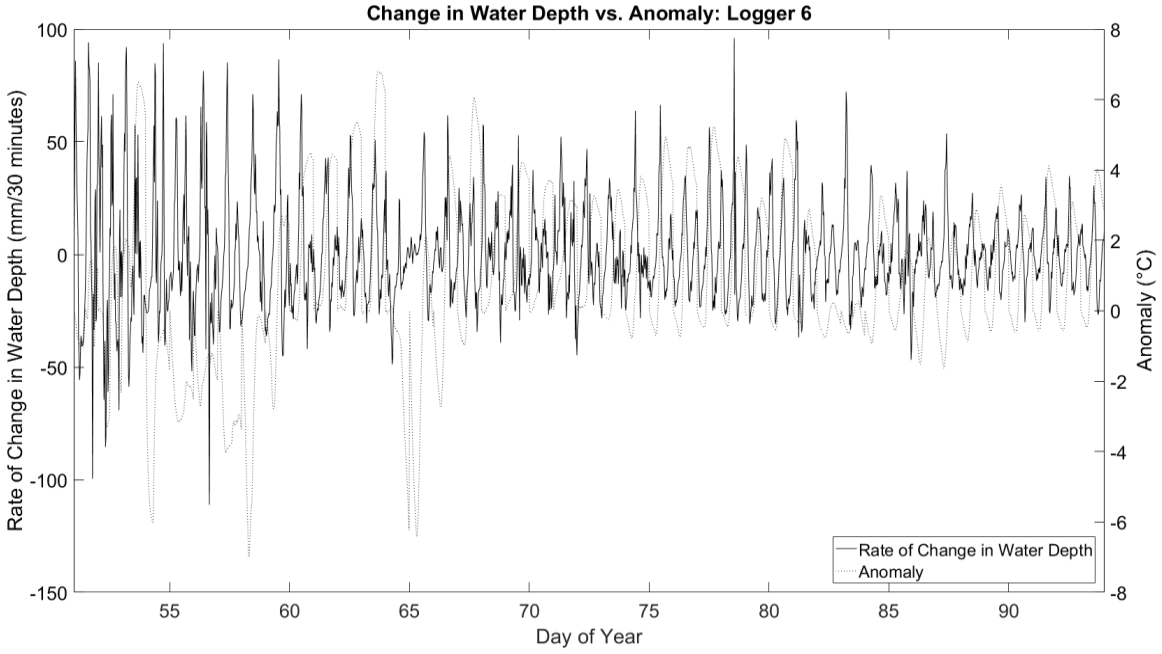
Change in Water Depth vs. Anomaly: Logger 6
Rate of Change in Water Depth (mm/30 minutes)
Anomaly (°C)
Day of Year
Rate of Change in Water Depth
Anomaly

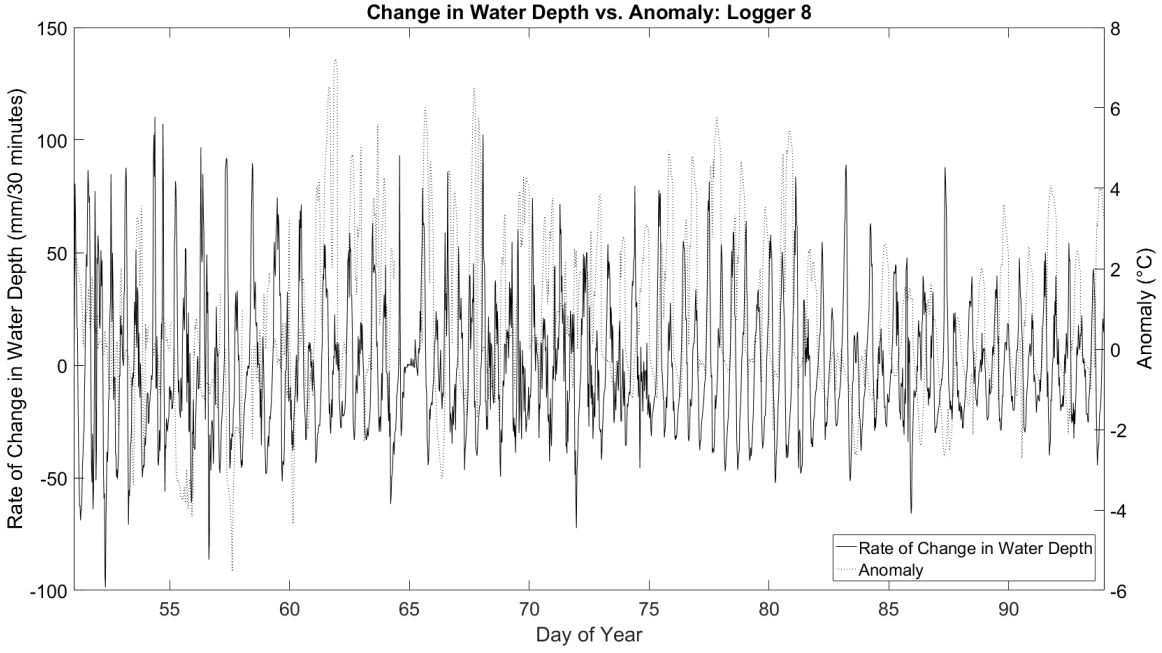
Change in Water Depth vs. Anomaly: Logger 8
Rate of Change in Water Depth (mm/30 minutes)
Anomaly (°C)
Day of Year
Rate of Change in Water Depth
Anomaly

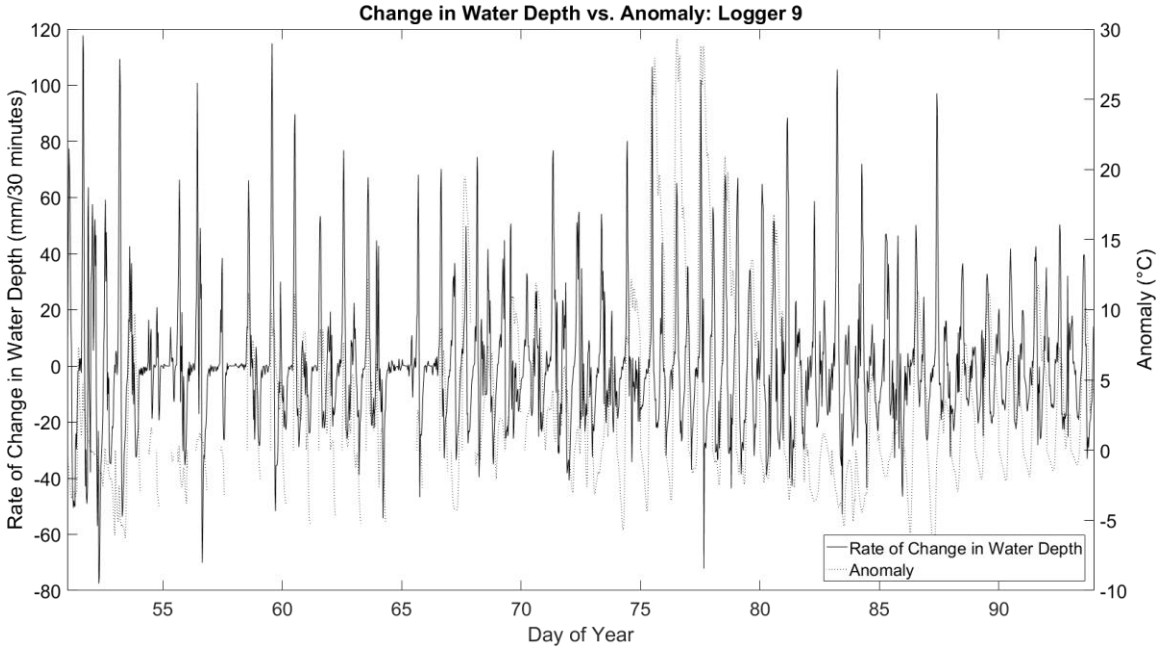
Change in Water Depth vs. Anomaly: Logger 9
Rate of Change in Water Depth (mm/30 minutes)
Anomaly (°C)
Day of Year
Rate of Change in Water Depth
Anomaly

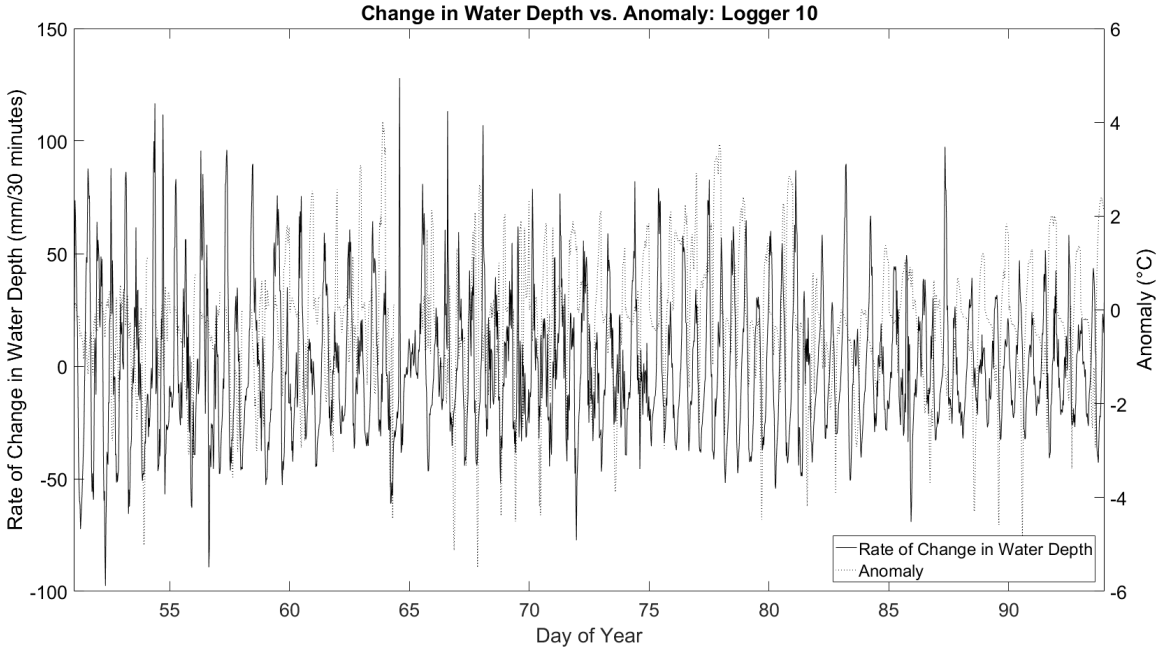
Change in Water Depth vs. Anomaly: Logger 10
Rate of Change in Water Depth (mm/30 minutes)
Anomaly (°C)
Day of Year
Rate of Change in Water Depth
Anomaly

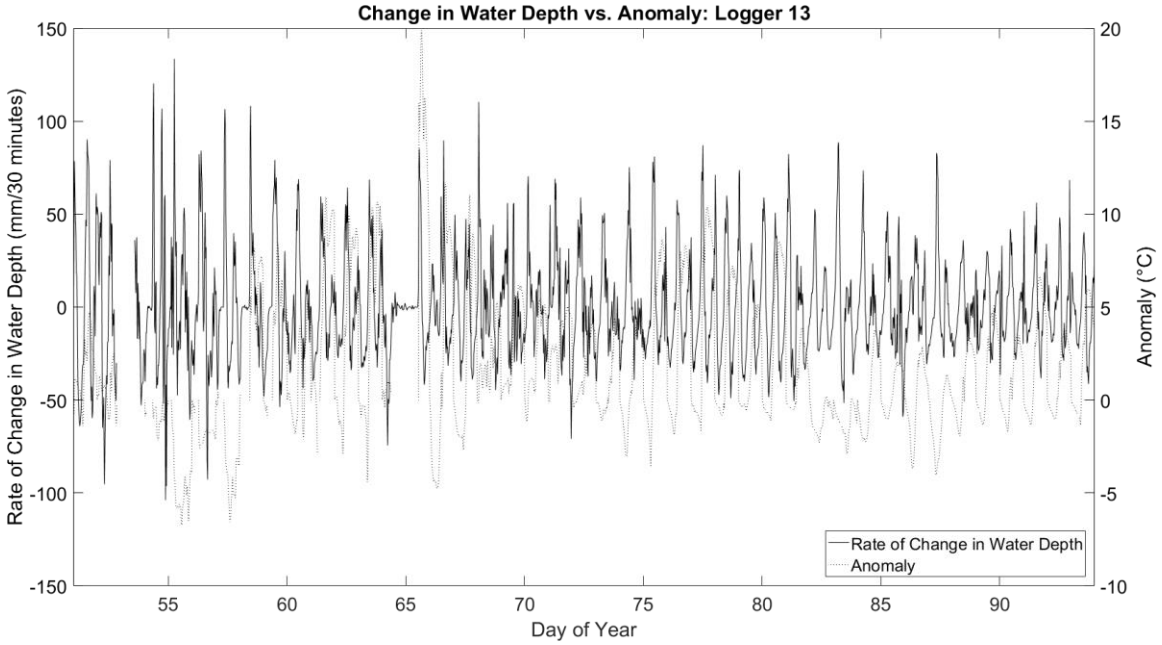
Change in Water Depth vs. Anomaly: Logger 13
Rate of Change in Water Depth (mm/30 minutes)
Anomaly (°C)
Day of Year
Rate of Change in Water Depth
Anomaly

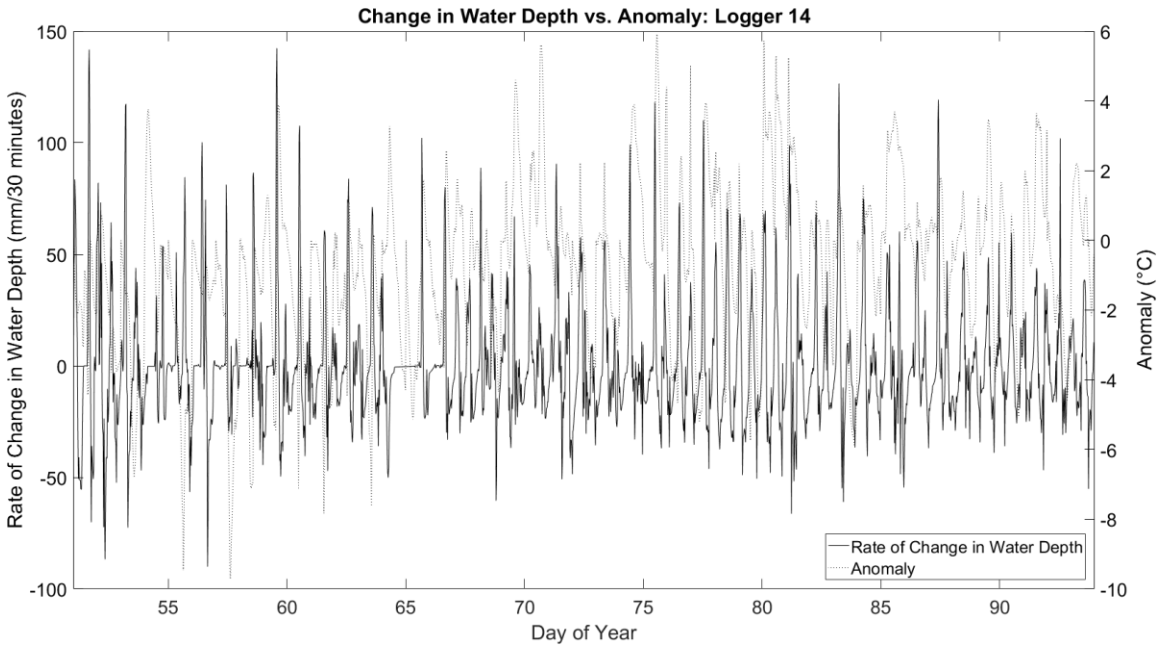
Change in Water Depth vs. Anomaly: Logger 14
Rate of Change in Water Depth (mm/30 minutes)
Anomaly (°C)
Day of Year
Rate of Change in Water Depth
Anomaly

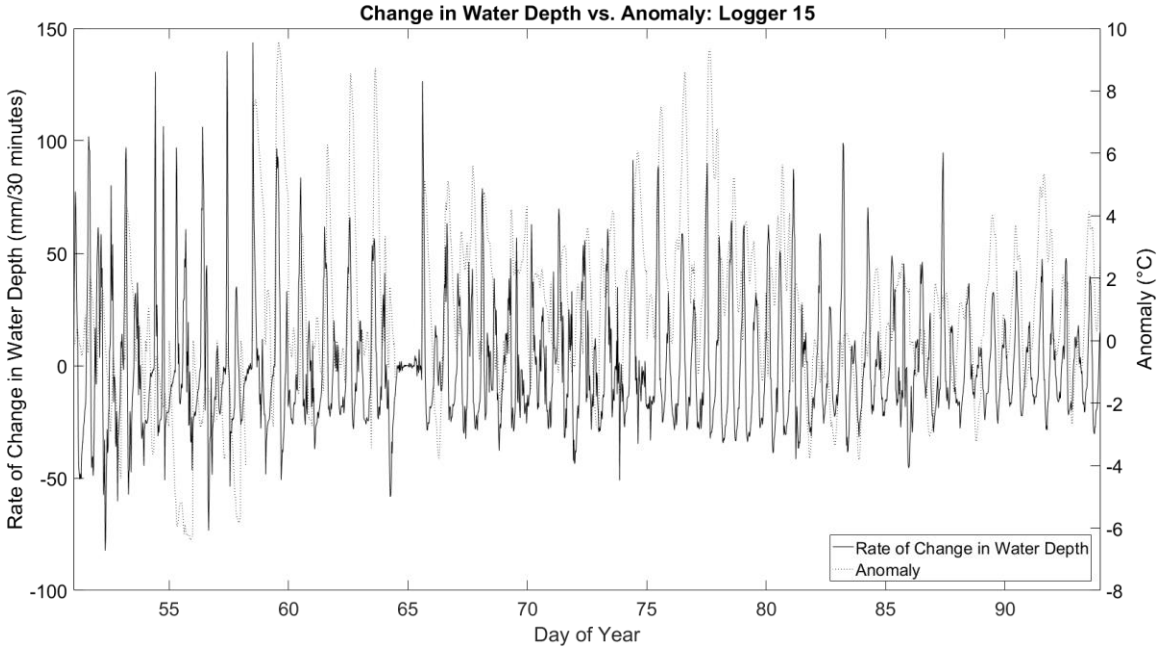
Change in Water Depth vs. Anomaly: Logger 15
Rate of Change in Water Depth (mm/30 minutes)
Anomaly (°C)
Day of Year
Rate of Change in Water Depth
Anomaly

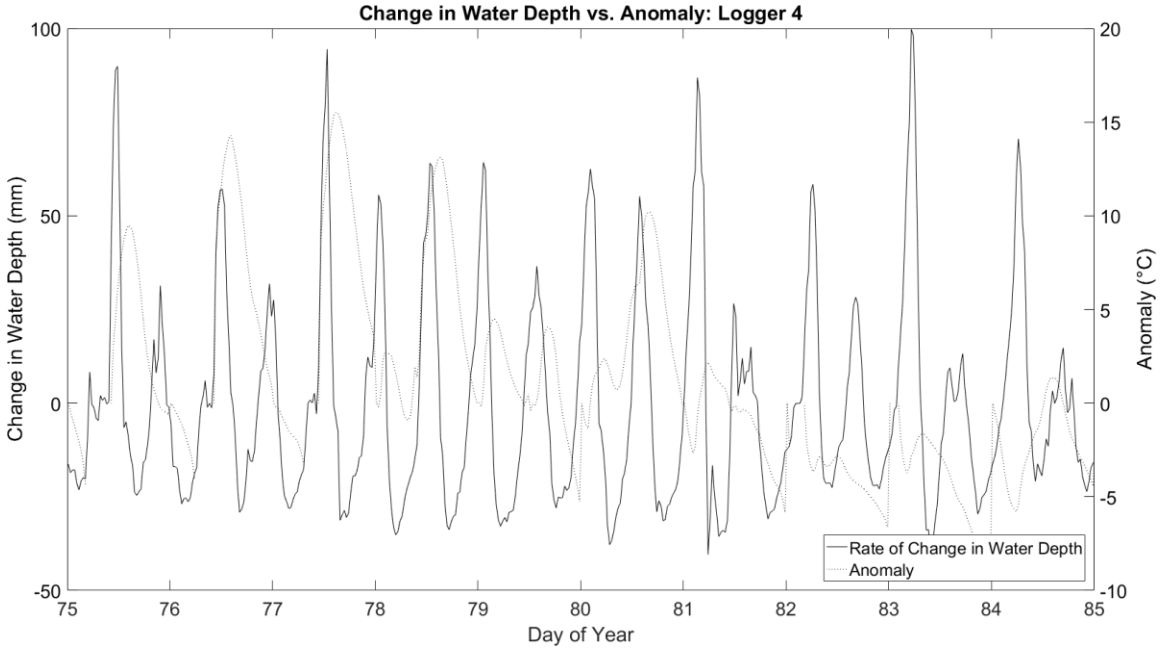
Change in Water Depth vs. Anomaly: Logger 4
Change in Water Depth (mm)
Anomaly (°C)
Day of Year
Rate of Change in Water Depth
Anomaly

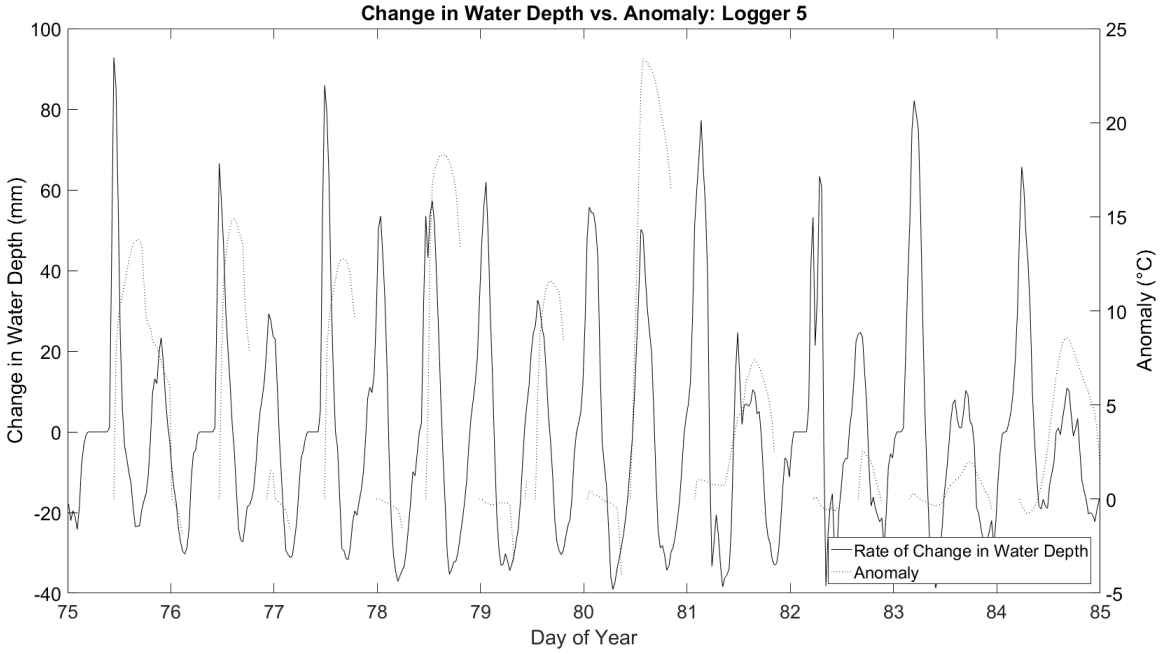
Change in Water Depth vs. Anomaly: Logger 5
Change in Water Depth (mm)
Anomaly (°C)
Day of Year
Rate of Change in Water Depth
Anomaly

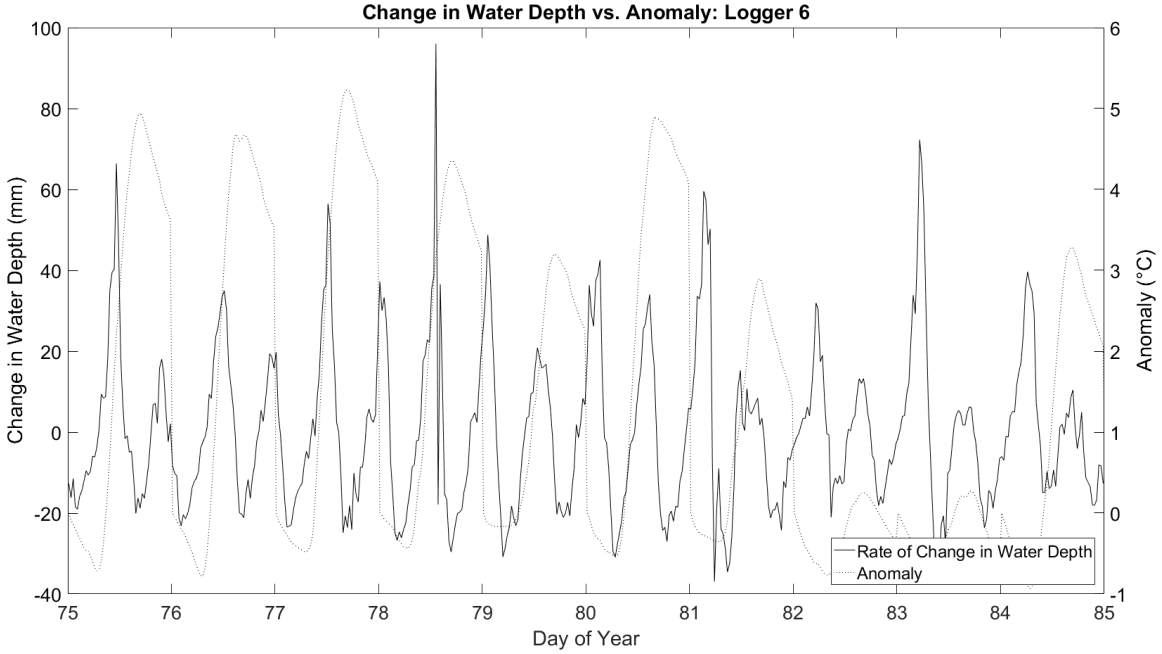
Change in Water Depth vs. Anomaly: Logger 6
Change in Water Depth (mm)
Anomaly (°C)
Day of Year
Rate of Change in Water Depth
Anomaly

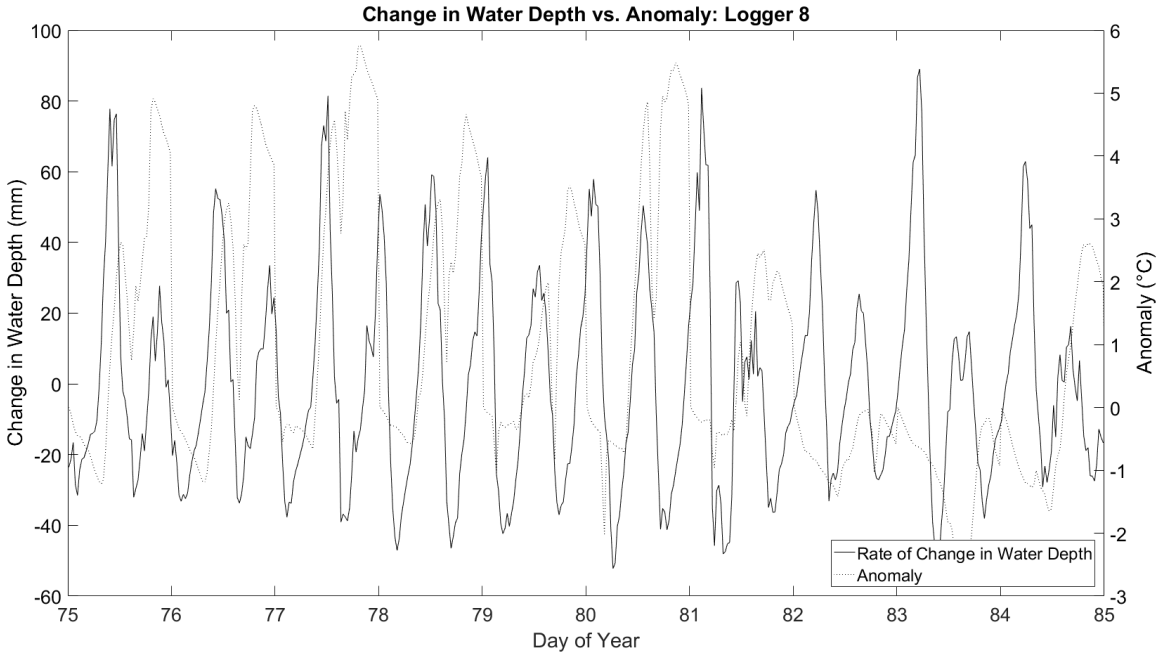
Change in Water Depth vs. Anomaly: Logger 8
Change in Water Depth (mm)
Anomaly (°C)
Day of Year
Rate of Change in Water Depth
Anomaly

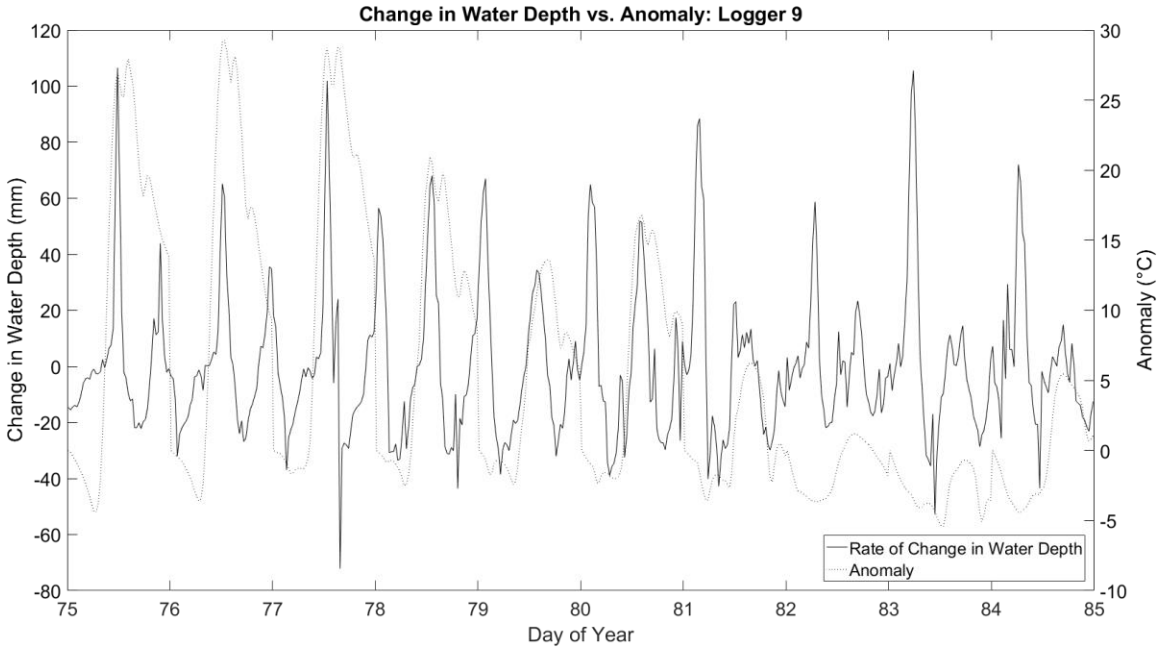
Change in Water Depth vs. Anomaly: Logger 9
Change in Water Depth (mm)
Anomaly (°C)
Day of Year
Rate of Change in Water Depth
Anomaly

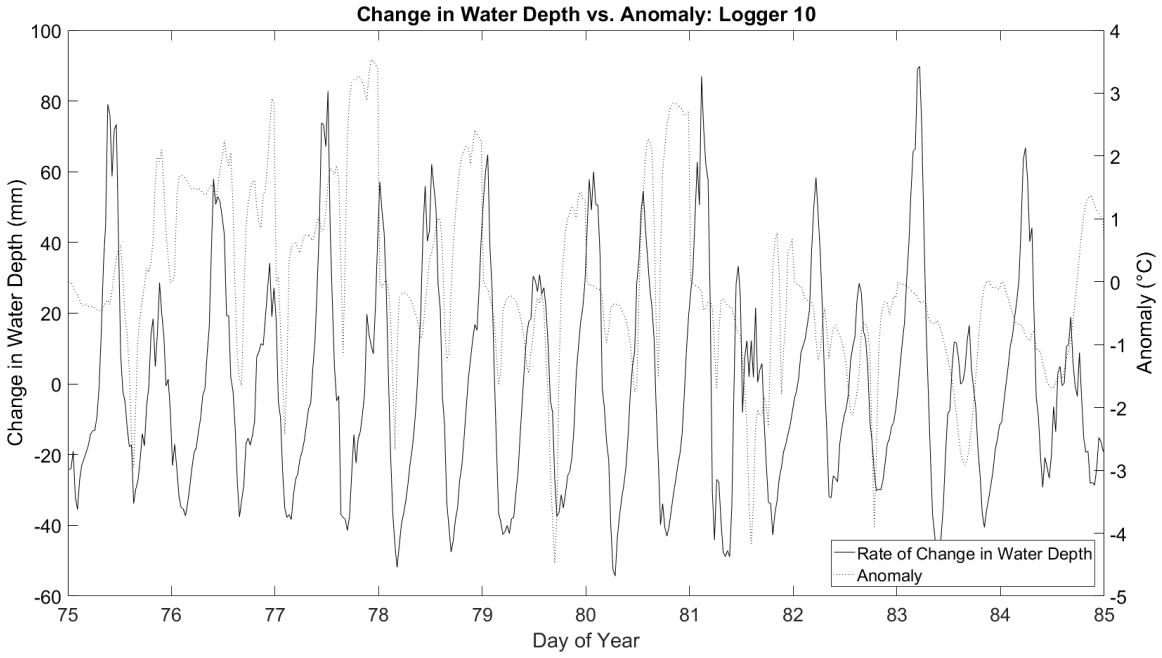
Change in Water Depth vs. Anomaly: Logger 10
Change in Water Depth (mm)
Anomaly (°C)
Day of Year
Rate of Change in Water Depth
Anomaly

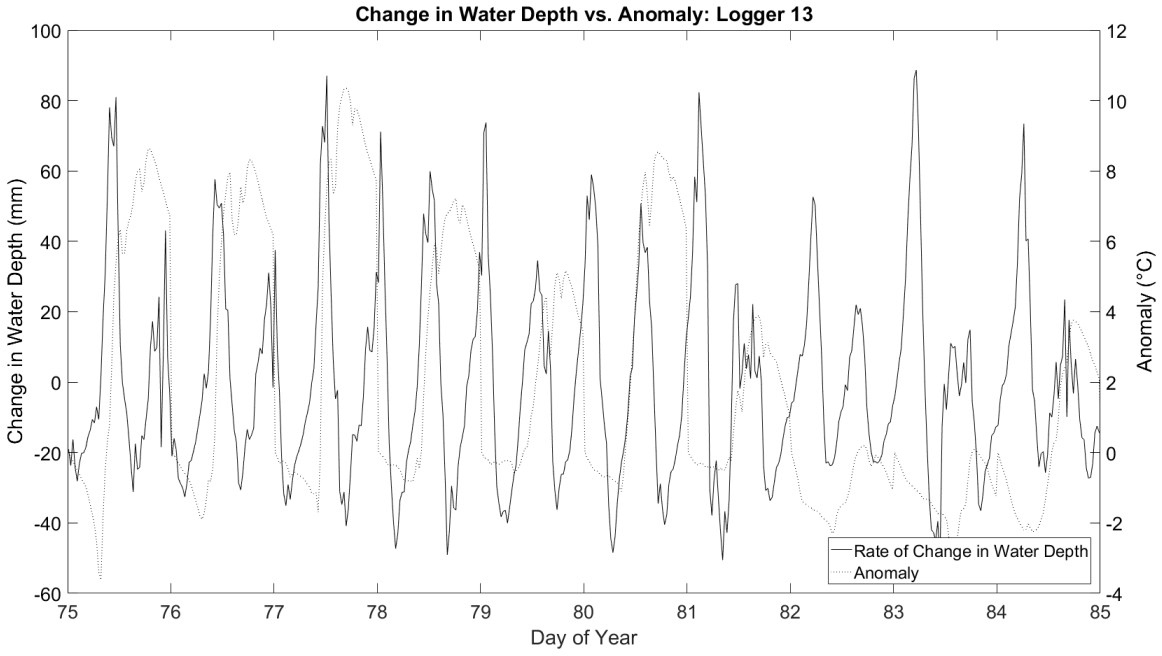
Change in Water Depth vs. Anomaly: Logger 13
Change in Water Depth (mm)
Anomaly (°C)
Day of Year
Rate of Change in Water Depth
Anomaly

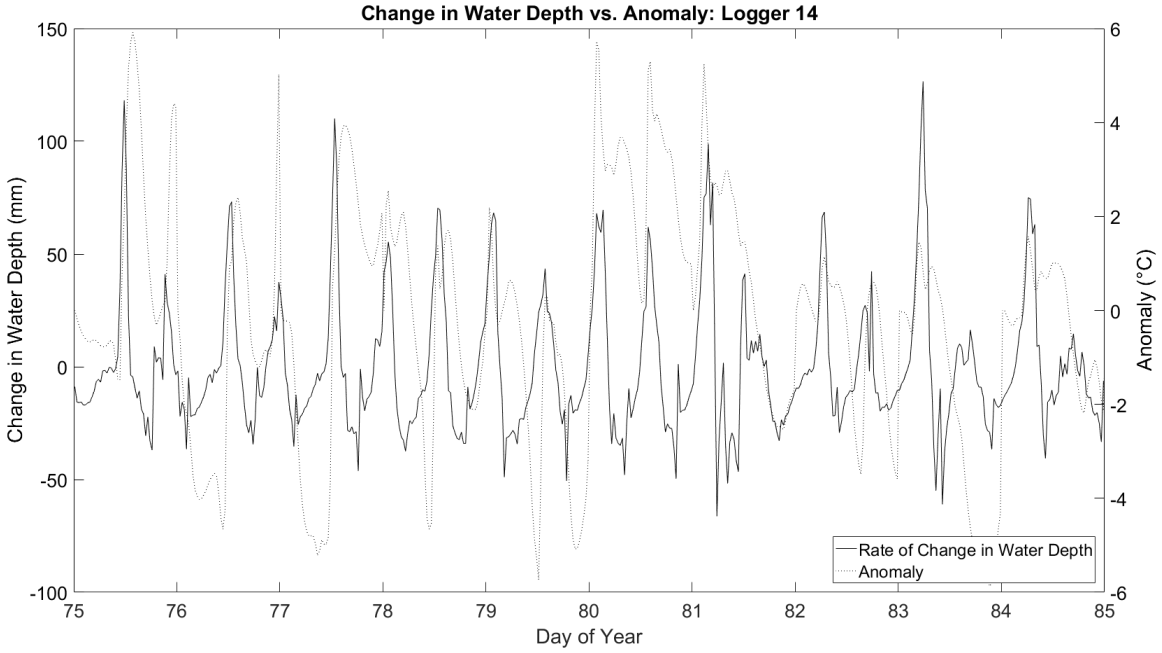
Change in Water Depth vs. Anomaly: Logger 14
Change in Water Depth (mm)
Anomaly (°C)
Day of Year
Rate of Change in Water Depth
Anomaly
150
100
50
0
-50
-100
6
4
2
0
-2
-4
-6
75
76
77
78
79
80
81
82
83
84
85

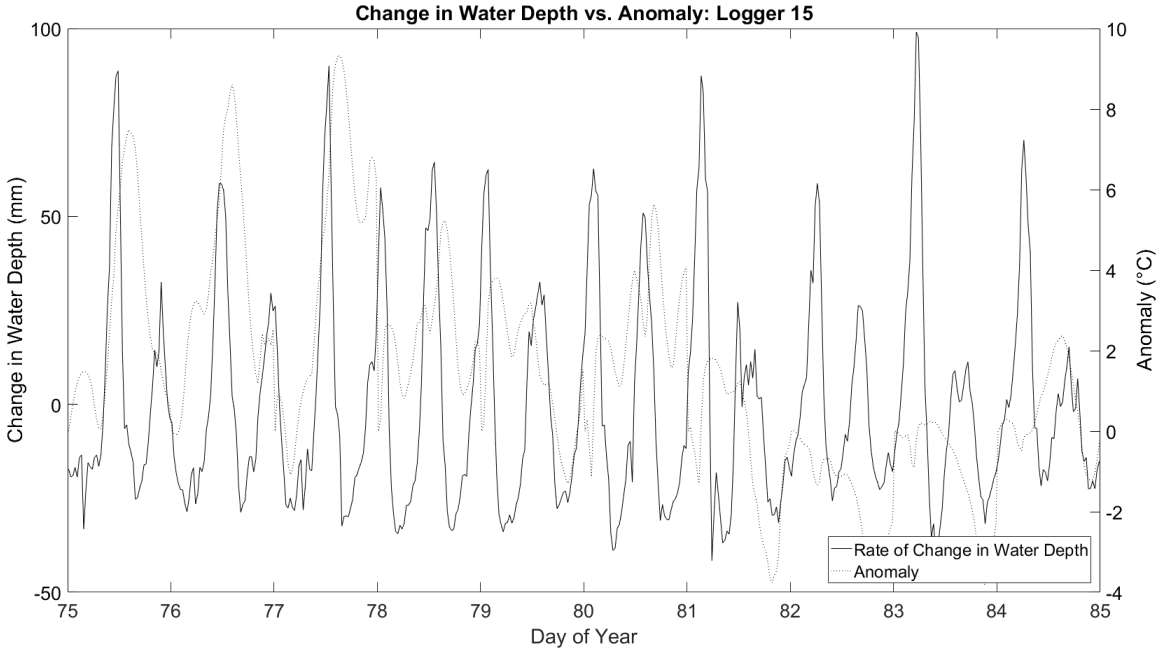
Change in Water Depth vs. Anomaly: Logger 15
Change in Water Depth (mm)
Anomaly (°C)
Day of Year
Rate of Change in Water Depth
Anomaly
100
50
0
-50
10
8
6
4
2
0
-2
-4
75
76
77
78
79
80
81
82
83
84
85

Appendix L: Alternate Ground Storage (G_s) Term Comparisons

Logger	Mean Anomaly (°C), Gs = 0.15	Mean Anomaly (°C), Gs = 0.05
10	1.00	1.09
14	1.28	1.41
8	2.03	2.23
15	2.39	2.58
6	2.50	2.75
4	3.61	4.08
13	4.24	4.66
9	6.51	7.19
5	7.01	7.50

Table L.1: Mean Positive Anomaly, Pyranometer (43 Days)

Logger	Mean Anomaly (°C), Gs = 0.15	Mean Anomaly (°C), Gs = 0.05
10	0.93	1.01
14	1.45	1.53
8	1.94	2.12
6	2.27	2.49
15	2.35	2.51
4	3.15	3.57
13	3.83	4.20
9	6.18	6.77
5	6.56	6.96

Table L.2: Mean Positive Anomaly, CRM (43 Days)

Logger	Mean Anomaly (°C), Gs = 0.15	Mean Anomaly (°C), Gs = 0.05
8	-0.86	-0.88
10	-0.95	-0.91
6	-1.09	-1.12
5	-1.14	-1.18
13	-1.22	-1.26
15	-1.29	-1.29
14	-1.66	-1.54
4	-1.85	-1.91
9	-1.91	-2.04

Table L.3: Mean Negative Anomaly, Pyranometer (43 Days)

Logger	Mean Anomaly (°C), Gs = 0.15	Mean Anomaly (°C), Gs = 0.05
8	-1.00	-1.00
10	-1.07	-1.04
6	-1.20	-1.22
5	-1.35	-1.40
13	-1.37	-1.44
15	-1.62	-1.60
9	-1.93	-2.05
14	-2.13	-2.04
4	-2.14	-2.20

Table L.4: Mean Negative Anomaly, CRM (43 Days)

Logger	Mean Anomaly (°C), Gs = 0.15	Mean Anomaly (°C), Gs = 0.05
14	-0.56	-0.38
10	-0.25	-0.16
4	0.45	0.75
8	0.71	0.87
15	1.01	1.18
6	1.01	1.14
13	1.90	2.16
9	3.27	3.64
5	4.83	5.14

Table L.5: Mean Total Anomaly, Pyranometer (43 Days)

Logger	Mean Anomaly (°C), Gs = 0.15	Mean Anomaly (°C), Gs = 0.05
14	-0.88	-0.73
10	-0.36	-0.28
4	-0.07	0.18
8	0.51	0.64
15	0.71	0.86
6	0.78	0.89
13	1.57	1.80
9	2.90	3.23
5	4.56	4.84

Table L.6: Mean Total Anomaly, CRM (43 Days)

Logger	Mean Anomaly (°C), Gs = 0.15	Mean Anomaly (°C), Gs = 0.05
10	0.83	0.94
14	1.16	1.23
15	1.59	1.70
8	1.61	1.75
6	1.86	2.08
4	2.24	2.56
13	3.43	3.78
9	3.91	4.24
5	4.43	4.80

Table L.7: Mean Positive Anomaly, CRM (88 Days)

Logger	Mean Anomaly (°C), Gs = 0.15	Mean Anomaly (°C), Gs = 0.05
6	-0.76	-0.79
8	-0.82	-0.81
10	-0.85	-0.81
5	-0.97	-1.03
15	-1.14	-1.09
13	-1.17	-1.23
9	-1.20	-1.33
4	-1.54	-1.60
14	-1.62	-1.55

Table L.8: Mean Negative Anomaly, CRM (88 Days)

Logger	Mean Anomaly (°C), Gs = 0.15	Mean Anomaly (°C), Gs = 0.05
14	-0.25	-0.10
10	-0.24	-0.16
8	0.28	0.42
4	0.31	0.51
15	0.50	0.64
6	0.80	0.91
13	1.26	1.46
9	1.54	1.81
5	2.39	2.64

Table L.9: Mean Total Anomaly, CRM (88 Days)